

Jan Bengsch

# Investigation and analysis of a CO<sub>2</sub> heat pump chiller with novel two-stage evaporator

Master's thesis in Sustainable Energy

Supervisor: Professor Armin Hafner

Co-supervisor: Mihir Mouchum Hazarika

August 2022



Jan Bengsch

# **Investigation and analysis of a CO<sub>2</sub> heat pump chiller with novel two-stage evaporator**

Master's thesis in Sustainable Energy  
Supervisor: Professor Armin Hafner  
Co-supervisor: Mihir Mouchum Hazarika  
August 2022

Norwegian University of Science and Technology  
Faculty of Engineering  
Department of Energy and Process Engineering





## Masterarbeit

für Herrn Jan Bengsch  
Matrikelnummer 5024604

### Investigation and analysis of a CO<sub>2</sub> heat pump chiller with novel two-stage evaporator

This study will be carried out to investigate the performance of a novel compact two-stage evaporator configuration. What makes this evaporator configuration unique is the integration of a self-circulation loop on one side of a plate heat exchanger (pre-cooling of secondary fluid) and an ejector-assisted circulation loop on the other side (after-cooling of secondary flow). The secondary loop is internally connected within the plate heat exchanger, which significantly reduces the pipework required for two separate heat exchangers connected in series on the secondary fluid path. As a result, the compact two-stage heat exchanger requiring less space and less connections.

Heat pump chillers currently available in the market have some limitations in terms of cooling capacity and space requirements. Some high-performance heat pump chillers require two chilling heat exchangers to function efficiently. Hence, the proposed compact heat exchanger design would be an attractive solution for such applications, especially when larger temperature differences across the secondary loop are desired. This compact design gives the opportunity to reduce the space requirements considerably and increase the volume specific capacity of the heat exchanger and the unit itself. In addition, the integration of ejector-assisted circulation loop and the self-circulation loop (gravity driven) has the potential to enhance the system performance significantly by elevating the suction pressure of the compressor.

In this proposed research work, studies will be carried out to investigate the implementations of this novel two-stage heat exchanger in a heat pump chiller. The tasks and objectives will be:

- Literature review: Chiller systems for high performance buildings, surplus heat recovery exchangers and concepts, thermal energy storage devices, ejectors, chiller systems, state-of-the-art refrigeration/AC systems for warm climates etc.

- Selection of the design conditions of a heat pump chiller for a suitable application (example: fish processing and hotel)
- Selection of components for the proposed chiller unit to be modeled
- Design and develop a system simulation model in Modelica for the proposed units
- Experimental study of the pilot evaporator and validation of the simulation model
- Discussion of the results and evaluation of the suitability of the investigated concept(s) for the intended use, described in a master thesis
- Draft version of a scientific article based on the finding from this research
- Proposal for further work

Die Bearbeitungszeit des schriftlichen Teils dieser Arbeit beträgt sechs Monate.

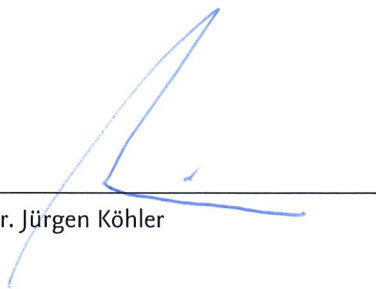
Ausgabe: 10.02.2022

Abgabe: 10.08.2022

Erstprüfer: Prof. Dr.-Ing. Jürgen Köhler

---

Prof. Dr. Jürgen Köhler



# Eidesstattliche Erklärung

Hiermit erkläre ich eidesstattlich, dass ich diese Arbeit eigenständig angefertigt und keine anderen als die angegebenen Hilfsmittel verwendet habe.

Jan Benysch

Braunschweig den 10. August 2022

# Abstract

Heat pump chillers currently available on the market often suffer from either insufficient cooling capacity or from too high space requirements. To address both issues simultaneously, a compact, novel two-stage evaporator was developed at NTNU in collaboration with SINTEF and Alfa Laval. It consists of two commercially available brazed plate heat exchangers which are assembled back to back. The compactness and thus uniqueness of this heat exchanger is due to an internal connection of the secondary loop between the two evaporators. This means that only two connections are required for the secondary fluid, thus saving pipework and space. In addition, the two-stage evaporator is also novel due to its mode of operation. Both evaporators are operated at different evaporation pressures. By using the thermosyphon principle, the medium-pressure evaporator, in which the secondary fluid is pre-cooled, is operated as a flooded gravity-fed evaporator. The low-pressure evaporator is operated as an ejector-fed evaporator via the suction mass flow of the ejector and cools the secondary fluid further down to the outlet temperature. All of this results in a higher temperature differential across the secondary fluid, a higher volumetric capacity of the evaporator and the overall system, and better system performance due to a two-stage evaporation and the higher compressor suction pressure enabled by the ejector.

In this thesis, this novel two-stage evaporator was investigated. This was done with the help of simulation models that were created in the course of this work using the TIL library. Furthermore, the simulation model was validated with the help of measurement data from a test rig. For this purpose, the state of the art of CO<sub>2</sub> heat pump chillers was first summarized and a concept for a heat pump chiller was developed on its basis. Then the model was developed and the system was investigated and validated in two steps. First, the simulation model for the gravity-fed evaporator loop was developed and extended into a heat pump chiller model with a single-stage evaporator. The second step was to extend the model to include the ejector-fed evaporator, to validate the two-stage evaporator with the aid of measurement data and to carry out further model-based investigations.



# Table of Contents

<b>Table of Symbols</b>	<b>XI</b>
<b>1 Introduction</b>	<b>1</b>
<b>2 CO<sub>2</sub> heat pumps and refrigeration systems</b>	<b>3</b>
2.1 CO <sub>2</sub> as a refrigerant . . . . .	3
2.2 Thermodynamic fundamentals of the CO <sub>2</sub> vapor compression cycle . . . . .	5
2.3 Process improvement for CO <sub>2</sub> vapor compression cycles . . . . .	8
2.4 Evaporator configurations . . . . .	11
2.5 Design of the heat pump chiller to be investigated . . . . .	17
<b>3 The gravity-fed evaporator system</b>	<b>18</b>
3.1 Model design and parameterization . . . . .	18
3.2 Model based examinations . . . . .	26
<b>4 The heat pump chiller with novel two-stage evaporator</b>	<b>38</b>
4.1 Model design and parameterization . . . . .	38
4.2 Model based examinations . . . . .	40
4.3 Adjustments of the current design for further investigations . . . . .	47
4.4 Effect of the division of the number of plates in the two-stage evaporator . . . . .	49
4.5 Part load behavior of the system . . . . .	52
<b>5 Summary and outlook</b>	<b>55</b>
<b>Bibliography</b>	<b>57</b>
<b>Appendix</b>	<b>61</b>
<b>A Test rig setup</b>	<b>62</b>
<b>B Interconnection of the cells in the heat exchanger</b>	<b>64</b>
<b>C Controller settings</b>	<b>65</b>
<b>D Pressure drop of the mass flow sensor</b>	<b>66</b>
<b>E Further data from the validation</b>	<b>67</b>
<b>F Conference paper for the 15th IIR-Gustav Lorentzen conference of Natural Refrigerants</b>	<b>68</b>
<b>G Abstract for the 26th International Congress of Refrigeration</b>	<b>79</b>

# List of Figures

2.1	Principle sketch of the simple subcritical CO <sub>2</sub> vapor compression cycle in a p, h diagram . . . . .	6
2.2	Principle sketches of transcritical CO <sub>2</sub> vapor compression cycles a) in the p,h diagram to illustrate the optimal high pressure and b) an optimization of heat rejection in the gas cooler at two different pressures. . . . .	7
2.3	Principle sketch of the transcritical CO <sub>2</sub> vapor compression cycle with an internal heat exchanger in a p, h diagram . . . . .	9
2.4	Principle sketch of the design of an ejector with its qualitative pressure curve over the construction length a) and the qualitative state change in the p,h diagram b) . . .	10
2.5	Heat transfer coefficient of CO <sub>2</sub> during evaporation in horizontal tubes, d = 3 mm, G = 390 kg m <sup>-2</sup> s <sup>-1</sup> , q = 20 kW m <sup>-2</sup> from Cheng et al. [8] . . . . .	12
2.6	Schematic diagram of flooded evaporators a) with forced circulation and b) with natural circulation . . . . .	13
2.7	Schematic temperature heat transfer diagram of a single stage evaporator a) and a two-stage evaporator b) . . . . .	14
2.8	Schematic illustration of different two-stage evaporator configurations for heat pump chillers: a) is an ejector operated two-stage evaporator from [16] where one evaporator is operated with the ejector discharge mass flow and the other with the suction mass flow, the configuration b) from [6] and the configuration c) from [2] are both two-stage evaporator configurations where the first evaporator is gravity-fed and the second is driven by the suction mass flow of the ejector and d) from [32] is an extended configuration of c) using an IHX to superheat the suction mass flow of the ejector. . . . .	15
2.9	Picture of the novel two-stage evaporator prototype from Alfa Laval a) and simplified principle sketch of its working principle b) . . . . .	16
2.10	Schematic drawing of the heat pump chiller with two-stage evaporation . . . . .	17
3.1	Schematic diagram of the refrigeration system with the gravity-fed evaporator loop in Dymola (Green lines: CO <sub>2</sub> , Light blue lines: water) . . . . .	19
3.2	Schematic diagram of the gravity-fed evaporator loop . . . . .	20
3.3	Illustration of the state points (from Figure 3.1) under design conditions of a) the entire gravity-fed evaporator system in the p,h diagram and b) zoomed in on the state points of the gravity-fed evaporator loop) . . . . .	27
3.4	Validation of the gravity loop for a) 11 different operating points at 38 bar separator pressure and b) for 10 different operating points at three different separator pressures. . . . .	29
3.5	Influence of the static height on the cooling capacity and the refrigerant mass flow in the gravity loop and via the gas cooler (separator pressure: 41 bar, water inlet temperature: 12 °C, water mass flow: 24 kg min <sup>-1</sup> ). . . . .	31

3.6	Influence of the static height on the pressure difference in the downcomer $\Delta p_{Down.}$ , evaporator $\Delta p_{Evap.}$ and riser $\Delta p_{Riser}$ as well as on the refrigerant vapor fraction $x$ at the outlet of the evaporator (separator pressure: 41 bar, water inlet temperature: 12 °C, water mass flow: 24 kg min <sup>-1</sup> ). . . . .	31
3.7	Influence of the riser diameter on the pressure difference in the downcomer $\Delta p_{Down.}$ , evaporator $\Delta p_{Evap.}$ and riser $\Delta p_{Riser}$ as well as on the refrigerant vapor fraction $x$ at the outlet of the evaporator (separator pressure: 41 bar, water inlet temperature: 12 °C, water mass flow: 24 kg min <sup>-1</sup> ). . . . .	32
3.8	Investigation of the influence of different water inlet temperatures on the gravity-fed evaporator loop with respect to the cooling capacity $\dot{Q}_{Evap.}$ and the refrigerant mass flow over the gravity-fed evaporator loop $\dot{m}_{Evap.}$ (separator pressure: 41 bar, water mass flow: 24 kg min <sup>-1</sup> ). . . . .	34
3.9	Investigation of the influence of different water inlet temperatures on the gravity-fed evaporator loop with respect to the pressure differences in the downcomer $\Delta p_{Down.}$ , evaporator $\Delta p_{Evap.}$ and riser $\Delta p_{Riser}$ as well as on the refrigerant vapor fraction $x$ at the outlet of the evaporator (separator pressure: 41 bar, water mass flow: 24 kg min <sup>-1</sup> ). . .	34
3.10	Investigation of the influence of different water inlet temperatures on the gravity-fed evaporator loop with respect to the cooling capacity $\dot{Q}_{Evap.}$ , the water temperature differences between inlet and outlet of the evaporator $\Delta T_w$ and the temperature difference between the refrigerant and the water entering the evaporator $\Delta T_{in}$ (separator pressure: 41 bar, water mass flow: 24 kg min <sup>-1</sup> ). . . . .	35
3.11	Investigation of the influence of different water mass flows on the gravity-fed evaporator loop with respect to the cooling capacity $\dot{Q}_{Evap.}$ and the refrigerant mass flow over the gravity-fed evaporator loop $\dot{m}_{Evap.}$ (separator pressure: 41 bar, water inlet temperature: 12 °C). . . . .	36
3.12	Investigation of the influence of different water mass flows on the gravity-fed evaporator loop with respect to the pressure differences in the downcomer $\Delta p_{Down.}$ , evaporator $\Delta p_{Evap.}$ and riser $\Delta p_{Riser}$ as well as on the refrigerant vapor fraction $x$ at the outlet of the evaporator(separator pressure: 41 bar, water inlet temperature: 12 °C). . . . .	37
3.13	Investigation of the influence of different water mass flows on the gravity-fed evaporator loop with respect to the cooling capacity $\dot{Q}_{Evap.}$ , the water temperature differences between inlet and outlet of the evaporator $\Delta T_w$ and the temperature difference between refrigerant and water entering the evaporator $\Delta T_{in}$ (separator pressure: 41 bar, water inlet temperature: 12 °C) . . . . .	37
4.1	Schematic diagram of the heat pump chiller model with the two-stage evaporator in Dymola (Green lines: CO <sub>2</sub> , Light blue lines: water) . . . . .	39
4.2	Illustration of the state points under design conditions of a) heat pump chiller in the p,h diagram and b) zoomed in on the state points of the gravity-fed evaporator loop) . . . . .	42

4.3	Temperature distribution curve for water and CO <sub>2</sub> in the gravity- and ejector-fed evaporator. Blue lines represent the temperature profile of the water and green lines represent the temperature profile of the CO <sub>2</sub> . The solid lines represent the curves under design conditions and the dashed lines represent the curves after correction of the heat transfer model in the ejector-loop for validation. . . . .	44
4.4	Validation of the two-stage evaporator with a water mass flow of 24, 18, 16 and 12 kg/min for a) the gravity-evaporator loop with 12 different operating points and b) the ejector-fed evaporator for 12 different operating points at 38 bar evaporation pressure. . . . .	45
4.5	Investigation of the influence of different water inlet temperatures on the combined COP of the Heat pump chiller at three different ejector-fed evaporation pressures . .	46
4.6	Schematic illustration of the possible adjustments for the redesign of the test rig with and without a mass flow sensor . . . . .	48
4.7	Influence of the division of the number of plates in the two-stage evaporator on the cooling capacity distribution and the vapor fraction in both evaporators. The number of plates of the gravity-fed evaporator is shown on the X-axis. Together with the ejector-fed evaporator, the total number of plates is always 80. . . . .	50
4.8	Effect of the division of the number of plates in the two-stage evaporator on the refrigeration COP. On the X-axis the number of plates of the gravity-fed evaporator is shown. Together with the ejector-fed evaporator, the total number of plates is always 80. . . . .	50
4.9	Effect of the division of the number of plates in the two-stage evaporator on the relative change of the refrigeration COP ( $COP/COP_{max}$ ) and on the separator pressure ( $p_{sep}$ ) over the refrigeration load distribution between gravity-fed $\dot{Q}_{GFE}$ and ejector-fed evaporators $\dot{Q}_{EFE}$ . . . . .	51
4.10	Investigation of the part load behavior of the two-stage evaporator system based on the cooling capacity distribution and the refrigeration COP over the water outlet temperature of the ejector-fed evaporator. (Water inlet temperature constant at 12 °C)	52
4.11	Investigation of the part load behavior of the two-stage evaporator system based on the evaporating pressure in the gravity-fed evaporator $p_{GFE}$ , and ejector-fed evaporator $p_{EFE}$ , and the vapor fraction at the outlet of the two evaporators $x_{GFE}$ and $x_{EFE}$ over the water outlet temperature of the ejector-fed evaporator. . . . .	53
4.12	Investigation of the part load behavior of the two-stage evaporator system based on the distribution of the refrigerant mass flow on the gravity-fed evaporator $\dot{m}_{GFE}$ and the ejector-fed evaporator $\dot{m}_{EFE}$ as well as the water-side temperature difference over the two evaporators $\Delta T_{w,GFE}$ and $\Delta T_{w,EFE}$ over the water outlet temperature of the ejector-fed evaporator. . . . .	54
A.1	Picture of the test rig . . . . .	62
A.2	P&ID of the laboratory test rig for the two-stage evaporator. . . . .	63
B.1	Interconnection of the cells in the heat exchanger [35]. . . . .	64

D.1 Pressure drop curve the mass flow sensor: Rheonics coreolis mass flow sensor RHM  
06 (Measured with water as fluid) [31] . . . . . 66

# List of Tables

3.1	Dimensions of the gravity fed evaporator loop . . . . .	20
3.2	Coefficient of resistance $\zeta$ in single-phase flow through pipe components and the experimentally determined and for tubes adjusted coefficient C from Paliwoda [30] .	21
3.3	Initialization values of the gravity-fed evaporator . . . . .	22
3.4	Initialization values of the internal heat exchanger and the gas coolers. . . . .	25
3.5	Design conditions for the gravity-fed evaporator system . . . . .	26
3.6	Measured values compared with the simulated values for the gravity-fed evaporator in the design point . . . . .	28
4.1	Design conditions for the heat pump chiller (Boundary conditions marked with *) .	40
4.2	Measured values compared with the simulated values for the gravity-fed evaporator and the ejector-fed evaporator with similar boundary conditions . . . . .	43
C.1	Controller setting for the gravity-fed evaporator system . . . . .	65
E.1	Measured values compared with the simulated values for the gravity-fed evaporator and the ejector-fed evaporator with similar boundary conditions . . . . .	67

# Table of Symbols

Abbreviation	Definition
AC	Space cooling
COP	Coefficient of performance
DHW	Domestic hot water
DX	Dry expansion evaporator
GWP	Global warming potential
HFCs	Hydrofluorocarbons
HX	Heat exchanger
IHX	Internal heat exchanger
GWP	Global warming potential
MFM	Mass flow meter
NTNU	Norwegian university of science and technology
TSEC-E	Two-stage evaporation single-stage vapor-compression cycle

Symbol	Definition	Unit
$d$	Diameter	mm
$E$	Exergy	kJ
$\dot{G}$	Mass flow density	kg/(m <sup>2</sup> s <sup>2</sup> )
$h$	Specific enthalpy	kJ/kg
$l$	Length	m
$\dot{m}$	Mass flow	kg/s
$n$	Number	n
$p$	Pressure	bar
$Q$	Heat	kJ
$q$	Specific heat	kJ/kg
$\dot{Q}$	Heat flow	kW
$S$	Entropy	kJ/K
$T$	Temperature	K
$V$	Volume	l
$\dot{W}$	Work	kW
$w$	Specific work	kJ/kg
$x$	Vapor fraction	-

<b>Symbol</b>	<b>Definition</b>	<b>Unit</b>
$\alpha$	Heat transfer coefficient	W/(m <sup>2</sup> · K)
$\beta$	Two-phase multiplier	-
$\mu$	Dynamic viscosity	(N· s)/m <sup>2</sup>
$\rho$	Density	kg/m <sup>3</sup>
$\vartheta$	Pressure drop ratio	-
$\xi$	Coefficient of resistance	-

<b>Indices</b>	<b>Definition</b>
<i>amb</i>	Ambient
<i>c</i>	Components
<i>cells</i>	Cells
<i>dc</i>	Downcomer
<i>dis</i>	Discharge
<i>Down.</i>	Downcomer
<i>Evap.</i>	Evaporator
<i>fr</i>	Frictional
<i>GC</i>	Gas cooler
<i>HP</i>	Heat pump
<i>HT</i>	High temperature
<i>i</i>	Inner
<i>in</i>	Inlet
<i>irr</i>	Irreversible
<i>L</i>	Loss
<i>LT</i>	Low temperature
<i>mot</i>	Motive
<i>n</i>	Nominal
<i>out</i>	Outlet
<i>rec</i>	Recovered
<i>Ref</i>	Refrigeration system
<i>rs</i>	Riser
<i>suc</i>	Suction
<i>t</i>	Technical
<i>w</i>	Water



# 1 Introduction

In order to meet the climate targets of the Paris Agreement, the European Union (EU), together with Norway and Iceland, is aiming for a reduction of greenhouse gas emissions (GHG). These should first be reduced to 55 % by 2030 before achieving climate neutrality in all sectors in 2050. [12] In order to achieve this, not only renewable electricity but also the thermal energy demand (heating and cooling) must be covered by renewable energies. In 2012, the thermal energy demand accounted for 51 % of final energy demand in the EU, was divided between space and process heating and cooling and domestic hot water (DHW) production [14]. In 2018, 21 % of final energy consumption for heating and cooling in the EU was already covered from renewable sources [13]. Electricity-based technologies such as heat pumps or compression refrigeration systems with natural refrigerants like CO<sub>2</sub> are already state of the art and offer a sustainable solution that can contribute to the reduction of GHG emissions [19]. In many applications, the demand for heating and cooling exists simultaneously or with only a slight time difference. Typical examples are high-performance buildings such as sports centers and hotels. Furthermore, this simultaneous need often also exists in the food industry such as on fishing vessels or in dairies. [5] One way to provide thermal energy in the form of heating, cooling and DHW simultaneously is to use a heat pump chiller (HPC). Such systems achieve a high level of energy efficiency by extracting heat from the heat source that needs to be cooled and rejecting it on the heat sink for simultaneous heating. [16]

Today's HPC available on the market frequently face issues of limited cooling capacity or require too much space. These issues are partly due to the fact that solutions that offer more cooling capacity often require two evaporators to operate efficiently. Therefore, a novel, compact, two-stage evaporator has been developed at NTNU together with SINTEF and Alfa Laval to overcome these challenges. What makes this evaporator configuration unique is the integration of a gravity-fed evaporator loop on one side of a plate heat exchanger (pre-cooling of secondary fluid) and an ejector-fed evaporator loop on the other side (after-cooling of secondary flow). The secondary loop is internally connected within the plate heat exchanger, which significantly reduces the pipework required for two separate heat exchangers. As a result, the compact two-stage heat exchanger requires less space and less connections. This results in a higher capacity per volume of the evaporator and the entire system. Furthermore, the evaporation on two pressure levels and the increase of the suction pressure of the compressor via the ejector is expected to lead to a higher system performance.

In the course of this thesis, a heat pump chiller equipped with the novel two-stage evaporator is to be investigated by means of a simulation model and subsequently validated with the aid of measurement results from the test rig. For this purpose, the state of the art of evaporator configurations used in heat pump chillers are presented. Based on the evaporator configurations, a concept for the CO<sub>2</sub> heat pump chiller was developed. Subsequently, this thesis consists of two parts. In the first part, a simulation model of the gravity-fed evaporator loop is created and extended to a heat pump chiller with only the gravity-fed evaporator. The model was built on the basis of the TIL li-

brary 3.11.0 using the Dymola simulation environment. After successful validation, a model-based investigation is carried out using the design conditions of the model and variations of these. In the second part of this thesis, the simulation model is extended by the ejector-fed evaporator in order to be able to investigate the novel two-stage evaporator by simulation. Once the model design has been completed, it is validated again with the aid of measurement data from the test rig. A model-based examination of the model is then carried out on the basis of the design conditions and variations of it. Finally, based on the knowledge gained from the model-based investigation, the performance of the two-stage evaporator with the gravity- and ejector-fed evaporator in the HPC is evaluated and a guideline for the design and operation of the novel two-stage evaporator is provided.

# 2 CO<sub>2</sub> heat pumps and refrigeration systems

A very efficient way to provide heating and cooling simultaneously is to use heat pump chillers (HPC). With HPC, both heating and cooling can be provided efficiently at the same time, as they combine the benefits of heat pumps and compression refrigeration systems. Both work according to the so-called vapor compression cycle, and absorb heat at a low temperature level and raise it with the help of an electrically driven compressor to a higher temperature level at which the heat is rejected. In the case of the heat pump, the benefit represents the heat rejected, and in the case of the refrigerating system, the benefit represents the heat absorbed. [37] In the vapor compression cycle, various refrigerants can be used as the working fluid, which undergo a phase change from liquid to gas. A distinction is made between synthetic and natural refrigerants. Synthetic refrigerants must be produced artificially and are currently used more frequently. From the group of the synthetic refrigerants, HFCs (hydrofluorocarbons) such as R-134a are the most widely used today. In addition to some advantages over natural refrigerants such as ammonia (R-717) or carbon dioxide (R-744), these have the disadvantage of a much higher global warming potential (GWP). Therefore, natural refrigerants are becoming increasingly important in the context of the EU F-Gas Regulation and the Paris Climate Agreement. [9]

The GWP of a refrigerant is indicated by the GWP<sub>100</sub> value and describes the global warming potential of a refrigerant compared to carbon dioxide over the period of 100 years in the atmosphere. According to the EU F-Gas Regulation, the emissions of fluorinated greenhouse gases must be reduced significantly by 2030 in order to protect the environment. F-Gases are (partially) fluorinated hydrocarbons that are found in synthetic refrigerants and usually have a high GWP<sub>100</sub> value. [9]

## 2.1 CO<sub>2</sub> as a refrigerant

Until the 1940s, carbon dioxide (CO<sub>2</sub>, R-744) was a widely used refrigerant, especially on ships, which was completely replaced by the emergence of synthetic refrigerants. Besides a very low GWP<sub>100</sub> value of one, CO<sub>2</sub> offers further advantages which led to its reinvention as a refrigerant under the leadership of Gustav Lorentzen in the 1980s. [9] R-744 is non-flammable, non-toxic and does not emit any environmentally harmful emissions during production. Therefore, it has the lowest direct environmental impact of all refrigerants. [19]

When looking at the fluid properties of CO<sub>2</sub>, the first thing that stands out is the low critical temperature of 31.1 °C compared to other refrigerants. In practice, this means that condensation of the refrigerant during heat dissipation in the condenser is possible only up to approximately 28 °C.

At the same time, CO<sub>2</sub> has a high critical pressure of 73.8 bar and a high triple point pressure of 5.18 bar which is above the atmospheric pressure. However, this relatively high pressure level leads to a high volumetric cooling capacity and thus to a compact design. [21] This also applies to the required displacement volume of the compressors. Compared to other refrigeration systems, these only need to be about one fifth as large for the same cooling capacity. The low pressure ratio between suction and discharge pressure also leads to a high isentropic compressor efficiency and thus to a higher energy efficiency of the overall system. [9] This leads, among other things, to the fact that CO<sub>2</sub> is outperforming all other refrigerants in terms of energy efficiency and compactness in refrigeration processes between  $-35^{\circ}\text{C}$  and  $-55^{\circ}\text{C}$ . [19] Furthermore, CO<sub>2</sub> has several fluid properties that lead to a good heat transfer. These include a high specific heat capacity, a relatively high thermal conductivity, a low viscosity and a high pressure level. Furthermore, the low surface tension of CO<sub>2</sub> causes it to bubble boiling even at low temperature differences, resulting in a high heat transfer coefficient. [21] These good properties of CO<sub>2</sub> mean that it is already state of the art as a refrigerant in Scandinavian supermarkets for simultaneous heating and cooling [17, 18, 25].

## 2.2 Thermodynamic fundamentals of the CO<sub>2</sub> vapor compression cycle

In this chapter, the thermodynamic fundamentals of the vapor compression cycle will be explained, which are necessary for the understanding of this thesis. This fundamental knowledge is already conveyed with reference to the refrigerant R-744 used in this work, but is also largely transferable to other refrigerants. These include in particular the basic subcritical as well as the transcritical vapor compression cycle.

### The basic vapor compression cycle

The vapor compression cycle is a counterclockwise thermodynamic cycle independent of the refrigerant used. It typically consists of an evaporator, a compressor, a condenser and an expansion valve. In the vapor compression cycle, the refrigerant is cyclically evaporated, compressed, condensed and expanded with the aid of mechanical energy. This is shown in Figure 2.1 using the example of refrigerant R-744 as a simple subcritical cycle. From 1 to 2, the superheated refrigerant is sucked in by the compressor and isentropically compressed. As a result of the compression, the pressure and temperature of the refrigerant increases. In the condenser, the absorbed heat is then rejected isobarically from 2 to 5. In this process, the superheated refrigerant is first cooled from 2 to 3 down to the dew point curve, from 3 to 4 it is fully liquefied, and from 4 to 5 the liquid refrigerant is subcooled. With the aid of the expansion valve, the subcooled refrigerant is then expanded from a high pressure (point 5) to a lower pressure (point 6) while the enthalpy remains constant (isenthalpic). Due to the expansion, it enters the two-phase region again and the refrigerant temperature drops. In the evaporator, the refrigerant is isobarically evaporated with the heat absorbed from heat source (6 to 1). The refrigerant is evaporated from 6 to 7 down to the dew point curve and then superheated from 7 to 1. Thus completing the thermodynamic cycle. [37]

Since the benefits of heat pumps and the refrigeration systems are different, the calculations of their respective coefficient of performance (COP) also differ. The COP is formed from the ratio of benefit to expenditure. The calculation of the COP is shown for the heat pump in equation 2.1 and for the refrigeration system in equation 2.2. The benefit of the heat pump is the specific heat rejected in the condenser  $q$  and the benefit of the refrigeration system is the specific heat absorbed by the evaporator  $q_o$ . The effort of both is the specific technical work of the compressor  $w_t$ . This is also shown in Figure 2.1 and can also be expressed by an enthalpy difference as shown in the equations 2.1 and 2.2. [37]

$$COP_{HP} = \frac{\textit{benefit}}{\textit{expenditure}} = \frac{|q|}{|q| - q_0} = \frac{|q|}{w_t} = \frac{h_2 - h_5}{h_2 - h_1} \quad (2.1)$$

$$COP_{Ref} = \frac{\textit{benefit}}{\textit{expenditure}} = \frac{|q_0|}{|q| - q_0} = \frac{|q_0|}{w_t} = \frac{h_1 - h_6}{h_2 - h_1} \quad (2.2)$$

If there is a simultaneous demand for heating and cooling, the energy efficiency can be further

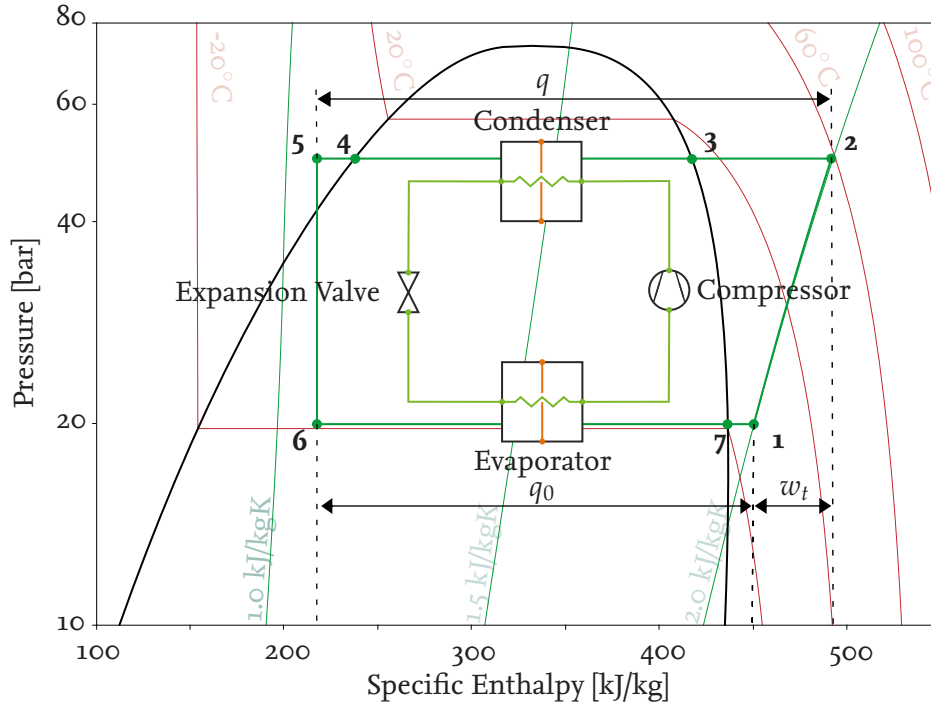


Figure 2.1: Principle sketch of the simple subcritical CO<sub>2</sub> vapor compression cycle in a p, h diagram

increased by a combined operation of one system (e.g. a heat pump). Via the evaporator, heat is extracted from an object to be cooled on the heat source side and, with the help of the condenser, supplied to the heat sink that requires heat. In this thesis, this mode of operation is called heat pump chiller. The resulting combined  $COP_{comb}$  is calculated as shown in the equation 2.3 below: [16]

$$COP_{comb} = COP_{HP} + COP_{Ref} = \frac{|q| + |q_0|}{w_t} = \frac{(h_2 - h_5) + (h_1 - h_6)}{h_2 - h_1} \quad (2.3)$$

When the specific enthalpy difference of the heat sink is multiplied by the refrigerant mass flow rate, the heating capacity that is rejected by the condenser is obtained, as can be seen in equation 2.4. For the cooling capacity extracted from the heat source by the evaporator, the calculation is done in the same way as shown in equation 2.5. [37]

$$\dot{Q} = \dot{m} \cdot (h_2 - h_5) \quad (2.4)$$

$$\dot{Q}_0 = \dot{m} \cdot (h_1 - h_6) \quad (2.5)$$

## The transcritical vapor compression cycle

If the pressure exceeds the critical pressure, the heat can no longer be rejected to the heat sink by means of a phase change. In the transcritical range, the CO<sub>2</sub> is present as a supercritical fluid with a very high density. When the temperature drops, the supercritical CO<sub>2</sub> behaves similarly to a liquid. Therefore, the heat exchanger responsible for heat rejection is called a gas cooler (GC) in the transcritical operation. [9] Since, unlike in the subcritical range, isothermal and isobaric are not in congruence, the transcritical process results in heat dissipation with a continuously gliding temperature. The course of the isotherms (red) can be traced on the basis of Figure 2.2 a). For example, the isotherm  $T_{GC}$  represents the exit temperature of the refrigerant from the gas cooler, but not the temperature of the total isobaric heat dissipation (2 to 3). [28] Although this temperature glide is not desired for all applications, it offers advantages especially when a large temperature lift is required on the heat sink side. This is the case, for example when heating domestic hot water. Therefore, CO<sub>2</sub> heat pumps are especially used in this field of application. [9]

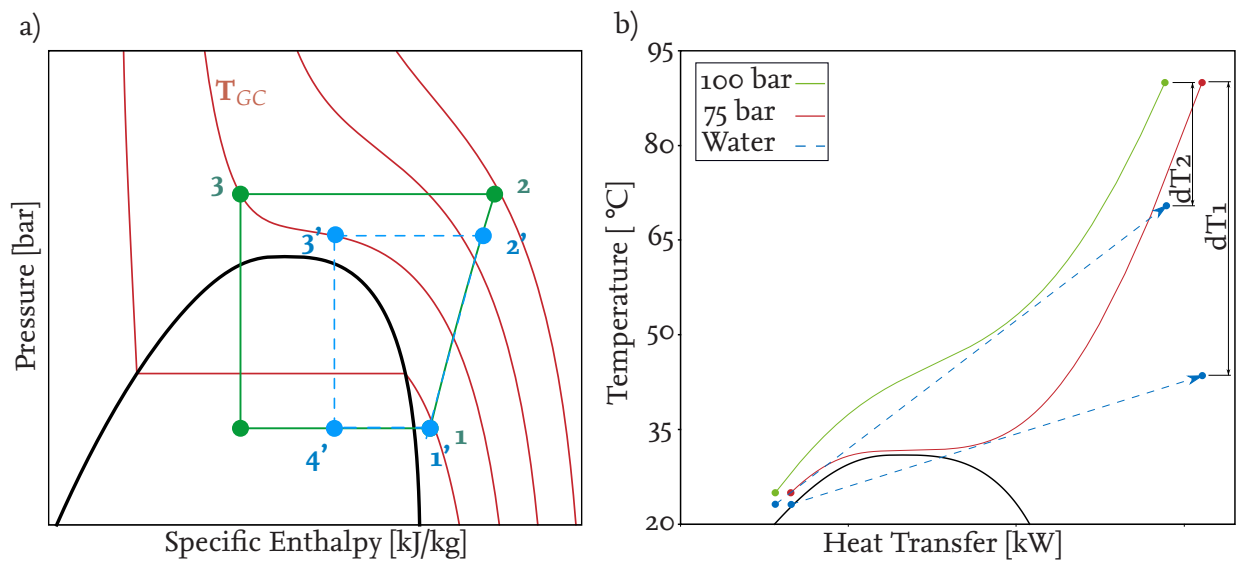


Figure 2.2: Principle sketches of transcritical CO<sub>2</sub> vapor compression cycles a) in the p,h diagram to illustrate the optimal high pressure and b) an optimization of heat rejection in the gas cooler at two different pressures.

For heat dissipation above the critical point, pressure and temperature can be selected independently. Figure 2.2 a) shows how, at the same gas cooler exit temperature ( $T_{GC}$ ), there are two different pressures for the Green and Blue cycles of heat dissipation. If the COP of the two processes is calculated according to equation 2.1, it becomes clear that with relatively little more effort for the compressor ( $h_2-h_1$ ), considerably more benefit is generated via the significantly larger enthalpy difference ( $h_2-h_3$ ) of the green process. Where the gas cooler pressure ideally lies depends on many factors. The ideal pressure for heat dissipation of transcritical systems is also referred to as the optimum high pressure and leads to higher energy efficiency. [28]

However, as can be seen from Figure 2.2 b), the optimum pressure must also be taken into account for optimum heat rejection by utilizing the temperature glide of transcritical CO<sub>2</sub>. In the

figure, water should be heated to the maximum with the help of the gas cooler from 23 °C. At a high pressure of 75 bar, the isobar has an extended saddle point, so that the pinch point, i.e. the point with the lowest temperature difference in the heat exchanger, is already at about 34 °C. These two aspects lead to a flat temperature rise of the water. Thus, when the water leaves, a large temperature difference  $dT_1$  remains with respect to the entry of the CO<sub>2</sub> into the gas cooler. For 100 bar, on the other hand, the pinch point is much higher, since the isobar is steeper and without a saddle point. Therefore, the water can be heated much further and the temperature difference  $dT_2$  between water outlet and CO<sub>2</sub> inlet decreases significantly compared to  $dT_1$ . [9]

To determine the optimum high pressure, various correlations can be used, some of which are adapted to the structure of the circuit and the intended use. A list of different correlations can be found in the paper by Yang et al. [38]. They use, among others, the outside temperature ( $T_{amb}$ ) or the gas cooler outlet temperature ( $T_{GC}$ ) for the calculation of the optimal high pressure.

## 2.3 Process improvement for CO<sub>2</sub> vapor compression cycles

Many options for improving CO<sub>2</sub> vapor compression cycles can be found in the literature. The extent to which these are useful depends on the potential energy savings, cost, and complexity of the improvement. In the following, improvements are presented that have been applied in this work and are therefore relevant for understanding.

### Internal heat exchanger

Using an internal heat exchanger (IHX) has several advantages when using CO<sub>2</sub> as a refrigerant. The two-phase refrigerant leaving the evaporator can be fully evaporated and then superheated in the IHX from point 0 to point 1. This is done by transferring the heat of the refrigerant leaving the gas cooler from 3 to 4. [28] Thus, the use of an IHX allows the evaporator to operate without superheating while protecting the compressor from liquid slugging. Based on the fluid properties of CO<sub>2</sub>, superheating in the evaporator should be avoided in efficient systems, if possible. Due to the ratio of temperature to pressure in the gas region, superheating by 1 K causes a decrease in evaporating pressure by almost 1 bar which leads to more work in the compressor and thus to lower efficiency. [9] Furthermore, an IHX causes the refrigerant to be further cooled or subcooled after leaving the gas cooler/condenser before it is expanded to the evaporating pressure. This can further increase the specific cooling capacity of the process. Thus, the refrigeration system performance  $COP_{Ref}$  can also be increased further, as can also be seen in Figure 2.3. [28] In systems with a low-pressure receiver downstream of the evaporator, the IHX is also used to ensure oil return to the compressor [9].



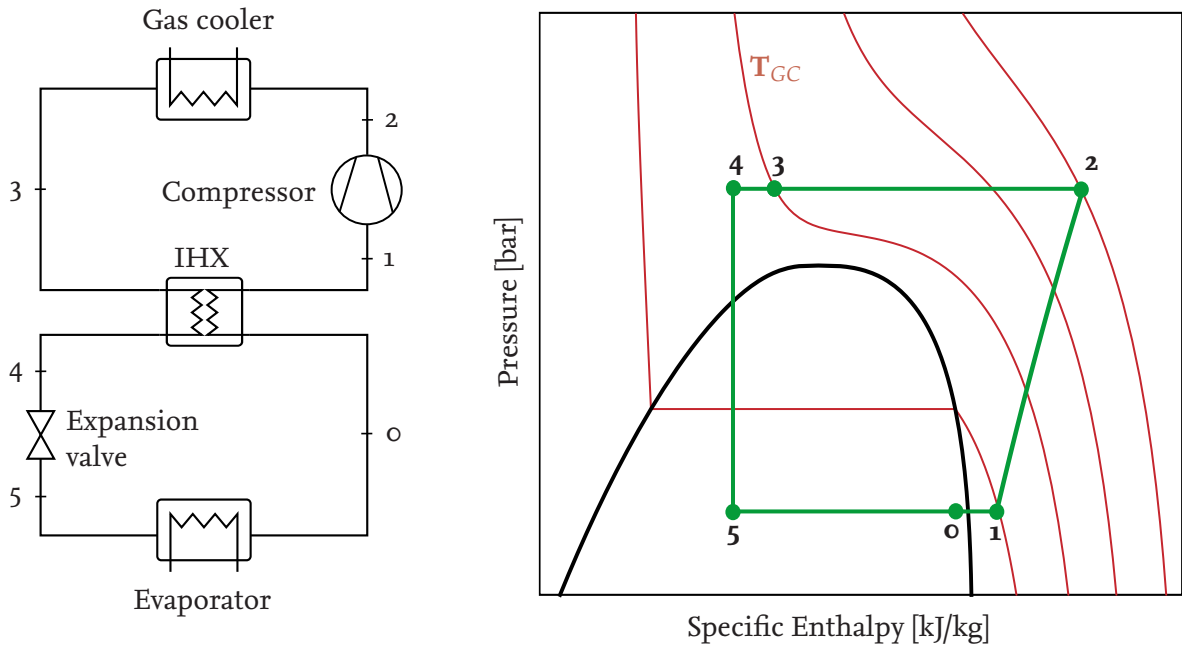


Figure 2.3: Principle sketch of the transcritical CO<sub>2</sub> vapor compression cycle with an internal heat exchanger in a p, h diagram

### Ejector in CO<sub>2</sub> Systems

Typically, the expansion is carried out with the aid of an expansion valve. In this process, the refrigerant is expanded isenthalpically (constant enthalpy) from a high pressure to a lower pressure, as already shown in Figure 2.2. This results in very high throttling losses, especially with transcritical CO<sub>2</sub> at high ambient temperatures. To prevent this, an ejector can be used by utilizing the expansion work to recompress the CO<sub>2</sub>. The performance of such an ejector depends strongly on its geometry and the operating conditions (high pressure and ambient temperature). [11] In an experimental study by Lucas et al. [27], the COP of the refrigeration system could be increased by up to 17% by using an ejector compared to an expansion valve. The structure of such an ejector is shown in Figure 2.4 a). It has no moving components and consists of a nozzle, a mixing chamber and a diffuser. The working principle of this system is the isentropic conversion of pressure energy into kinetic energy. Two mass flows enter the ejector. The motive flow and the suction flow. The motive flow enters the nozzle at high pressure coming from the gas cooler and is expanded and strongly accelerated. When it leaves the nozzle, the pressure of the motive flow is below that of the fluid to be sucked in. This can be seen in the drawing in Figure 2.4 a), which shows the qualitative pressure curve over the construction length. This creates a vacuum through which the suction mass flow is sucked in. In the mixing chamber, the driving mass flow  $\dot{m}_{mot}$  and the suction mass flow  $\dot{m}_{suc}$  meet and are decelerated to a common velocity and mixed to form the discharge mass flow  $\dot{m}_{dis}$ . This results in an increase in pressure. Subsequently, a continuous expansion of the diameter in the diffuser leads to a further increase in pressure until the refrigerant exits the ejector. The state changes with the isentropic expansion and the pressure increase in the ejector can also be seen in the p,h diagram in Figure 2.4 b). The green lines represent isentropes. [9]

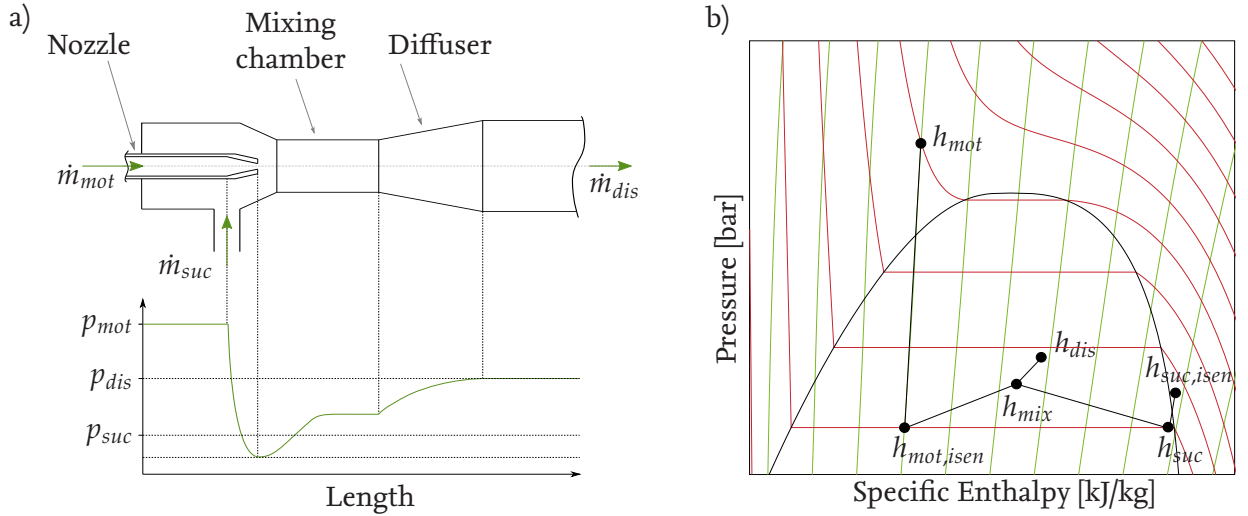


Figure 2.4: Principle sketch of the design of an ejector with its qualitative pressure curve over the construction length a) and the qualitative state change in the p,h diagram b)

In the study by Elbarghthi et al. [11] ejectors were tested experimentally. It was found that up to 36.9% of the throttle losses could be recovered by an ejector. Depending on the operating conditions, the suction pressure  $p_{suc}$  can be 1 bar to 10 bar below the discharge pressure  $p_{dis}$  and thus reduce the load on the compressor. To be able to determine how well an ejector works under given boundary conditions, the ejector efficiency was defined. This can be seen in equation 2.6 and indicates how much expansion work  $\dot{W}_{rec}$  could be recovered using the ejector compared to the maximum possible recovery work  $\dot{W}_{rec,max}$ . The recovered expansion work is composed of the suction mass flow  $\dot{m}_{suc}$  and the enthalpy difference of the isentropic compression ( $h_{suc,isen} - h_{suc}$ ). The maximum possible recovered expansion work consists of the motive mass flow  $\dot{m}_{mot}$  and the enthalpy difference of isentropic expansion ( $h_{mot} - h_{mot,isen}$ ). A quantitative representation of the condition points required for calculating the ejector efficiency are shown in Figure 2.4 b). [11] Typical values for ejector efficiency at the design point range from 30% to 35% [9].

$$\eta_{jec} = \frac{\dot{W}_{rec}}{\dot{W}_{rec,max}} = \frac{\dot{m}_{suc} \cdot (h_{suc,isen} - h_{suc})}{\dot{m}_{mot} \cdot (h_{mot} - h_{mot,isen})} \quad (2.6)$$

## 2.4 Evaporator configurations

As already seen in chapter 2.2, the evaporation of the refrigerant takes place in the two-phase region. With the help of a heat exchanger, thermal energy is extracted from a heat source and absorbed in the refrigerant, whereby the refrigerant evaporates. Therefore, this heat exchanger is also called an evaporator. A basic distinction can be made between two categories of evaporators. On the one hand the dry expansion evaporators (DX), on the other hand the flooded evaporators. [26] In this chapter, the two evaporator categories will be each explained in more detail and then compared to each other. Following this, various other evaporator configurations that are necessary for the understanding of this thesis will be presented.

### Comparison between a dry expansion evaporator and a flooded evaporator

The DX is a evaporator configuration for small and medium refrigeration systems. After full evaporation, 10 – 30 % of the heat exchanger surface is used to superheat the refrigerant [34]. This superheat typically ranges between 5 – 10 K and is usually controlled by a thermostatic or electronic expansion valve.[28] The superheat is used to protect the downstream compressor from liquid slugging and thus extend its lifetime. Another advantage of a DX system is the automatic oil return. [26] A disadvantage is that between 95 – 99 % of the refrigerant volume is already gaseous when flowing into the evaporator. This leads to poor liquid contact and thus to poor heat transfer. [26] This can also be shown by the study results of Cheng et al. [8]. In this paper, the influence of vapor fraction on the heat transfer coefficient of  $\text{CO}_2$  in pipes was investigated and a new flow boiling heat transfer model for  $\text{CO}_2$  was established and compared with experimental data for different boundary conditions. As can be seen from Figure 2.5, it was shown that the heat transfer coefficient of  $\text{CO}_2$  is relatively constant high at  $10\text{--}16\text{ kW m}^{-2}\text{ K}^{-1}$  for vapor fraction from 0 % to about 70 % , depending on the boundary condition considered. Thereafter, the heat transfer coefficient drops steeply until it reaches a low plateau of about  $0.1\text{--}1.7\text{ kW m}^{-2}\text{ K}^{-1}$  at about 80– 90 % vapor fraction, which continues until 100 %. [8] Furthermore, the vapor fraction also has a great influence on the pressure drop inside the evaporator. As the vapor fraction increases, so does the pressure drop. [23]

Unlike DX systems, flooded evaporators are supplied with liquid refrigerant from a separator and are operated without superheating. They can be divided into two categories. Flooded evaporators with and without liquid circulation. Evaporators without liquid circulation are, for example, shell and tube heat exchangers, which will not be discussed further in this work.

For evaporators with circulation a distinction can be made between forced and natural circulation. This can be seen in Figure 2.6. Those with forced circulation a), e.g. by a pump or ejector and those with natural circulation b), also called gravity-fed evaporators. [28] In both systems with liquid circulation, the liquid coming from the high pressure side is first collected in a receiver after throttling. There, the liquid and gaseous phases are separated from each other so that only liquid refrigerant enters the evaporator. In case a), the evaporator is fed by the pump. This regulates the refrigerant mass flow and thus also the vapor fraction at the outlet of the evaporator. As with the

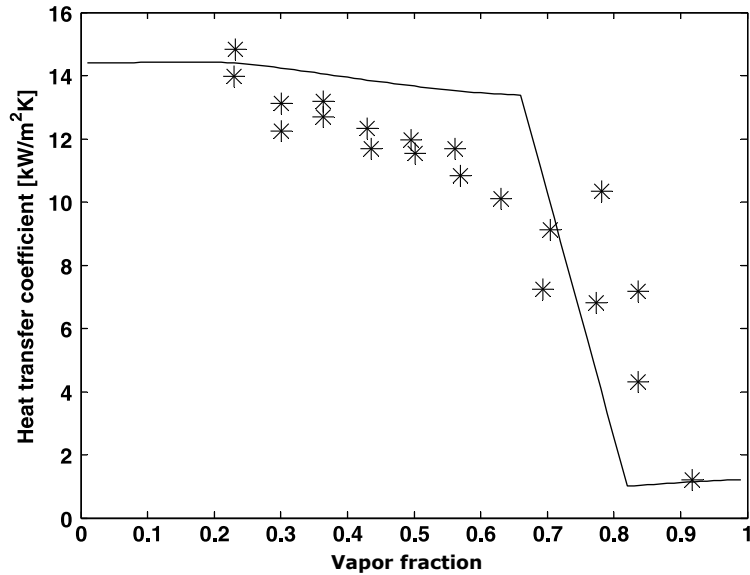


Figure 2.5: Heat transfer coefficient of CO<sub>2</sub> during evaporation in horizontal tubes,  $d = 3$  mm,  $G = 390 \text{ kg m}^{-2} \text{ s}^{-1}$ ,  $q = 20 \text{ kW m}^{-2}$  from Cheng et al. [8]

gravity-fed evaporator, this should preferably be around 80 % in order to obtain a good heat transfer coefficient and a low pressure drop, and at the same time to obtain a circulation number that is not too high. The circulation number is formed from the reciprocal of the vapor content at the evaporator outlet and, due to the lack of superheating, tells how many times the refrigerant must pass through the evaporator circuit to evaporate completely. For Plate heat exchanger the circulation number should be between 1.1 ( $x_{out}=0.91$ ) to 1.4 ( $x_{out}=0.71$ ). [34] Due to the better heat transfer and the elimination of superheating, the temperature difference between the secondary fluid and the evaporating temperature can be smaller. Therefore, flooded evaporators can be operated with an evaporating temperature that is 6 - 8 K above the DX system. [17] Since the ratio of saturation pressure to saturation temperature of CO<sub>2</sub> is almost 1, the evaporation pressure can be chosen higher. This results in less compressor work being required and thus increases the overall performance (COP) of the system. [9] The gravity-fed evaporator b) operates according to the thermosyphon principle via a density difference between the inlet and outlet state of the refrigerant in the evaporator. In addition, the liquid column  $H$  leads to a slight increase in pressure. The natural circulation works only if the thermosyphon principle overcomes the major pressure drop inside the evaporator and the piping and the minor pressure drop of the Bends and changing tube diameters (cross section area). Therefore, it is important that the system is designed properly. [29] The gravity-fed evaporator will be discussed in more detail in Chapter 3.1. Among many advantages of a flooded evaporator, the incomplete evaporation of the refrigerant leads to a higher refrigerant charge which can be disadvantageous, for instance, when installation restrictions are imposed due to refrigerant charge limits. Comparable DX systems require significantly lower refrigerant charges. Furthermore, a system with a flooded evaporator requires higher installation costs since more components such as receivers and more piping are needed. [34]

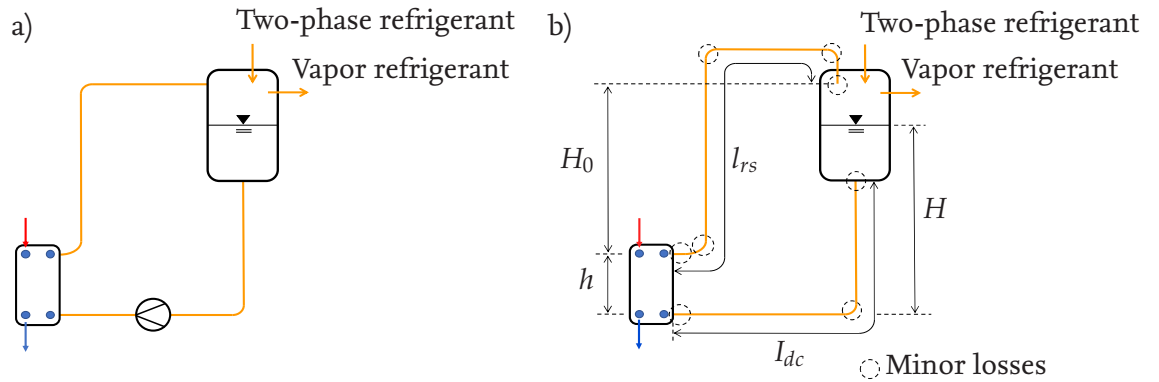


Figure 2.6: Schematic diagram of flooded evaporators a) with forced circulation and b) with natural circulation

### Two-stage evaporator system

During evaporation, the heat flux flows from the warmer heat source to the colder refrigerant, causing it to evaporate. In reality, this process requires a driving temperature difference. However, this temperature difference can be small. A small temperature difference offers thermodynamic advantages, since the heat transfer approaches the ideal reversible heat transfer as the temperature difference decreases. [3] If a heat source has to be cooled from a temperature  $A$  to a temperature  $B$ , this can be done with a single-stage evaporator as shown in Figure 2.7 a) or with several parallel evaporators at different temperature levels, through which a secondary fluid flows in series and is gradually cooled. This is illustrated by the example of a two-stage evaporation in Figure 2.7 b). The two-stage evaporation can reduce the maximum temperature difference that occurs between the secondary fluid entering and the refrigerant leaving. Thus, the irreversible losses that occur during heat transfer from one fluid with the Temperature  $T_1$  to another fluid with the temperature  $T_2$  ( $T_2 < T_1$ ) in real processes are reduced. These thermodynamic losses are called exergy loss or exergy destruction and occur due to entropy production. The exergy loss  $dEx_L$  is defined in Equation 2.7 where  $T_{amb}$  represents the ambient temperature,  $dQ$  the heat transferred from the hot fluid to the cold fluid and  $dS_{irr}$  the irreversible entropy change. [33]

$$dEx_L = T_{amb} \cdot dQ \cdot \frac{T_1 - T_2}{T_1 \cdot T_2} = T_{amb} \cdot dS_{irr} \quad (2.7)$$

Therefore it can be concluded from Equation 2.7 that if the temperature difference that occurs during heat transfer is reduced by a two- or multi-stage heat transfer, that this also reduces the exergy destruction.

In the following, some ejector-driven two-stage evaporator concepts that can be found in the literature are presented. These are compared in Figure 2.8. All presented concepts cool the secondary fluid (blue dashed line) in two stages. As already presented in Figure 2.7 b), this is done with the aid of two evaporators at different pressure and temperature levels. In the report by Gabriellii [16], a heat pump chiller is used in an Indian centralized kitchen to preheat the cooking water to  $90^\circ\text{C}$  and to provide space cooling (AC). For space cooling, the secondary fluid is cooled in two stages from  $12^\circ\text{C}$  to  $5^\circ\text{C}$ . For this purpose, the evaporator configuration shown in Figure 2.8 a) is used. The secondary fluid is first precooled in the evaporator operated with the ejector discharge mass

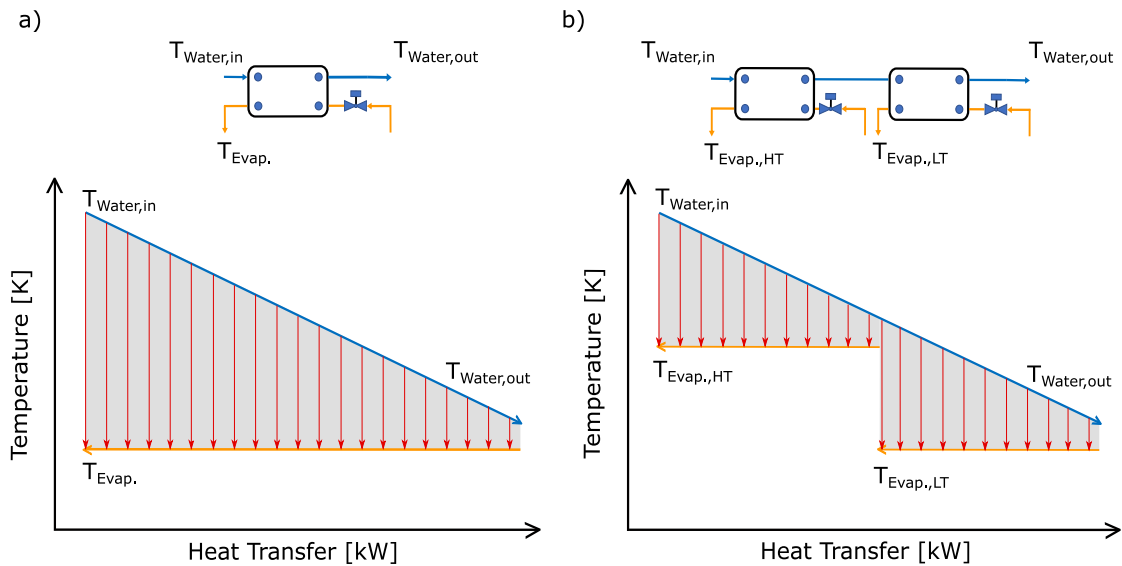


Figure 2.7: Schematic temperature heat transfer diagram of a single stage evaporator a) and a two-stage evaporator b)

flow. It is then cooled to the desired temperature by the evaporator through which the suction mass flow of the ejector flows. [16] In the study by Cao et al. [6] the influence of different evaporator configurations on the coefficient of performance (COP) of R410A vapor compression cycle was investigated and compared. In addition, an exergy analysis was performed for the four state changes: compression, condensation, expansion and evaporation. This made it possible to show the influence of the configuration on the exergy losses for the various state changes. Furthermore, the investigation was repeated for four other refrigerants for a general significance independent of the refrigerant. Among them also R744. It was found that a ejector-assisted two-stage evaporation single-stage vapor-compression cycle as shown in Figure 2.8 b) (abbreviated as TSEC-E in Coa et al.) that enables the two temperature levels through an ejector works most efficiently when a large temperature glide is required for the heat source. At small temperature glides, unequal mass flow distribution through the ejector to both evaporators results in greater exergy losses than in single-stage systems. Although the TSEC-E configuration increases the COP for all refrigerants considered, it is most effective for the transcritical  $\text{CO}_2$  vapour compression cycle. This is mainly due to the fact that the very high expansion losses of  $\text{CO}_2$  can be reduced by the ejector, as already shown in Chapter 2.3. [6]

Another evaporator configuration (Figure 2.8 c) ) is used in several publications related to the MultiPACK project [2, 10, 36]. The first evaporator is gravity fed and the second one is ejector fed. In the study by Tosato et al. [36] a heat pump chiller for heating, cooling and domestic hot water (DHW) was installed and monitored in a hotel facility in Italy and the data was evaluated. It was found that at low demand (partial load), most of the load was on the gravity-fed evaporator. At the same time, the refrigerant in the ejector fed evaporator exits at high superheat. When the demand increases, the ejector fed evaporator takes on more load and can thus be operated almost without overheating. At the same time, the load absorbed by the gravity-fed evaporator decreases. Howev-

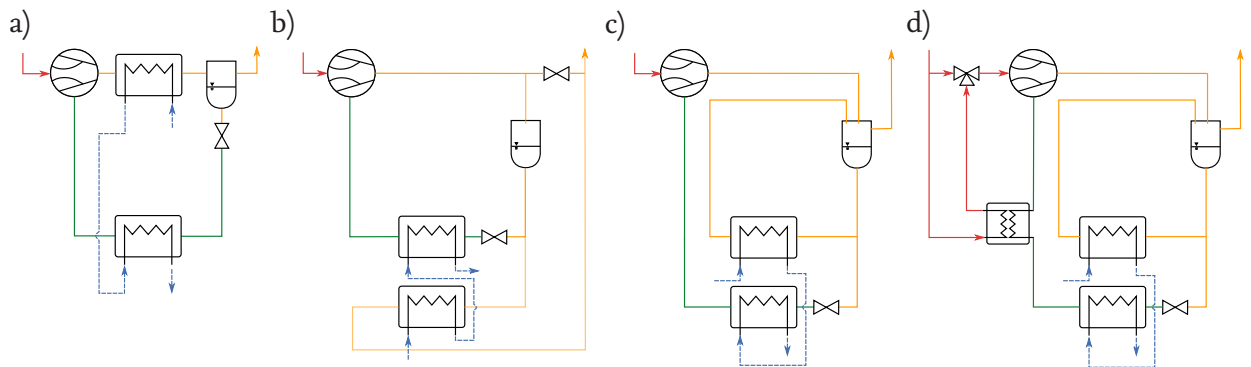


Figure 2.8: Schematic illustration of different two-stage evaporator configurations for heat pump chillers: a) is an ejector operated two-stage evaporator from [16] where one evaporator is operated with the ejector discharge mass flow and the other with the suction mass flow, the configuration b) from [6] and the configuration c) from [2] are both two-stage evaporator configurations where the first evaporator is gravity-fed and the second is driven by the suction mass flow of the ejector and d) from [32] is an extended configuration of c) using an IHX to superheat the suction mass flow of the ejector.

er, the reason for this still needs to be investigated. Nevertheless, the measured data have shown that a heat pump chiller with two-stage evaporation is a reasonable solution for the thermal energy demand of a hotel.[36] An extended version of the evaporator configuration considered in the MultiPACK projects is presented in Smitt et al.[32]. The study considers different configurations of CO<sub>2</sub> heat pump chillers for heating, cooling and DHW. A comparison of the configurations is made for eight different locations in Europe based on the year COP. The best configuration is shown in Figure 2.8 d). In addition, a payback period is given for each location based on the annual simulation. In order to operate the ejector driven evaporator with low superheat and still be able to use a vapor ejector, an IHX is used. This IHX is flown through on one side by a part of the ejector motive flow and on the other side by the suction flow of the ejector. The ejector fed evaporator is operated 4 bar to 6 bar below the gravity-fed evaporator. In the process, the cooling load is determined on the basis of the secondary fluid mass flow and the pressure in the separator. The secondary fluid mass flow is controlled to the desired outlet temperature. [32]

### Novel two-stage evaporator

As mentioned in the previous section, some two-stage evaporator systems already exist. Current heat pump chiller systems are limited by the larger footprint of two heat exchangers and extra piping. Therefore, NTNU, SINTEF and Alfa Laval have joined forces and developed a two-stage evaporator consisting of two identical brazed plate heat exchangers. These were assembled back to back as a 'sandwich'. The result can be seen in Figure 2.9 a). A slightly thicker intermediate plate separates the two HXs, which is shown as dashed lines in Figure 2.9 a) and b). The secondary loop was connected internally, so that only two connections have to be made for it. This can be seen in figure 2.9 b). Warm water (light blue) enters the HX at the top right, is cooled down and exits cold at the top left (dark blue). This saves additional piping and results in a compact two-stage evaporator system. This novel two-stage evaporator is designed to increase the volumetric cooling load of heat

pump chillers due to its compact design.

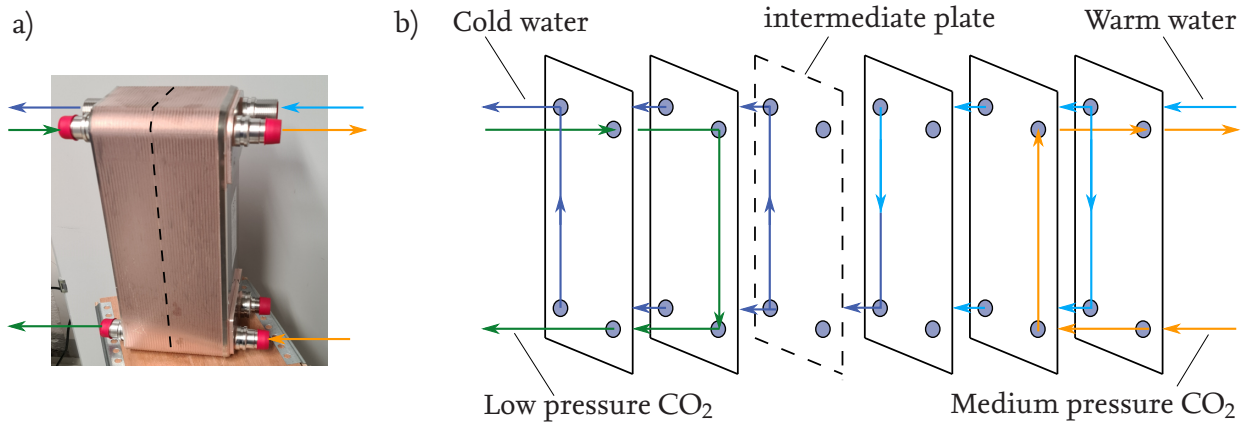


Figure 2.9: Picture of the novel two-stage evaporator prototype from Alfa Laval a) and simplified principle sketch of its working principle b)

In Appendix A, you can see the setup of the test rig in which the prototype is examined by measurement. The measurement results are used in the model design of chapters 3 and 4 for the validation of the simulation model. For a detailed discussion of the measurement results, please refer to the conference paper by Hafner et al. [20] and the master's thesis by Hafsås [22].



## 2.5 Design of the heat pump chiller to be investigated

This chapter describes the design of the heat pump chiller under investigation. A schematic drawing of the heat pump chiller is shown in Figure 2.10. This consists of the two-stage evaporator circuit already shown in figure 2.7 c). The gravity-fed evaporator is operated at the pressure of the separator (medium pressure). Similarly, the ejector-fed evaporator is operated with the suction mass flow of the ejector at low pressure. Water flows as a secondary fluid first through the gravity-fed evaporator, where it is pre-cooled, and then through the ejector-fed evaporator, where it is further cooled to the outlet temperature. Saturated steam is sucked from the separator by the compressor and is superheated by the internal heat exchanger (IHX) on its way to the compressor inlet. With the help of the compressor, the CO<sub>2</sub> is compressed to high pressure and heats up in the process. In the two gas coolers (GC), the CO<sub>2</sub> is then cooled by transferring the heat to another secondary fluid (water). This represents the heating of domestic hot water (DHW) and flows in series through both GCs. The CO<sub>2</sub> exiting the two gas cooler is then further cooled using the IHX before entering the ejector as motive flow. In the ejector, the motive flow is expanded, mixed with the low pressure suction flow and then enters the separator together as a discharge flow at medium pressure level.

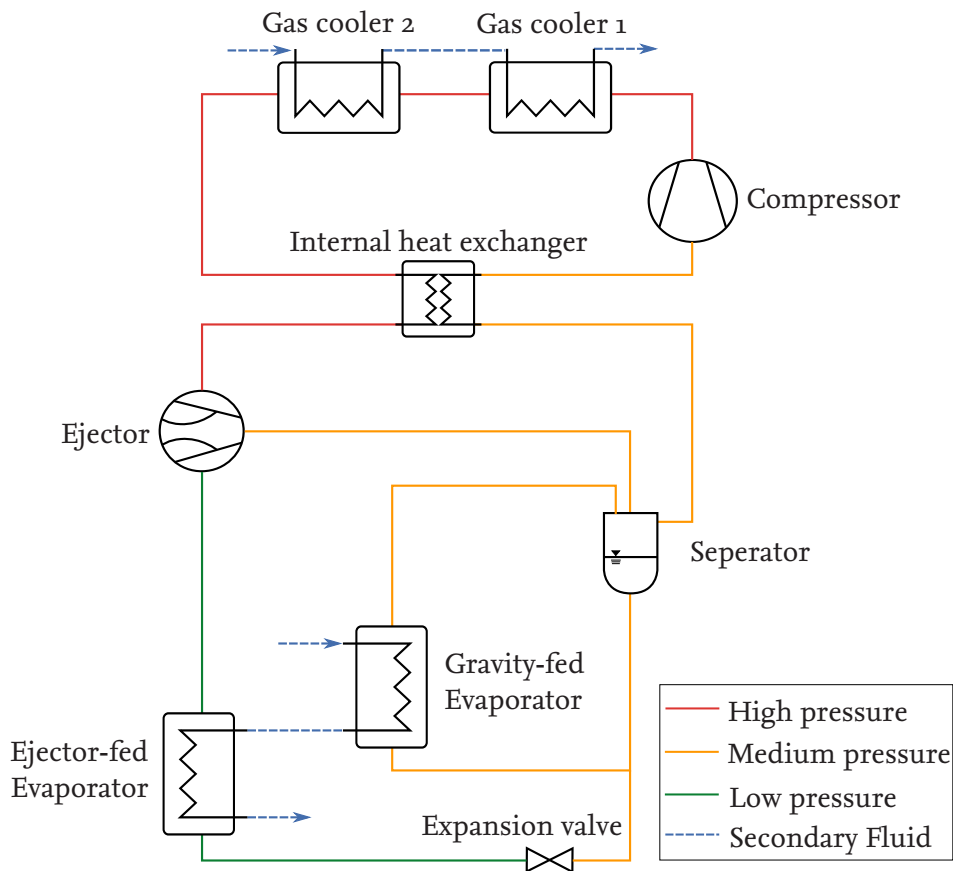


Figure 2.10: Schematic drawing of the heat pump chiller with two-stage evaporation

# 3 The gravity-fed evaporator system

In the scope of this thesis, a novel compact two-stage evaporator will be investigated. This chapter deals with the construction and validation of the simulation model for the self circulating refrigeration loop, which is also known as a gravity-fed evaporator loop. In order to simulate a thermal energy unit with a gravity-fed evaporator, a model must first be built that takes into account all the important physical processes within the evaporator unit. The simulation is performed using the modeling language Modelica, the program Dymola in version 2020x with its standard solver Dassl and the thermal model library TIL/TILMedia (version 3.11.0) from TLK-Thermo GmbH. The model library contains components that can be individually adapted and extended to the required level of detail and TILMedia is providing the fluid properties. In order to be able to adapt the components to the requirements of the gravity-fed evaporator loop, the structure with all the important equations are described in this chapter. A schematic diagram of the refrigeration circuit considered in this chapter is shown in Figure 3.1 and includes, in addition to the gravity-fed evaporator loop, an internal heat exchanger (IHX), a compressor, two gas coolers/condensers and a throttle valve.

## 3.1 Model design and parameterization

At the beginning of the model design, the structure of the gravity-fed evaporator model is presented first. The resulting evaporator loop model is then used to build the model of the refrigeration cycle as already shown in Figure 3.1.

### Gravity-fed evaporator loop

The already mentioned design of the flooded evaporator in the form of a gravity-fed evaporator has been proven for a long time, especially for ammonia [23, 29]. The design of a gravity-fed evaporator can be seen in Figure 3.2. It typically consists of a separator, a downcomer, a heat exchanger, and a riser. The saturated liquid flows from the separator via the downcomer to the evaporator inlet. The hydrostatic pressure of the liquid column  $H$  increases the pressure at the evaporator inlet, thus slightly subcooling the liquid. The pressure gain can range from 0.05 bar to 0.5 bar, depending on the height difference  $H$ . In the evaporator, heat is transferred from the secondary fluid to the refrigerant as these two fluids flow in counter current direction. As a result, part of the refrigerant is evaporated until it leaves the evaporator, without superheating. The partial evaporation causes a change in density, which leads together with the pressure gain in the downcomer to the thermosyphon effect. [34] In the gravity-fed evaporator, the liquid circulates naturally due to this thermosyphon effect. Therefore, the system must be designed so that all minor and major pressure losses are overcome by the thermosyphon effect, so that the two-phase refrigerant can flow back

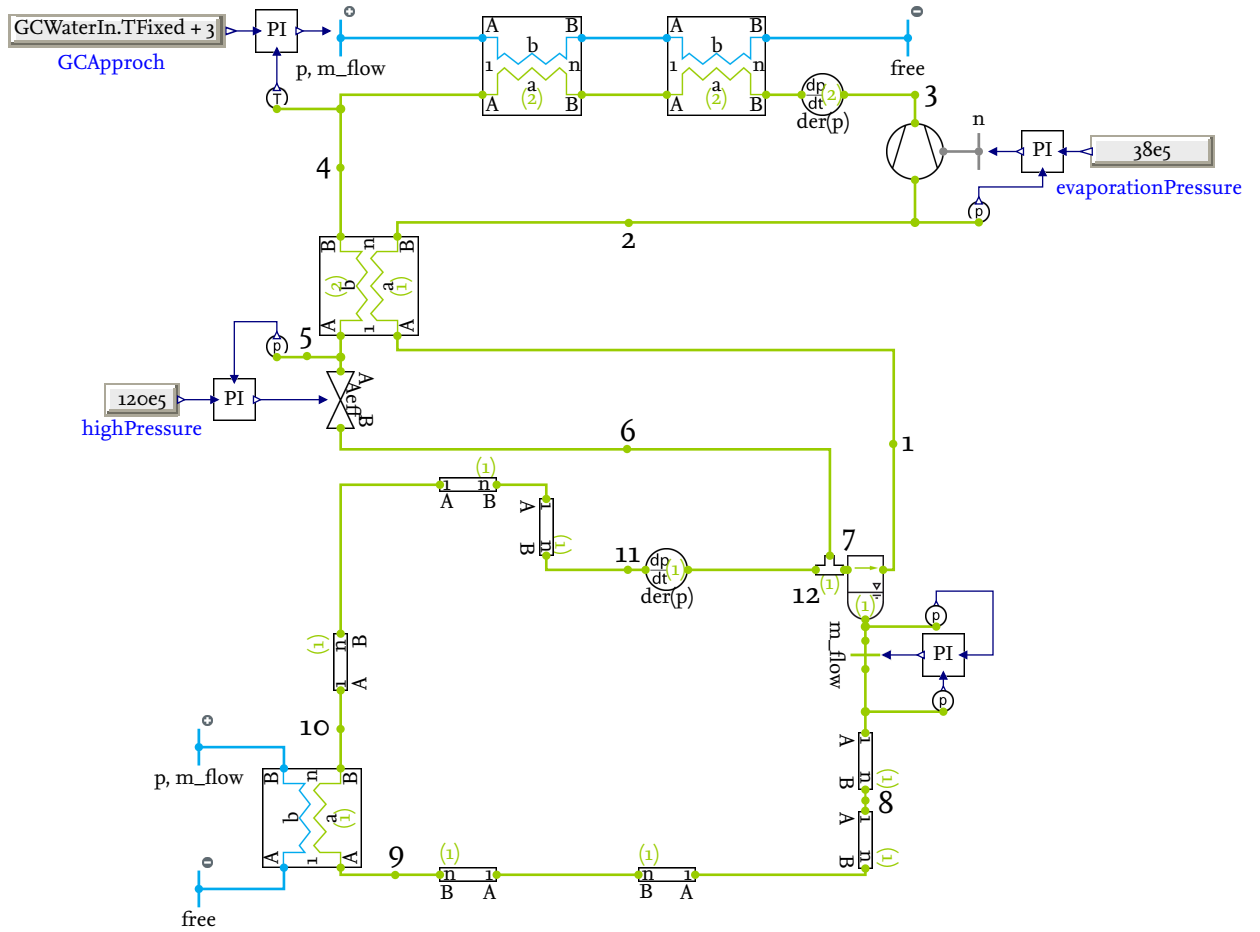


Figure 3.1: Schematic diagram of the refrigeration system with the gravity-fed evaporator loop in Dymola (Green lines: CO<sub>2</sub>, Light blue lines: water)

into the evaporator. [29] The frictional resistances in the pipes give rise to the major losses while the change in flow-direction/flow-area (bends and cross-section area) gives rise to the minor losses. The dimensions of the gravity-fed evaporator loop shown in Figure 3.2 can be found in Table 3.1. These correspond to the dimensions of the test setup on the test rig in the laboratory which was described in the master's thesis by Hafsås [22].

When the heat load of the evaporator is  $\dot{Q} = 0$ , then the liquid level in the riser is  $H$  since the thermosyphon effect does not occur. If  $\dot{Q} > 0$ , the refrigerant in the evaporator starts to boil and evaporate, creating a two-phase fluid with a density difference between the inlet and outlet of the evaporator. Thus, the thermosyphon effect takes place and the two-phase fluid can flow into the separator under the condition that all pressure losses are overcome. This condition is shown in equation 3.8. [29]

$$H \cdot \rho' \cdot g - h \cdot \rho_{ev} \cdot g - H_0 \cdot \rho_0 \cdot g = \Delta p_{dc;fr} + \sum \Delta p_{dc;c} + \Delta p_{ev;fr} + \sum \Delta p_{ev;c} + \Delta p_{rs;fr} + \sum \Delta p_{rs;c} \quad (3.8)$$

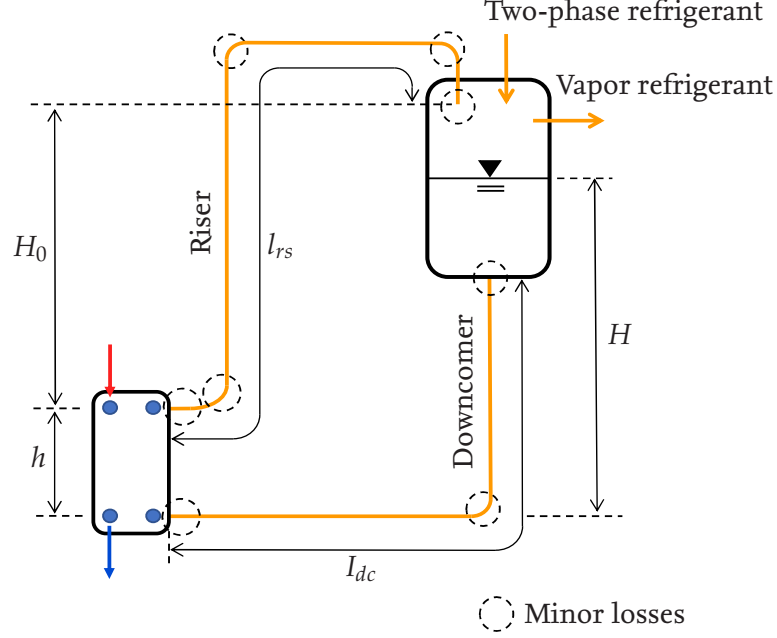


Figure 3.2: Schematic diagram of the gravity-fed evaporator loop

Table 3.1: Dimensions of the gravity fed evaporator loop

Dimensions			
Height downcomer	$H$	0.795	m
Length downcomer	$l_{dc}$	1.5	m
Height evaporator	$h$	0.42	m
Height riser	$H_0$	0.63	m
Length riser	$l_{rs}$	2.15	m
Pipe diameter	$d_i$	0.014	m
Separator volume	$V$	210	l

On the left side of the equation, the hydrostatic pressure is calculated and subtracted from each section (i.e. downcomer, evaporator, and riser) with the different densities ( $\rho$ ), the gravitational acceleration on earth ( $g$ ) and different heights of the sections (as shown in Figure 3.2). On the right side of the equation,  $\Delta p$  represents all pressure losses in the section of the circuit. This means for major ( $\Delta p_{xx;fr}$ ) and minor ( $\Delta p_{xx;c}$ ) pressure losses. The frictional (major) pressure losses in the downcomer are to be calculated as a single-phase flow according to the Blasius formula as shown in equation 3.9.  $\mu$  represents the dynamic viscosity of the refrigerant,  $\dot{m}$  the refrigerant mass flow,  $l_{dc}$  the length of the downcomer and  $d_i$  the inner diameter of the tube. The pipe length and diameter can be obtained from Table 3.1. [29]

$$\Delta p_{dc;fr} = \frac{0.3164}{2} \cdot \frac{\mu'^{0.25}}{\rho'} \cdot \dot{m}^{1.75} \cdot \frac{l_{dc}}{d_i^{1.25}} \quad (3.9)$$

The minor pressure losses in the components due to change in the flow-direction/flow-area in the downcomer are to be calculated as single-phase flow as seen in equation 3.10: [30]

$$\Delta p_{dc;c} = \xi \cdot \frac{\dot{G}^2}{2 \cdot \rho'} \quad (3.10)$$

The respective values for the coefficient of resistance  $\xi$  of the different components for the calculation of the pressure loss can be taken from Table 3.2. Furthermore,  $\dot{G}$  in the equation stands for the mass flow density.

Table 3.2: Coefficient of resistance  $\xi$  in single-phase flow through pipe components and the experimentally determined and for tubes adjusted coefficient C from Paliwoda [30]

Component	$\xi$	C
Straight pipe	-	2
90° bend (R/d = 4.0)	0.09	2.7
Sudden expansion of cross-section	1	1.21
Sudden contraction of cross-section	0.5	1.21

By adding the frictional pressure loss, the sum of the pressure losses in the components and the gravitational term, the pressure difference across the downcomer is obtained as shown in equation 3.11.

$$\Delta p_{dc} = \Delta p_{dc;fr} + \sum \Delta p_{dc;c} - H \cdot \rho' \cdot g \quad (3.11)$$

Since the height difference across the liquid column is positive for the downcomer, the result of  $\Delta p_{dc}$  should be negative and thus lead to a pressure increase before the evaporator inlet. The pressure losses (minor and major), the gravity term and the lengths from Table 3.1 were implemented in the tube models.

The design of the plate heat exchanger model for the evaporator is based on the geometry of the prototype provided by Alfa Laval. More precisely, one half of the two-stage evaporator, as only the geometry of the gravity-fed evaporator is initially considered. The geometry was determined by measurement wherever possible and supplemented by reasonable assumptions from the literature. The values determined and other values for the initialization of the evaporator are listed in Table 3.3. For modeling the heat transfer that occurs inside of the evaporator, heat transfer correlations are included in the models. The heat transfer of the evaporator is composed of the convective heat transfer of the two fluids and the heat conduction through the wall. A heat transfer model for convective heat transfer can be selected independently for each fluid side (in the case of the evaporator: CO<sub>2</sub> and water). The heat exchangers can be discretized into individual finite volume elements, called cells ( $n_{Cells}$ ) in the following. The discretization into  $n_{Cells}$  is done for both fluid sides and for the wall and allows, for example, to follow the temperature curve within the heat exchanger. The interconnection of the cells within the heat exchanger can be seen in Appendix B. The evaporator is discretized into 25 cells. The number of cells was increased stepwise (1; 2; 5; 10; ...; 25) until the relative change of the dissipated heat flux between two consecutive successive simulations was less

than 0.5 %. This is considered to be sufficiently accurate. Since no suitable correlation for the heat transfer is available in the literature for evaporators designed as plate heat exchangers with the refrigerant CO<sub>2</sub>, the correlation of Longo et al. is used. As this correlation was not created for CO<sub>2</sub>, the reference heat transfer coefficient  $\alpha_0$  (see Table 3.3) was taken from the heat transfer coefficient for the CO<sub>2</sub> side of evaporators from Smitt et al. [32]. For the heat transfer of the secondary fluid (water), the correlation VDI plate heat exchanger for single-phase fluid is used.

Table 3.3: Initialization values of the gravity-fed evaporator

	Designation	Value	Unit
Geometry	Total number of plates	40	-
	Plate length	0.42	m
	Plate width	0.1555	m
	Chevron angle	22.5	°
	Wall thickness	0.5	mm
	Pattern amplitude	0.0029	m
	Pattern wave length	0.006	m
	Number of cells	$n_{Cells}$ 25	-
Heat transfer	Heat transfer model CO <sub>2</sub>	Longo correlation	
	Reference heat transfer coefficient CO <sub>2</sub>	$\alpha_0$ 2500	W/(m <sup>2</sup> · K)
	Heat transfer model secondary fluid	VDI plate HX correlation	
	Wall material	Stainless Steel	
	Wall heat conduction Model	Geometry based	
Pressure drop	Pressure loss model CO <sub>2</sub>	Quadratic mass flow dependent $\Delta p$	
	Nominal pressure loss CO <sub>2</sub>	$\Delta p_n$ 2528	Pa
	Nominal mass flow CO <sub>2</sub>	$\dot{m}_n$ 0.0505	kg/s
	Nominal Plate length	$l_n$ 0.42	m
	Pressure drop secondary fluid	0	Pa

For the pressure loss, the correlation of the quadratic mass flow dependent pressure drop (equation 3.12), which is also already included in the model of the HX, was chosen. It contains the major and minor losses that occur in the HX. The correlation was adapted from the first measurements of the test rig by means of nominal values (see Table 3.3) which flow into the constant  $b$  (Eq. 3.13).

$$\Delta p_{ev;fr} + \sum \Delta p_{ev;c} = b \cdot \dot{m}^2 \quad (3.12)$$

$$b = \frac{\Delta p_n \cdot l}{\dot{m}_n^2 \cdot l_n} \quad (3.13)$$

If the gravity term is then integrated into the pressure loss calculation of the heat exchanger, the total pressure loss for the bottom-fed evaporator is obtained in equation 3.14. The implementation of the gravitational term into the HX was done by adding it to the existing correlation and dividing it by the number of cells ( $n_{Cells}$ ). This was done to account for the influence of the vertical flow direction of the refrigerant in the plate heat exchanger. Since the gravitational force acts against the

flow direction over the height  $h$  of the HX, the gravitational term becomes negative.

$$\Delta p_{ev} = \Delta p_{ev;fr} + \sum \Delta p_{ev;c} - h \cdot \rho_{ev} \cdot g \quad (3.14)$$

When the refrigerant leaves the evaporator, it has changed to a two-phase fluid for which the pressure drop is higher than for single-phase. Therefore, the single-phase pressure drop from the 3.9 and 3.10 equations must each be multiplied by the two-phase multiplier  $\beta$ . Beta is composed as described in equation 3.15, where the liquid only/vapour only pressure drop ratio  $\vartheta$  (equation 3.16) must first be calculated. The coefficient  $C$  for the different components can be found in Table 3.2. When calculating  $\beta$ ,  $x$  represents the vapor fraction of the refrigerant. [30]

$$\beta = [\vartheta + C(1 - \vartheta) \cdot x] \cdot (1 - x)^{0.333} + x^{2.276} \quad (3.15)$$

$$\vartheta = \frac{\rho''}{\rho'} \cdot \left( \frac{\mu'}{\mu''} \right)^{0.25} \quad (3.16)$$

If  $\beta$  is now inserted into the single-phase pressure loss equations as described, the equations 3.17 and 3.18 are obtained which apply to the riser.[29]

$$\Delta p_{rs;fr} = \frac{0.3164}{2} \cdot \beta_{rs} \cdot \frac{\mu''^{0.25}}{\rho} \cdot \dot{m}^{1.75} \cdot \frac{l_{rs}}{d_i^{4.75}} \quad (3.17)$$

$$\Delta p_{rs;c} = \zeta \cdot \frac{\dot{G}^2}{2 \cdot \rho''} \cdot \beta \quad (3.18)$$

As with the downcomer, all pressure losses across the riser are now added together as shown in equation 3.19. Since the gravitational force with the height  $H_0$  acts against the flow direction, the gravitational term becomes negative, and the pressure difference becomes positive.

$$\Delta p_{rs;c} = \Delta p_{rs;fr} + \sum \Delta p_{rs;c} - H_0 \cdot \rho_0 \cdot g \quad (3.19)$$

For the gravity-fed loop to operate in the simulation model, the direction of flow of the refrigerant had to be restricted in one direction. This could be achieved by using an *Inline Boundary* and a *PI controller*. The PI controller controlled the mass flow by matching the actual value (pressure before the *Inline Boundary*) with the setpoint value (pressure after the *Inline Boundary*). The controller settings can be found in Appendix C. The secondary fluid side (water) in the gravity loop was modeled in a simplified way with two *Fluid Boundaries*, where e.g. the temperature, pressure and mass flow can be specified.

## The refrigeration cycle with the gravity-fed evaporator loop

After the gravity-fed evaporator loop has been created, the remaining components must be added to create a closed refrigeration cycle. For this purpose, the remaining three HX are inserted and initialized. These include the internal heat exchanger and the two gas coolers. For these, the brazed plate heat exchangers AXP14 from Alfa Laval available on the market are used. The geometry was taken as far as possible from the manufacturer's data and supplemented by reasonable assumptions

from the literature. For the IHX, the smallest available design with 10 plates, and for the two GCs, the largest possible design with 150 plates was chosen. [1] The heat transfer for the IHX was initialized on the low pressure side (LP) equivalent to the evaporator. On the high pressure (HP) side, a constant alpha value of  $2521.1 \text{ W m}^{-2} \text{ K}^{-1}$  from Zendehboudi et al. [39] was assumed for the heat transfer model. For the  $\text{CO}_2$  side of the gas coolers 1 and 2 the heat transfer model was also realized with constant alpha values, which are the same for both fluids. For the GC 1 a value of  $977.8 \text{ W m}^{-2} \text{ K}^{-1}$  and for the GC 2 of  $1870.5 \text{ W m}^{-2} \text{ K}^{-1}$  was assumed from Zendehboudi et al. [39]. In all three HX, a simplified assumption was made that no pressure loss occurs. An PI controller controls the water mass flow entering the two gas coolers so that the  $\text{CO}_2$  exits at a 3 K higher temperature than the water inlet temperature. The values of the initialization of the HX are summarized in Table 3.4. The *EffCompressor* class is used for the compressor. It is parameterized with via the displacement volume of 0.0161 as well as parameters that represent losses. By these losses the model can represent the deviation of the considered compression to an ideal isentropic compression. These include the volumetric efficiency and the isentropic efficiency. Volumetric efficiency can be used to represent the deviation of the transported mass flow from the theoretically possible transported mass flow. For the theoretical mass flow rate transported, the compressor volume, the speed and the density of the refrigerant upstream of the compressor inlet must be taken into account. The isentropic efficiency is formed from the ratio of the adiabatically reversible technical work in relation to the specific technical work to be applied in reality. Furthermore, it is assumed that the compressors do not exchange heat with the environment (adiabatic compression). For more detailed information on the efficiency-based approach of the model, please refer to Försterling [15]. Both volumetric efficiency and isentropic efficiency depend, among other things, on the pressure ratio. Since these change under the boundary conditions considered in this work, a value of 0.7 was chosen for both. [7] Via the speed control of the compressor, the suction pressure is controlled. This is done with the aid of a *PI controller*. The PI controller regulates the speed of the compressor by comparing the actual value (pressure before the compressor) with the setpoint. The settings of the controller can be found in Appendix C.



Table 3.4: Initialization values of the internal heat exchanger and the gas coolers.

	Designation	Value	Unit
Geometry	Total number of plates IHX	10	-
	Total number of plates gas cooler	150	-
	Plate length	0.154	m
	Plate width	0.076	m
	Chevron angle	22.5	deg
	Wall thickness	0.5	mm
	Pattern amplitude	0.0029	m
	Pattern wave length	0.006	m
	Number of cells	$n_{Cells}$ 25	-
Heat transfer IHX	Heat transfer model low pressure	Longo correlation	
	Reference heat transfer coefficient LP	$\alpha_0$ 2500	W/(m <sup>2</sup> · K)
	Heat transfer model high pressure	Constant alpha	
	Heat transfer coefficient HP	2521.1	W/(m <sup>2</sup> · K)
	Wall material	Stainless Steel	
	Wall heat conduction Model	Geometry based	
Heat transfer GC	Heat transfer model CO <sub>2</sub> and water	Constant alpha	
	Heat transfer coefficient GC 1	977.8	W/(m <sup>2</sup> · K)
	Heat transfer coefficient GC 2	1870.5	W/(m <sup>2</sup> · K)
	Wall material	Stainless Steel	
	Wall heat conduction Model	Geometry based	

For the high pressure control valve an *orifice valve* from the TIL library was selected. In the valve model, the mass flow is calculated using the Bernoulli equation. A PI controller is used to control the effective flow area of the valve and thus the pressure upstream of it. The controller compares the actual value (pressure in front of the valve) with the set value of 120 bar. The settings of the controller can be found in Appendix C.

## 3.2 Model based examinations

After the model design of the gravity-fed evaporator system has been completed, this subsection first examines the system under design conditions. This is followed by a validation of the model with the aid of measurement data from the laboratory test rig. After validation, the simulation results for different operating conditions and different gravity-loop component dimensions are presented.

### Design conditions for the gravity-fed evaporator system

The design conditions for the simulation model were chosen so that a vapor fraction of 75 % to 85 % is present at the evaporator outlet. At the same time, it should be possible to provide the boundary conditions for the evaporator such as water mass flow, water outlet temperature and evaporation pressure from the test rig in order to validate the results. As design conditions for the gas cooler side, the project of Gabriellii [16] already presented in chapter 2.4 was used. In this project, water should be heated from 24 °C to about 90 °C using a heat pump chiller. The design conditions are shown in Table 3.5.

Table 3.5: Design conditions for the gravity-fed evaporator system

	Designation	Value	Unit
Gravity-fed evaporator	Separator pressure	41	[bar]
	Cooling capacity	8.185	[kW]
	Refrigeration mass flow gravity loop	2.980	[kg/min]
	Vapor fraction evaporator outlet	78.24	[%]
	Water inlet temperature	12	[°C]
	Water outlet temperature	7.12	[°C]
	Water mass flow	24	[kg/min]
Gas cooler	High pressure	120	[bar]
	Heating capacity	11.149	[kW]
	Refrigeration mass flow GC	2.618	[kg/min]
	Refrigeration outlet temperature GC	27	[°C]
	Water inlet temperatur	24	[°C]
	Water outlet temperatur	92.7	[°C]
	Water mass flow	2.326	[kg/min]

From the table it can be seen that the refrigerant leaves the evaporator with a vapor fraction of 78.24 % and thus meets the target conditions. The cooling capacity of the evaporator is approximately 8.2 kW and cools the water by about 5 K. On the heat sink side, the water is simultaneously heated by about 69 K to 92.7 °C with a thermal power of about 11.1 kW. The state points that occur under design conditions are illustrated in Figure 3.3 in a p,h diagram. In part a) of the figure, the overall process of the gravity-fed evaporator system is shown. Since the thermodynamic state changes within the gravity-fed evaporator loop occur only with small pressure differences, a zoomed in p,h diagram is shown separately in b). Between point 1 and 2, the refrigerant leaving the separator

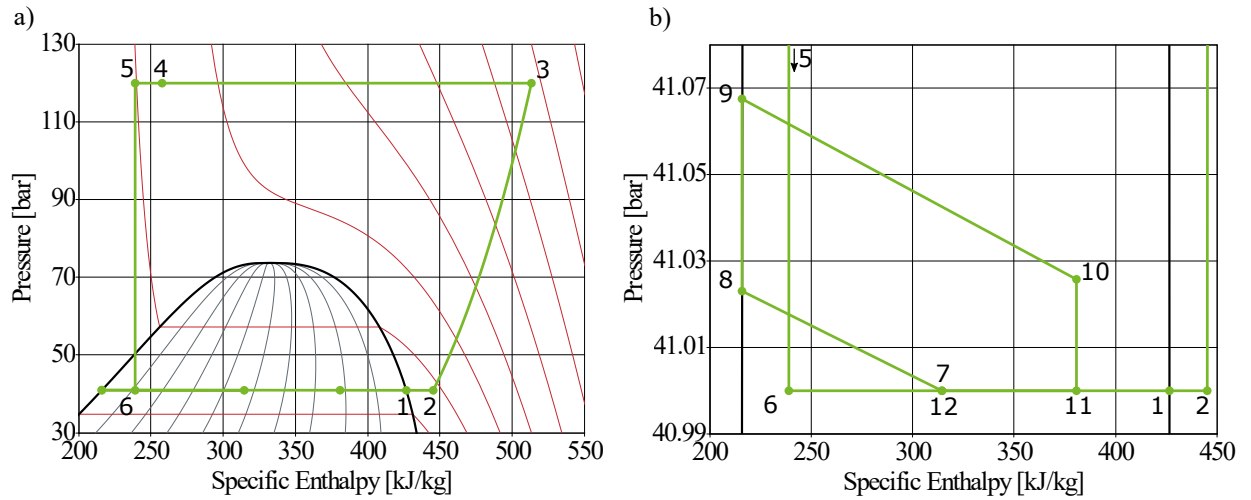


Figure 3.3: Illustration of the state points (from Figure 3.1) under design conditions of a) the entire gravity-fed evaporator system in the p,h diagram and b) zoomed in on the state points of the gravity-fed evaporator loop)

is superheated from the saturation line with the help of the IHX. Then, from 2 to 3, the refrigerant is compressed and heats up in the process. From 3 to 4, the refrigerant is cooled down with the help of the two GCs. Subsequently, the transcritical refrigerant in the IHX is cooled down further from 4 to 5. From 5 to 6, it is expanded into the separator. Now the process is continued in Figure 3.3 b) for better illustration. From 6 to 7, the expanded refrigerant is mixed with the refrigerant that returns from the gravity loop and then enters the separator. The liquid part of the refrigerant exits the separator in 8 under the influence of the static pressure of the liquid column. This causes the pressure to increase by approximately 2000 Pa. From 8 to 9, mainly the static pressure of the refrigerant in the downcomer acts on point 9, so that the pressure before the evaporator inlet increases by another 5000 Pa. A pressure drop of about 4000 Pa, as well as the vaporization inside the plate heat exchanger can be seen between 9 and 10. In the riser, a further pressure drop of about 3000 Pa occurs from 10 to 11. Subsequently, the two-phase refrigerant is mixed together with the expanded refrigerant from 6, to 12 and enters the separator. The gaseous phase is then sucked back towards the compressor 1.

### Model validation of the gravity-fed evaporator system based on measurement data

Ideally, a simulation model of a thermal system should represent the reality, which means that it should take into account all physical and chemical processes that occur in the real process. In this way, the behavior of the modeled system can be investigated without high costs and optimization potentials can be identified, for example. When building such a simulation model, a step-by-step approach is taken and assumptions or simplifications often have to be made, as can be seen from Chapter 3.1. In order to check whether the finished simulation model shows a reasonable behavior despite these assumptions, a validity analysis is carried out in the following. This is based on

measurements from the NTNU/SINTEF laboratory where the gravity-fed evaporator loop was experimentally investigated and which was the basis for the model design described in Chapter 3.1. The evaluation of the measurement results from the test rig is described in Hafsås [22].

Table 3.6 compares the measured values from the test rig with the results from the simulation for the design point. If the values are now compared with each other, the large deviation between the two refrigerant mass flows of almost 37 % is particularly noticeable. Furthermore, the vapor fraction with  $-29\%$  also differ significantly. The cooling capacity as well as the water outlet temperature differ with approximate 4 % and about 3 %, respectively, do not differ much. All other values vary negligibly. In order to approximate the simulation results to the measured values, deviations between the simulation model and the test rig must be identified. Since the mass flow and thus also the vapor fraction deviate strongly, the reasons for this had to be investigated. As already described in chapter 3.1, the mass flow in gravity-fed systems depends on the thermosyphon effect. This depends strongly on the pressure losses within the loop. Thus, the higher the pressure drop, the lower the mass flow in the gravity loop. The coriolis mass flow sensor was identified as the first cause of a higher pressure drop in the test rig. In addition, there are shut-off handles, a sight glass and several sensors in the loop.

Table 3.6: Measured values compared with the simulated values for the gravity-fed evaporator in the design point

Designation	Measured value	Simulated value	Unit	Difference [%]
Separator pressure	41	41	[bar]	0
Cooling capacity	7.9	8.185	[kW]	3.5
Refrigeration mass flow gravity loop	1.9	2.980	[kg/min]	36.2
Vapor fraction evaporator outlet	100.9	78.24	[%]	$-29.0$
Water inlet temperature	12	12	[°C]	0
Water outlet temperature	7.3	7.12	[°C]	$-2.5$
Water mass flow	24	24	[kg/min]	0

From the manufacturer's documentation of the *Rheonics coreolis mass flow sensor RHM 06*, a pressure drop curve per mass flow could be obtained (see Appendix D). The pressure drop curve is shown for the fluid water from  $0 \text{ kg min}^{-1}$  to  $36 \text{ kg min}^{-1}$ . Due to the fact that the  $\text{CO}_2$  mass flow in the gravity-loop will not increase above  $6 \text{ kg min}^{-1}$ , a correlation for the pressure loss curve was created covering the mass flow from  $0 \text{ kg min}^{-1}$  to  $6 \text{ kg min}^{-1}$ . This can be seen in equation 3.20. Since the viscosity and density of water and liquid  $\text{CO}_2$  differ significantly, pressure losses are expected to be lower with  $\text{CO}_2$ . Therefore, a correction factor was taken into account when implementing the equation in the model.

$$\Delta p_{MFM} = 6 \cdot 10^{10} x^6 - 2 \cdot 10^{10} x^5 + 3 \cdot 10^9 x^4 - 2 \cdot 10^8 x^3 + 5 \cdot 10^6 x^2 + 191555 \cdot x - 64.245 \quad (3.20)$$

By iteratively adjusting the correction factor to 0.28, the deviations of the simulation results could be reduced. This is especially true for the mass flow and the vapor content. The refrigerant mass

flow rate is now  $2.27 \text{ kg min}^{-1}$ , deviating by 17%. The refrigerant is now saturated with 100% vapor fraction, deviating by 6%. Furthermore, the refrigeration capacity of the model at the design point has also moved closer to the measured value at 7.97 kW. It should be noted that the implementation of the pressure loss correlation with correction factor not only applies to the mass flow sensor, but also takes into account all pressure losses not considered in the gravity loop model. The approximation of the model at the design point is considered sufficiently accurate at this point. Therefore, the model can now be validated under different boundary conditions.

For this purpose, 21 operation points measured on the test rig were chosen in order to compare the simulation and measurement results. The results can be seen in Figure 3.4. The two diagrams show the deviations between the experimentally determined cooling capacity (X-axis) and the cooling capacity determined in the simulation (Y-axis). Figure 3.4 a) shows the comparison of different operating points at a separator pressure of 38 bar. Different cooling capacities were generated by varying the water mass flow rate between  $12 \text{ kg min}^{-1}$  and  $24 \text{ kg min}^{-1}$  and the water inlet temperature between  $10^\circ\text{C}$  and  $15^\circ\text{C}$ . The comparison of the measured and simulated values does not show a very large deviation, especially up to a cooling capacity of 10 kW. For higher capacities, the values deviate more strongly from each other. However, except for one value, all values remain within a deviation of  $\pm 15\%$ . Figure 3.4 b) compares 10 different operating points at three different separator pressures. The different cooling capacities were generated with four different water inlet temperatures between  $10^\circ\text{C}$  and  $20^\circ\text{C}$  and at a water mass flow rate of  $16 \text{ kg min}^{-1}$ . Here the differences between simulative and experimental results are very close up to a cooling capacity of about 9 kW. For larger loads, the differences also become more significant. As in part a) of the figure, the measured values are larger than the simulated ones, but remain within  $\pm 15\%$ .

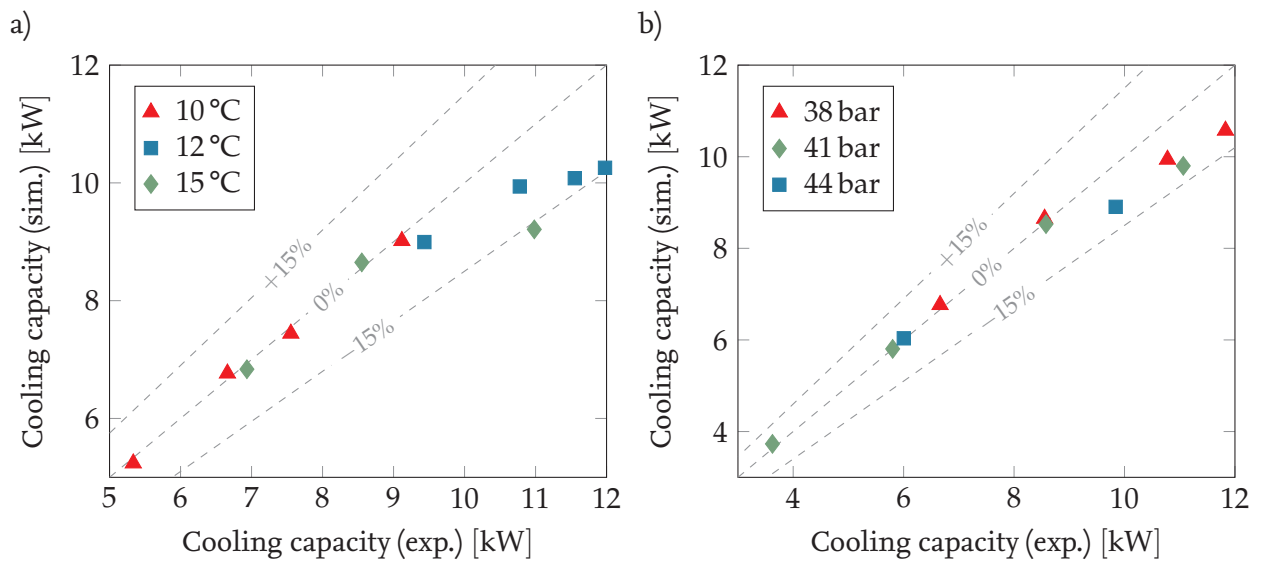


Figure 3.4: Validation of the gravity loop for a) 11 different operating points at 38 bar separator pressure and b) for 10 different operating points at three different separator pressures.

When comparing all recorded values, it is noticeable that the operating points which show larger deviation from each other all exit the evaporator superheated. Therefore, it is obvious that either the Longo correlation used for the heat transfer in case of superheating is no longer applicable, or that the pressure loss calculations do not reflect the reality of superheated refrigerants properly. A combination of both would also be possible. Under normal circumstances, the gravity-fed evaporator should be operated without superheating in any case. Since this case is represented very well by the simulation model, the simulation model is assumed to be sufficiently valid at this point.

### Steady-state investigation of the gravity-fed evaporator loop dimensions

In this subsection, the influence of the dimensioning of the gravity-fed evaporator loop is investigated. This is essential to understand the influence of the individual components on the performance of the loop. This steady-state examination is carried out without the additional pressure drop required for validation. The reason for this is that, outside of test rigs, real systems are not equipped with a mass flow sensor inside the gravity loop.

Therefore, the influence of the static height  $H$ , i.e. the height of the downcomer plus the height of the liquid level in the separator, on the performance of the gravity-fed evaporator loop is investigated first. For this purpose, the static height was varied between 0.35 m and 1.43 m at a separator pressure of 41 bar, a water inlet temperature of 12 °C, and a water mass flow rate of 24 kg min<sup>-1</sup>. This is illustrated in Figure 3.5 and Figure 3.6. It can be seen that the refrigerant mass flow through the evaporator depends strongly on the static height. At low heights, very little refrigerant circulates in the gravity loop due to the thermosyphon effect. This leads to superheating in the HX. The superheating results in poorer heat transfer because less fluid is in contact with the HX surface. Therefore, low height results in a low cooling capacity of less than 8 kW.

The highest cooling capacity occurs with about 8.3 kW at a vapor fraction between 70 % and 90 %. A vapor fraction of 80 % can thus be considered optimal for the design of the gravity loop. With increasing height the vapor fraction decreases. At the same time, the cooling capacity also decreases slightly. Another very interesting aspect is the comparison between the refrigerant mass flow in the gravity loop and that in the gas cooler. While the refrigerant mass flow through the gas cooler remains almost constant, the refrigerant mass flow in the evaporator increases significantly with increasing height. At low vapor fraction, the refrigerant must pass through the gravity loop up to two times (at 1.43 m) until it is completely evaporated. Figure 3.6 further shows the pressure difference across the three components of the gravity loop (downcomer, evaporator, and riser). The pressure difference in the downcomer represents an increase in pressure (+), while the pressure differences in the evaporator and riser represent losses (-). Adding the two losses gives the pressure rise across the downcomer.

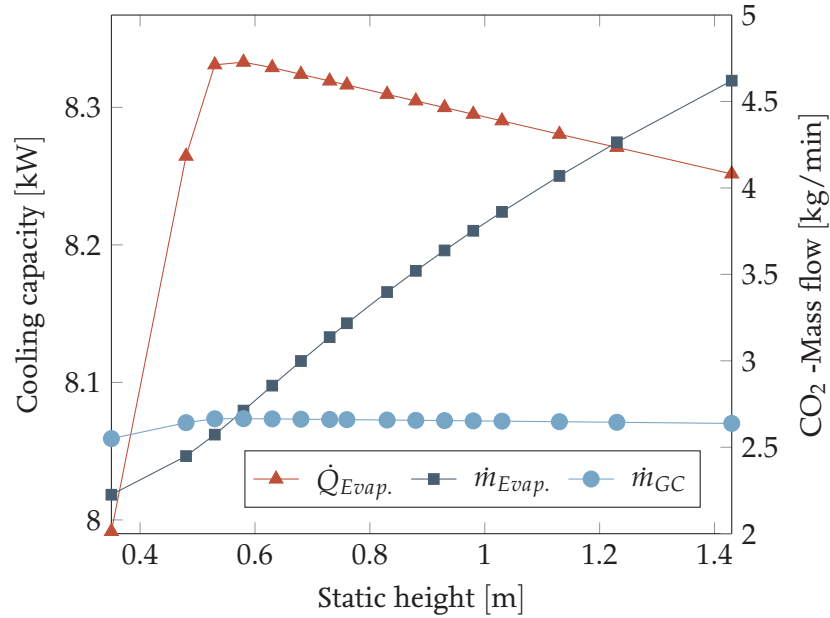


Figure 3.5: Influence of the static height on the cooling capacity and the refrigerant mass flow in the gravity loop and via the gas cooler (separator pressure: 41 bar, water inlet temperature: 12 °C, water mass flow: 24 kg min<sup>-1</sup>).

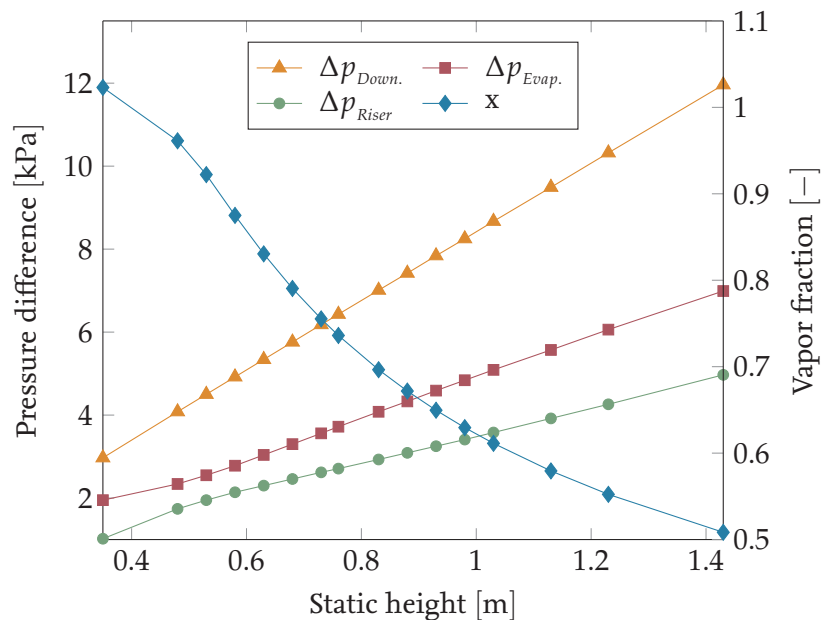


Figure 3.6: Influence of the static height on the pressure difference in the downcomer  $\Delta p_{Down.}$ , evaporator  $\Delta p_{Evap.}$  and riser  $\Delta p_{Riser}$  as well as on the refrigerant vapor fraction  $x$  at the outlet of the evaporator (separator pressure: 41 bar, water inlet temperature: 12 °C, water mass flow: 24 kg min<sup>-1</sup>).

Another important component in the gravity-fed evaporator loop is the riser. Since the riser, unlike the downcomer, contains two-phase fluid, the expected pressure loss in it is bigger than in the downcomer. Although the pressure drop in the HX is higher than in the riser, as can be seen in

Figure 3.3, it is much more difficult to reduce. Therefore, the influence of the variation of the riser diameter was investigated in Figure 3.7. During the study, the diameter was varied between 14 mm and 28 mm. The boundary conditions were selected in the same way as for the downcomer variation.

As the diameter increases, the pressure drop in the riser decreases. At the same time, however, the pressure drop in the evaporator increases. This is due to the fact that the mass flow of the self-circulating circuit increases because of the lower pressure drop. The increase in pressure drop across the evaporator is not as high as the decrease across the riser. With higher mass flow, the vapor fraction at the outlet of the evaporator also decreases by up to 14 % compared to a diameter of 14 mm. From about 20 mm diameter, the initially strong effect decreases. Hence, it can be concluded that an expansion of the diameter by more than twice the downcomer diameter has no significant additional value.

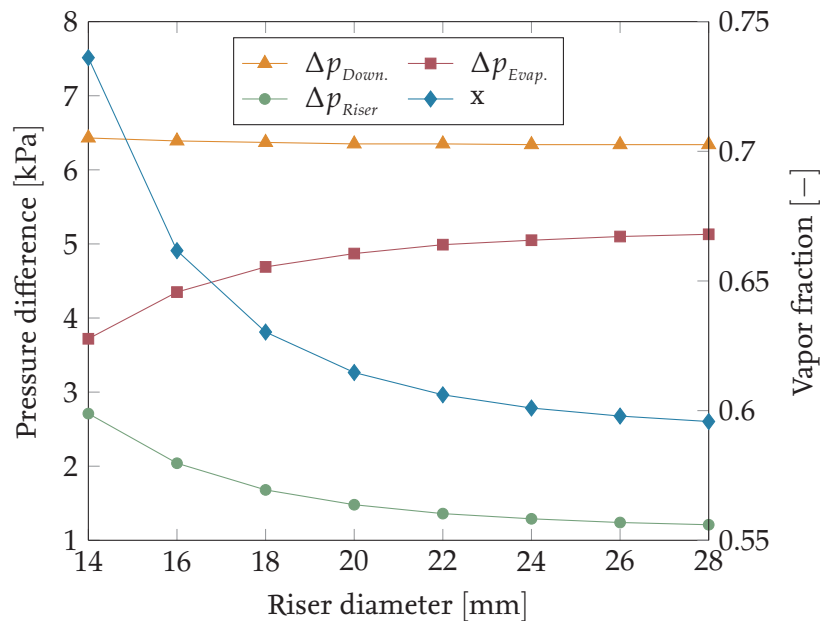


Figure 3.7: Influence of the riser diameter on the pressure difference in the downcomer  $\Delta p_{Down.}$ , evaporator  $\Delta p_{Evap.}$  and riser  $\Delta p_{Riser}$  as well as on the refrigerant vapor fraction  $x$  at the outlet of the evaporator (separator pressure: 41 bar, water inlet temperature: 12 °C, water mass flow: 24 kg min<sup>-1</sup>).

In conclusion, it can be said that by choosing a larger riser diameter, similar effects occur as with the choice of a higher downcomer. Thus, the static height can be reduced by increasing the riser diameter. In this case, however, this applies only up to twice the diameter. The reduction of the vapor fraction by approximately 15 % can therefore be achieved for the operating point investigated either with a doubling of the riser diameter or with an increase in the static height by approximately 0.3 m. Further investigations are required to determine the extent to which this conclusion can be applied to other operating points and gravity loop dimensions.



## Steady-state investigation of the influence of various boundary conditions on the gravity-fed evaporator loop

In the following subsection, the influence of various boundary conditions on the gravity-fed evaporator loop is investigated. These include investigations on the influence of different water inlet temperatures and water mass flows on the evaporator loop.

First, the influence of different water inlet temperatures are considered. For this purpose, the water inlet temperature was varied from 10 °C to 20 °C. The results are shown in Figures 3.8, 3.9 and 3.10. If the inlet temperature of the water increases, the cooling capacity via the evaporator also increases. This is shown in Figure 3.8 and 3.10.

At the same time, the refrigerant mass flow in the gravity loop decreases up to a temperature of 13.5 °C and then increases again to the original value of about 3.3 kg min<sup>-1</sup>. As can be seen in Figure 3.9, this is due to the fact that, with increasing water inlet temperature, the vapor fraction and thus the pressure drop in the riser increases. Thus, the self circulating mass flow decreases due to the increased pressure drop in the riser until a vapor fraction of 0.95 is reached. While the pressure drop in the riser increases, the pressure drop in the evaporator decreases as the refrigerant mass flow decreases. This is because the pressure drop in the evaporator model is calculated quadratic mass flow dependent (see equation 3.12).

Figure 3.10 again shows the cooling capacity over the water inlet temperature. This time, however, together with the temperature difference of the secondary fluid  $\Delta T_w$  over the evaporator and with the temperature difference between the refrigerant and the water entering the evaporator  $\Delta T_{in}$ . If the inlet water temperature increases, the cooling capacity via the evaporator also increases almost linearly up to a water inlet temperature of 14 °C. After that, the curve flattens out until it hardly increases from 18 °C. A similar curve can also be observed for the temperature difference of the water  $\Delta T_w$  between inlet and outlet. In the investigated section, the maximum temperature difference in the evaporator  $\Delta T_{in}$  increases linearly. With the given boundary conditions and dimensions of the gravity-fed evaporator loop, a maximum  $\Delta T_w$  of about 7.75 K and a cooling capacity of maximum 13 kW can be obtained.

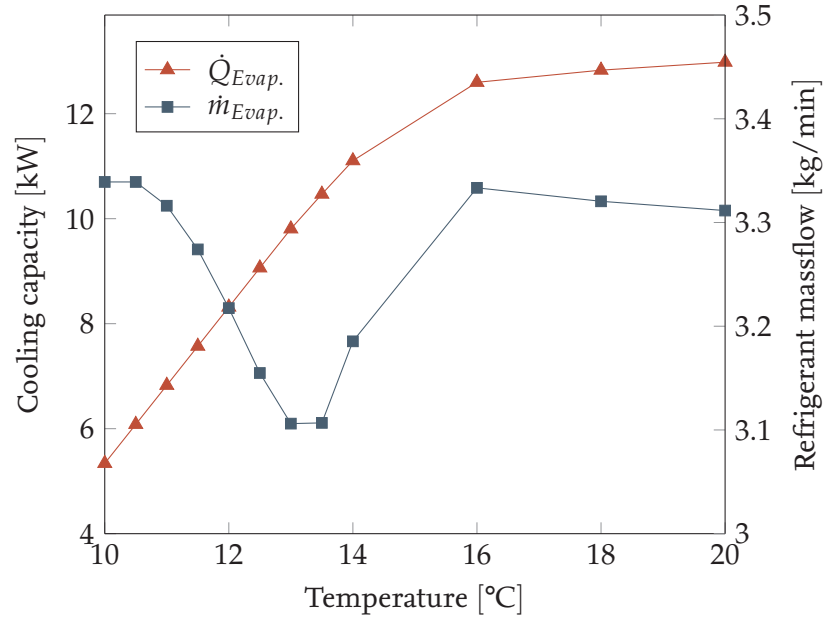


Figure 3.8: Investigation of the influence of different water inlet temperatures on the gravity-fed evaporator loop with respect to the cooling capacity  $\dot{Q}_{Evap.}$  and the refrigerant mass flow over the gravity-fed evaporator loop  $\dot{m}_{Evap.}$  (separator pressure: 41 bar, water mass flow:  $24 \text{ kg min}^{-1}$ ).

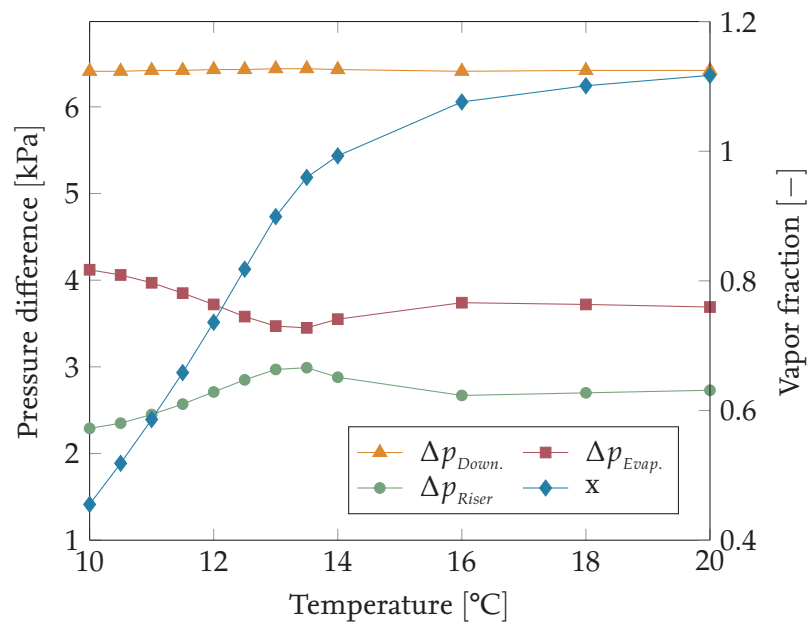


Figure 3.9: Investigation of the influence of different water inlet temperatures on the gravity-fed evaporator loop with respect to the pressure differences in the downcomer  $\Delta p_{Down.}$ , evaporator  $\Delta p_{Evap.}$  and riser  $\Delta p_{Riser}$ , as well as on the refrigerant vapor fraction  $x$  at the outlet of the evaporator (separator pressure: 41 bar, water mass flow:  $24 \text{ kg min}^{-1}$ ).

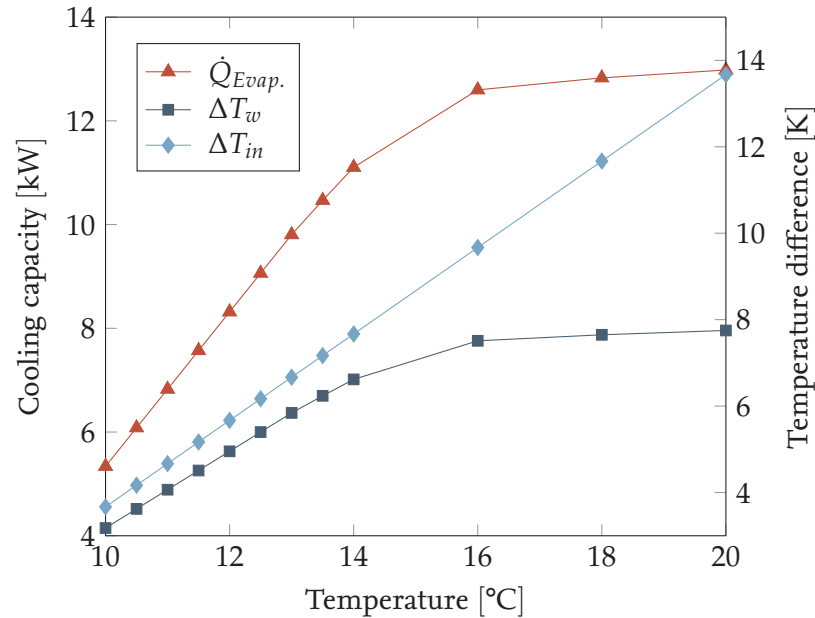


Figure 3.10: Investigation of the influence of different water inlet temperatures on the gravity-fed evaporator loop with respect to the cooling capacity  $\dot{Q}_{Evap.}$ , the water temperature differences between inlet and outlet of the evaporator  $\Delta T_w$  and the temperature difference between the refrigerant and the water entering the evaporator  $\Delta T_{in}$  (separator pressure: 41 bar, water mass flow:  $24 \text{ kg min}^{-1}$ ).

Next, the influence of different water mass flows on the gravity-fed evaporator loop is investigated. For this purpose, the water mass flow was varied from  $12 \text{ kg min}^{-1}$  to  $48 \text{ kg min}^{-1}$  while leaving the water inlet temperature constant at  $12 \text{ }^\circ\text{C}$  and the separator pressure at 41 bar. The results are illustrated in the Figures 3.11, 3.12 and 3.13. These results show a similar pattern as for the variation of the water inlet temperature. First, the course of the cooling capacity over the water mass flow is considered. This is shown in both Figure 3.11 and Figure 3.13. As the water mass flow increases, the cooling capacity increases almost linearly up to a mass flow of  $30 \text{ kg min}^{-1}$ . At the same time, the refrigerant mass flow in the gravity loop decreases up to a water mass flow of  $30 \text{ kg min}^{-1}$ . Subsequently, the refrigerant mass flow rate increases again to  $3.35 \text{ kg min}^{-1}$ , which was already the case at a water mass flow rate of  $15 \text{ kg min}^{-1}$ . As with the variation of the water inlet temperature, this is due to the fact that the vapor fraction and thus the pressure drop in the riser increases with increasing water mass flow. This can be seen in Figure 3.12. Thus, the self-circulating mass flow decreases due to the increased pressure drop in the riser until a vapor fraction of 0.95 is reached. While the pressure drop in the riser increases, the pressure drop in the evaporator decreases as the refrigerant mass flow decreases. This is because the pressure drop in the evaporator model is calculated quadratic mass flow dependent (see equation 3.12).

In Figure 3.13 again shows the cooling capacity over the water mass flow. This time, however, together with the temperature difference of the secondary fluid  $\Delta T_w$  over the evaporator and with the temperature difference between refrigerant and water entering the evaporator  $\Delta T_{in}$ . The cooling capacity increases steeply up to a water mass flow of  $42 \text{ kg min}^{-1}$  and then levels off. As the water

mass flow increases, the water temperature difference across the evaporator decreases. From initial 5.4 K the difference decreases by almost 2 K at the maximum examined water mass flow to about 3.65 K. However, the maximum temperature difference across the evaporator remains constant at 6.7 K.

By varying the water inlet temperature and the water mass flow rate, the behavior of the gravity-fed evaporator loop could be studied under different boundary conditions. Both the change in the water inlet temperature and the change in the water mass flow rate lead to a change in the cooling capacity and thus to similar behavior. The only strong difference can be seen when comparing the temperature differences in Figure 3.10 and Figure 3.13. In Figure 3.10, it is shown that the geometry of the gravity-fed evaporator loop has an influence on the maximum temperature difference between water inlet and outlet, as the maximum refrigerant mass flow is limited by the thermosyphon effect which depends on the geometry. Thus, even by increasing the water temperature, no temperature difference greater than 7.5 K could be achieved. However, if the water mass flow is increased, the temperature difference of the water to be cooled decreases, as shown in Figure 3.13. One of the reasons for this is that the refrigerant mass flow to be circulated via the thermosyphon effect (see Figures 3.8 and 3.11) also has a limit value. Under the operating conditions considered, this is slightly more than  $3.3 \text{ kg min}^{-1}$ .

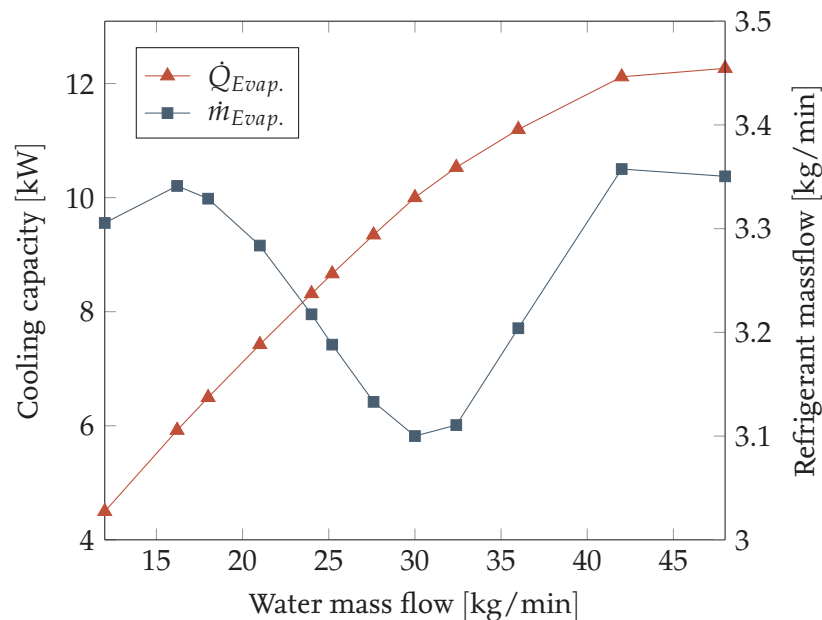


Figure 3.11: Investigation of the influence of different water mass flows on the gravity-fed evaporator loop with respect to the cooling capacity  $\dot{Q}_{Evap.}$  and the refrigerant mass flow over the gravity-fed evaporator loop  $\dot{m}_{Evap.}$  (separator pressure: 41 bar, water inlet temperature: 12 °C).

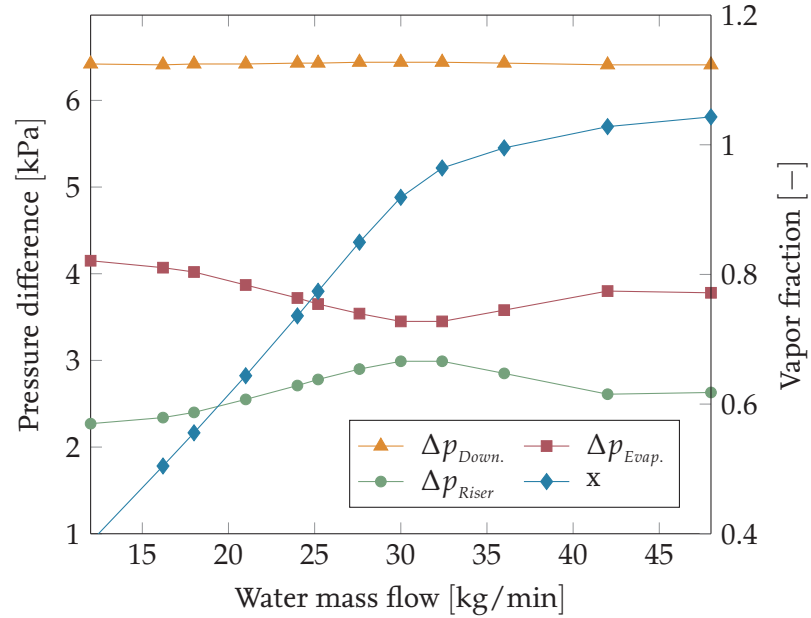


Figure 3.12: Investigation of the influence of different water mass flows on the gravity-fed evaporator loop with respect to the pressure differences in the downcomer  $\Delta p_{Down.}$ , evaporator  $\Delta p_{Evap.}$  and riser  $\Delta p_{Riser.}$  as well as on the refrigerant vapor fraction  $x$  at the outlet of the evaporator(separator pressure: 41 bar, water inlet temperature: 12 °C).

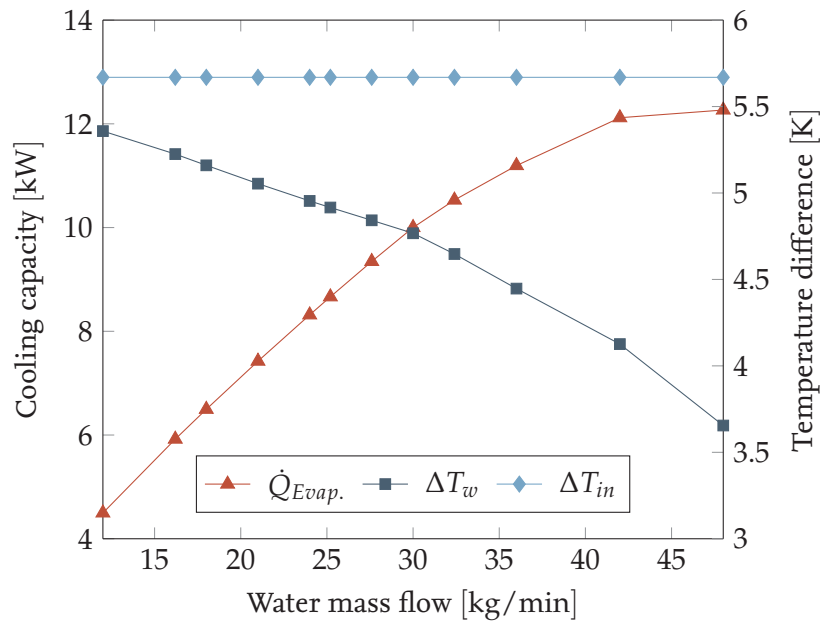


Figure 3.13: Investigation of the influence of different water mass flows on the gravity-fed evaporator loop with respect to the cooling capacity  $\dot{Q}_{Evap.}$ , the water temperature differences between inlet and outlet of the evaporator  $\Delta T_w$  and the temperature difference between refrigerant and water entering the evaporator  $\Delta T_{in}$  (separator pressure: 41 bar, water inlet temperature: 12 °C)

# 4 The heat pump chiller with novel two-stage evaporator

In this chapter, the gravity-fed evaporator system described in chapter 3 is extended to the full heat pump chiller system with the novel two-stage evaporator. For this purpose, some components have to be added or replaced in the existing model. Therefore, the first part of this chapter deals with the extension and parameterization of the model. Afterwards, the model is validated with measurement data from our test rig and checked for plausibility. This is followed by various tests using the simulation model.

## 4.1 Model design and parameterization

For the extension of the model a second evaporator and an ejector are needed. Furthermore, the position of the expansion valve must be changed and the displacement volume of the compressor must be adjusted. This is described step by step in this chapter. For all components that are not described and initialized in detail here, please refer to chapter 3. Figure 4.1 shows the final model with the changes just described. Please refer to chapter 2.5 for the description of the state changes that take place in the heat pump chiller.

The ejector-fed evaporator loop runs between state points 6, 7, 8, 13, 14 and 15 which can be followed in Figure 4.1. The structure between state-points 6 to 8 is as described in chapter 3. In the first part of the downcomer there is now not only the refrigerant for the gravity-fed evaporator loop present, but also the refrigerant that supplies the ejector-fed evaporator. After the downcomer's piping has become horizontal, the refrigerant mass flow is divided by means of a junction. With the help of the *orifice valve*, the refrigerant is expanded from point 13 to 14. In the design condition of the system, the valve is fixed at an effective flow area of  $1.95 \text{ mm}^2$ . This results in a pressure drop of about 4.3 bar over the valve. Subsequently, the refrigerant is evaporated from point 14 to 15. This is done with the same type and initialized heat exchanger as described in Table 3.3. Now, the only difference is that the refrigerant enters the evaporator from the top instead of the bottom. Unlike the gravity loop, the gravitational force acts with the direction of flow of the refrigerant in the plate heat exchanger. Thus the gravitational term for equation 3.14 becomes positive, meaning that the pressure increases across the liquid column of the height of the HX is taken into account. The refrigerant leaving the evaporator is the suction flow of the ejector. For this purpose, the class of the *Efficiency based ejector* was used. In this model, the effective area of the motive flow nozzle is determined by a PI controller. By changing the area of the effective flow area of the nozzle, the PI controller adjusts the high pressure to the setpoint of 120 bar. For the modeling of the nozzle flow, the correlation of Brennen [4] was used, which is suitable for two-phase  $\text{CO}_2$  flow and is al-

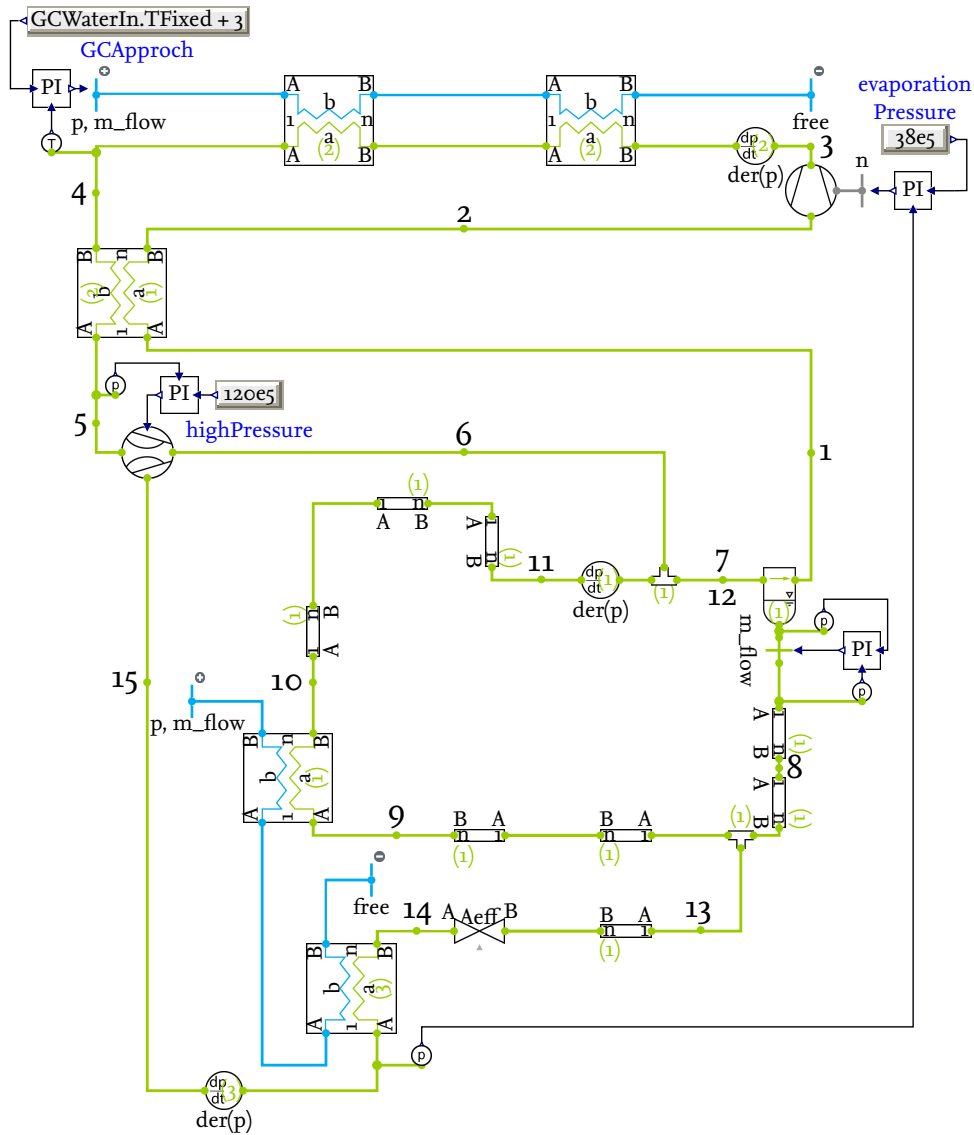


Figure 4.1: Schematic diagram of the heat pump chiller model with the two-stage evaporator in Dymola (Green lines: CO<sub>2</sub>, Light blue lines: water)

ready implemented in the class. In the ejector model, a fixed ejector efficiency can be specified. It is calculated as shown in equation 2.6 and was set to 20%. Although this efficiency is not as high as indicated in [9] with 30% to 35% for the design condition, it is assumed to be more realistic due to different operating conditions that are investigated.

Because of the two evaporators now installed in the model, the refrigeration capacity increases and thus the refrigerant mass flow rate. Therefore, the displacement volume of the compressor is no longer sufficient to deliver the required refrigerant mass flow. Therefore, this was increased to 0.0351. Furthermore, the control for the compressor was slightly adjusted. The actual pressure for the PI controller is now measured at the ejector-fed evaporator outlet. This was done on the basis of the test rig operation, where the ejector-fed evaporator was controlled to a fixed outlet pressure.

## 4.2 Model based examinations

After the model design of the heat pump chiller has been completed, it is examined under design conditions in a next step. Subsequently, the simulation model is validated with the measurement results. Then the design conditions are optimized on the basis of the experience gained and further investigations are carried out with the aid of the adapted simulation model.

### Design conditions for the heat pump chiller

The design of the two-stage evaporator circuit is based on the measurement results and the operation of the test rig, which is described in more detail in Hafsås [22]. This excludes the high pressure side. As mentioned above, this was designed to produce domestic hot water up to a temperature of 90 °C. Table 4.1 shows the design conditions.

Table 4.1: Design conditions for the heat pump chiller (Boundary conditions marked with \*)

	Designation	Value	Unit
Gravity-fed evaporator	Separator pressure	42.33	[bar]
	Cooling capacity	6.42	[kW]
	Refrigeration mass flow gravity loop	2.909	[kg/min]
	Vapor fraction evaporator outlet	64.12	[%]
	Water inlet temperature*	12	[°C]
	Water outlet temperature	8.18	[°C]
	Water mass flow*	24	[kg/min]
Ejector-fed evaporator	Evaporation pressure*	38	[bar]
	Cooling capacity	6.86	[kW]
	Refrigeration mass flow ejector loop	3.211	[kg/min]
	Vapor fraction evaporator outlet	62.93	[%]
	Water inlet temperature	8.18	[°C]
	Water outlet temperature	4.096	[°C]
	Water mass flow*	24	[kg/min]
Gas cooler	High pressure*	120	[bar]
	Heating capacity	17.9	[kW]
	Refrigeration mass flow GC	4.345	[kg/min]
	Refrigeration outlet temperature GC*	27	[°C]
	Water inlet temperatur*	24	[°C]
	Water outlet temperatur	88.53	[°C]
	Water mass flow	3.977	[kg/min]



In Table 4.1, the boundary conditions can be recognized by the fact that they are marked with an asterisk (\*). All other values are based on the initialization of the individual components and the thermodynamic processes they represent. The vapor fraction leaving both evaporators has a low value of about 64 % and 63 %, respectively. For the gravity-fed evaporator, this is due, among other things, to the higher pressure of the separator and the resulting higher evaporation temperature compared to the conditions in Table 3.5. In the gravity-fed evaporator, the water to be cooled is pre-cooled from 12 °C to 8.2 °C. It is then further cooled down to 4.1 °C in the ejector-fed evaporator. The cooling capacity is slightly more distributed on the ejector-fed evaporator with 6.86 kW to 6.42 kW at the gravity-fed evaporator. This also applies to the refrigerant distribution. On the heat sink side, the water is heated by about 64 K to 88.5 °C using a thermal power of about 17.9 kW.

In Figure 4.2, the state points occurring under design conditions are shown in a p,h diagram. Part a) of the figure, shows the overall process of the heat pump chiller. Since thermodynamic state changes within the gravity evaporator circuit only occur at small pressure differences, this is shown separately in b) with a different axis scaling. Between points 1 and 2, the saturated vapor leaving the separator is superheated by the IHX. From point 2 to 3, the refrigerant is then compressed and heats up. Thereafter, from 3 to 4, the refrigerant is cooled down with the help of the two GCs. Subsequently, the transcritical refrigerant is further cooled from 4 to 5 by the IHX. As the refrigerant exits the IHX (point 5), it enters the ejector as a motive flow and is expanded isentropically. At the same time, the refrigerant leaving the ejector-fed evaporator (point 15) is sucked in and compressed. Subsequently, both flows are mixed and exit the ejector as discharge flow in 6. Since the state changes within the ejector are not shown in the diagram, the lines between 5 and 6 and 15 and 6 are shown dashed. Ejector Discharge flow 6 and the refrigerant leaving the riser (point 11) are then mixed and enter the separator. In 8, the liquid refrigerant medium separated in the separator enters the downcomer, and the pressure increases due to the liquid column. From here on, the change of state in the gravity loop can be seen in detail in part b) of the figure. From 8 to 9, the pressure in the downcomer rises before the gravity-fed evaporator. A state change in the gravity-fed evaporator takes place from 9 (saturated or slightly subcooled liquid) to 10. Part of the refrigerant evaporates and enters the riser in 10 as a two-phase fluid. In the riser, the pressure loss leads to a change of state from 10 to 11. From point 8 the loop of the ejector-fed evaporator begins as well. In the first section of the downcomer, the pressure increases due to the hydrostatic pressure of the liquid column. While the refrigerant passing through the gravity loop flows towards point 9, part of the refrigerant flows through the junction to point 13. Afterwards, the refrigerant is expanded from 13 to 14 with the help of the throttle valve. Therefore, the subsequent evaporation from 14 to 15 takes place at a pressure about 4.3 bar lower than in the gravity-fed evaporator. From the ejector-fed evaporator, the refrigerant exits in two phases and is then sucked by the ejector and exits mixed with the expanded motive flow at point 6 at the separator pressure. Then the two-phase refrigerant mass flows 6 and 11 are mixed at point 12 and then enter the separator. Finally, the gaseous phase (point 1) is sucked out of the separator by the compressor.

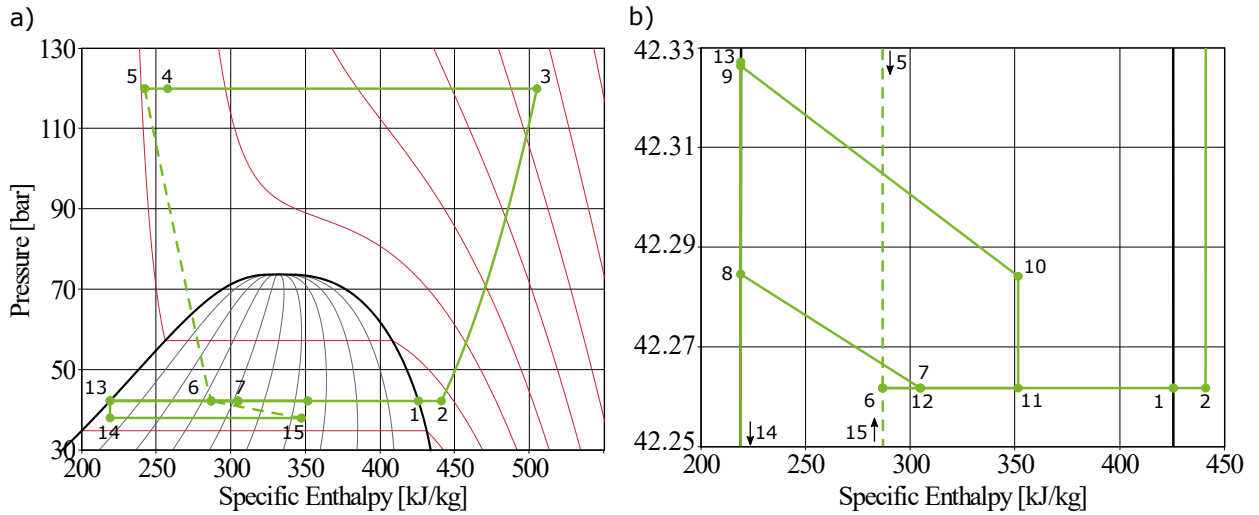


Figure 4.2: Illustration of the state points under design conditions of a) heat pump chiller in the p,h diagram and b) zoomed in on the state points of the gravity-fed evaporator loop)

## Model validation of the heat pump chiller system with the two-stage evaporators based on measurement data

As described in the validation of the gravity-fed evaporator system in Chapter 3, the simulation model created should be as close as possible to reality. However, since assumptions and simplifications had to be made when creating this model, the validation with the help of measurement data from the test rig is used to check the extent to which the model and reality match or divert from one another and subsequently take steps to bring them closer together. The validation of the gravity-fed evaporator loop has already shown that, among other things, the coriolis mass flow sensor entails a not inconsiderable pressure loss and this must therefore be taken into account in the validation of the simulation model. Since both gravity and ejector loop have the same mass flow sensor, the equation 3.20 is also used here and multiplied by the same correction factor of 0.28. In contrast to the design conditions, the validation was carried out at a high pressure of 80 bar, since the test rig could not provide the design pressure of 120 bar. As with the gravity-fed evaporator, validation is carried out only for the evaporator loops. Nevertheless, in the case of the two-stage evaporator system, the high pressure condition is important because it represents the motive conditions of the ejector. Therefore, as many boundary conditions of the ejector as possible were taken into account for the validation. This includes, for example, the motive and suction conditions as well as the efficiency of the ejector.

The results of the comparison of the measured values close to the design conditions with the simulated results are shown in Table 4.2. For better comparability, measured values were used for the setpoints of the PI controllers. These can be recognized from the table by the fact that they do not show any deviation. Although the gravity loop is identical to the validation in Chapter 3, a deviation of about 40% can be observed from Table 4.2 for the cooling capacity or vapor fraction. This deviation is mainly due to the higher separator pressure by 1.5 bar and thus by the same value higher evaporation pressure. Thus, the precooled water exits the gravity-fed evaporator with a

temperature 1 K higher in the simulation than in the measured value. If the ejector-fed evaporator is considered, the deviation for cooling capacity and vapor fraction is similar with about 40 % each. In addition, the water to be cooled emerges from the ejector-fed evaporator at 4.2 °C, which is a relative deviation of almost 23 % compared to the measurement at the test rig.

In order for the simulation results to be closer to the measured results, the separator pressure must be lowered. This was achieved by lowering the ejector efficiency to 5.5 %. This is admittedly a rather poor ejector efficiency, which can be attributed at least in part to the poor boundary conditions of the ejector. The results of the adjustment can be found in Appendix E. Thus, the largest deviation in the gravity loop could be lowered to 4.78 % for the cooling capacity. For the ejector-fed evaporator loop, the differences could also be reduced by lowering the ejector efficiency. The cooling capacity decreased by 1.8 kW to 6.8 kW, but still deviates by 23.6 % from the result of the test rig. After model fitting, refrigerant mass flow and evaporating pressure deviate only very slightly or not at all from the measured results. Since the evaporator models used have the same geometry, pressure loss and heat transfer model, this deviation needs to be further investigated .

Table 4.2: Measured values compared with the simulated values for the gravity-fed evaporator and the ejector-fed evaporator with similar boundary conditions

	Designation	Measured value	Simulated value	Unit	Difference %
Gravity-fed evaporator	Separator pressure	42.2	43.77	[bar]	3.59
	Cooling capacity	6.2	4.42	[kW]	-40.27
	Refrigeration mass flow	1.9	1.894	[kg/min]	-0.34
	Vapor fraction evaporator outlet	92.4	69.55	[%]	-32.85
	Water inlet temperature	12	12	[°C]	0
	Water outlet temperature	8.3	9.366	[°C]	11.38
	Water mass flow	24	24	[kg/min]	0
Ejector-fed evaporator	Evaporation pressure	38	38	[bar]	0
	Cooling capacity	5.2	8.619	[kW]	39.67
	Refrigeration mass flow	3.3	3.712	[kg/min]	11.38
	Vapor fraction evaporator outlet	42.5	69.73	[%]	39.05
	Water inlet temperature	8.3	9.366	[°C]	11.83
	Water outlet temperature	5.2	4.235	[°C]	-22.79
	Water mass flow	24	24	[kg/min]	0
Ejector	Motive flow pressure	79.8	79.8	[bar]	0
	Motive flow temperature	35	35	[°C]	0
	Ejector efficiency	10	10	[%]	0

A first approach to understand this difference is to examine under which conditions the simulation results match the experimental results. Since the simulated values for the cooling capacity deviated strongly from the measured results of the prototype, a poor heat transfer was considered as

a possible problem. Therefore, the correction factor for evaporation in the heat transfer model was adjusted iteratively until the cooling capacities matched. This was the case for the design condition at a correction factor of 0.2. This means that the average heat transfer coefficient obtained in the test rig for the ejector-fed evaporator is only 20 % of the value calculated by the Longo correlation. Consequently, the deviation between expected and present heat transfer coefficient turns out to be significant and needs further investigation. Due to the poor heat transfer coefficient, the temperature distribution curves within the evaporators also change. These are presented in Figure 4.3. It illustrates the temperature distribution curves for water and CO<sub>2</sub> in the gravity- and ejector-fed evaporator. While the green lines represent the temperature curves on the CO<sub>2</sub> side, the blue lines represent the temperature of water to be cooled. In addition, the solid lines show the simulation results in which both evaporators use the same heat transfer model (Longo correlation for the CO<sub>2</sub> side). Dashed lines represent the temperature curve when the heat transfer model in the ejector-fed evaporator is adjusted using the evaporation correction factor of 0.2 determined during validation. While the temperature curves in the gravity loop are still almost identical, the correction of the heat transfer model for the ejector loop leads to greater deviations on the water side. As a result, the water outlet temperature from the ejector-fed evaporator differs by approximately 1 K. Due to the same evaporation pressure, the temperature curves for the CO<sub>2</sub> side run congruent.

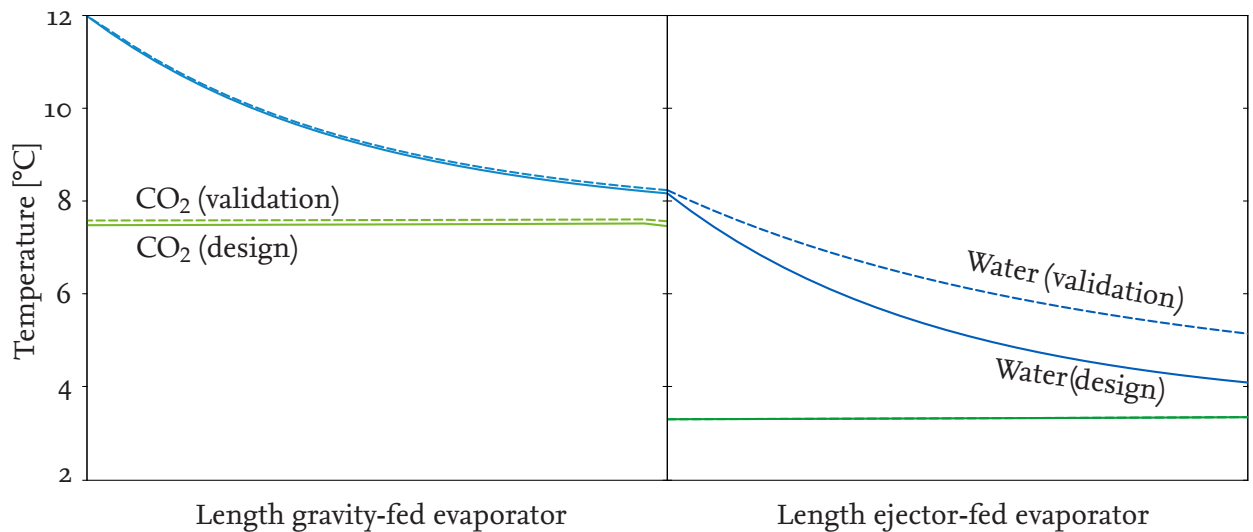


Figure 4.3: Temperature distribution curve for water and CO<sub>2</sub> in the gravity- and ejector-fed evaporator. Blue lines represent the temperature profile of the water and green lines represent the temperature profile of the CO<sub>2</sub>. The solid lines represent the curves under design conditions and the dashed lines represent the curves after correction of the heat transfer model in the ejector-loop for validation.

With the adjustments to the ejector efficiency and the Longo correlation in the ejector-fed evaporator, a validation of the simulation model could be carried out. This is shown in Figure 4.4 a) for the gravity-fed evaporator and in b) for the ejector-fed evaporator. The two diagrams show the deviations between the experimentally determined cooling capacity (X-axis) and the cooling capacity determined in the simulation (Y-axis). For validation, 12 different operating points were compared. This investigation was performed at an ejector-fed evaporator outlet pressure of 38 bar, at three different water inlet temperatures (12 °C, 15 °C, and 20 °C), and four different water mass flows be-

tween  $12 \text{ kg min}^{-1}$  to  $24 \text{ kg min}^{-1}$ . For the gravity-fed evaporator, for which the validation is shown in Figure 4.4 a), all points are within a deviation of  $\pm 15\%$ . For the validation of the ejector-fed evaporator, which can be seen in part b) of the figure, good agreement was achieved at least for the design temperature of  $12^\circ\text{C}$  for all four mass flows. The maximum deviation was around  $7\%$ . For  $15^\circ\text{C}$ , the values deviated slightly more significantly. However, all but one point, which deviated  $16\%$ , remained within the  $\pm 15\%$ . At the last operating points with  $20^\circ\text{C}$ , only the point of highest water mass flow of  $24 \text{ kg min}^{-1}$  was able to stay within the  $\pm 15\%$ . For all other points, the simulated cooling capacity was up to  $22\%$  above the measured one. Despite these deviations, the validation is considered successful for both evaporators. Further investigation into the differences between the model and reality should be carried out in future studies to determine the cause of the differences.

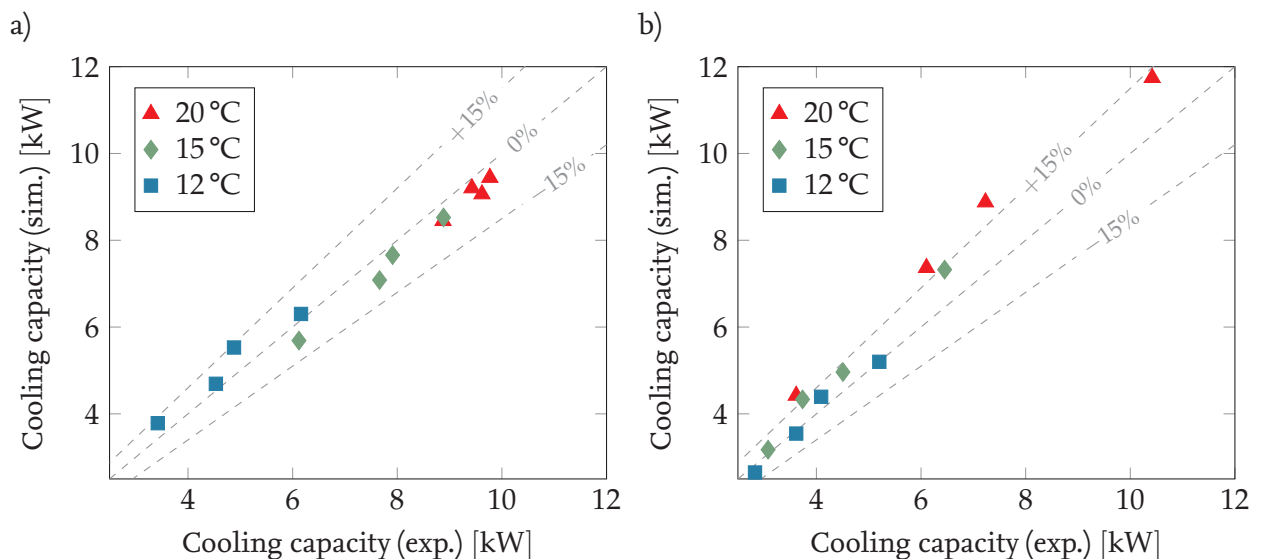


Figure 4.4: Validation of the two-stage evaporator with a water mass flow of  $24$ ,  $18$ ,  $16$  and  $12 \text{ kg/min}$  for a) the gravity-evaporator loop with  $12$  different operating points and b) the ejector-fed evaporator for  $12$  different operating points at  $38 \text{ bar}$  evaporation pressure.

The cooling capacities determined experimentally were calculated on the basis of the measured water-side temperature differences. For the measurement of the water temperature between the two evaporators, a sensor was installed in one of the two free lower connections of the water side. The free connection is shown in Figure 2.9 (connection without entering arrow). This measuring point should be checked and adjusted during the modification of the test rig as this is the source for the strong deviation between the heat transfer characteristics of the two identical evaporators. For example, an array of probes could be installed instead of just one sensor, and an average could then be calculated from the various measurement results. In addition, the sensor could be equipped with a device that generates turbulence at the measuring point, so that local stratification of the water at the measuring point can be avoided.

Future studies should continue to improve the performance of the ejector and the vapor fraction at the outlet of the ejector-fed evaporator. For the measurement results, the vapor fraction used

for validation was on average 41 %. In general, however, a vapor fraction of around 80 % should be aimed for, as with the gravity-fed evaporator. Nevertheless, care should be taken to ensure that the refrigerant does not superheat. This can be easily achieved by controlling the opening cross-section of the expansion valve and thus the outlet condition of the evaporator. With a higher vapor fraction, the ejector also needs to suck in less liquid phase. This, in combination with a higher high pressure or a lower outlet temperature from the IHX, should improve the efficiency of the ejector noticeably. At the same time, the ejector efficiency calculated from the measured values (e.g. 10.4 % from Table 4.2) and the ejector efficiency required in the simulation model for a similar pressure lift (5.5 %) deviate strongly.

### Stationary investigation of the performance of the heat pump chiller

In order to investigate how the heat pump chiller behaves under different water inlet temperatures and evaporation pressures, a variation of these boundary conditions was carried out. The water inlet temperature was varied between 9 °C and 18 °C in one degree celsius steps. This variation of the water inlet temperature was carried out for an ejector-fed evaporator outlet pressure of 41 bar, 38 bar and 35 bar. The results of this are shown in Figure 2.3. The combined COP (see equation 2.3) is shown over the water inlet temperature. The lowest COPs were determined at 35 bar, the highest at 41 bar. This is due to the fact that the pressure ratio between suction and discharge pressure of the compressor is lower at higher evaporating pressures and therefore less work has to be done. The curves at 35 bar and at 38 bar show a maximum. This is for 35 bar at 15 °C and for 38 bar at 17 °C. This is due to the fact that the pressure lift of the ejector is greatest at these points.

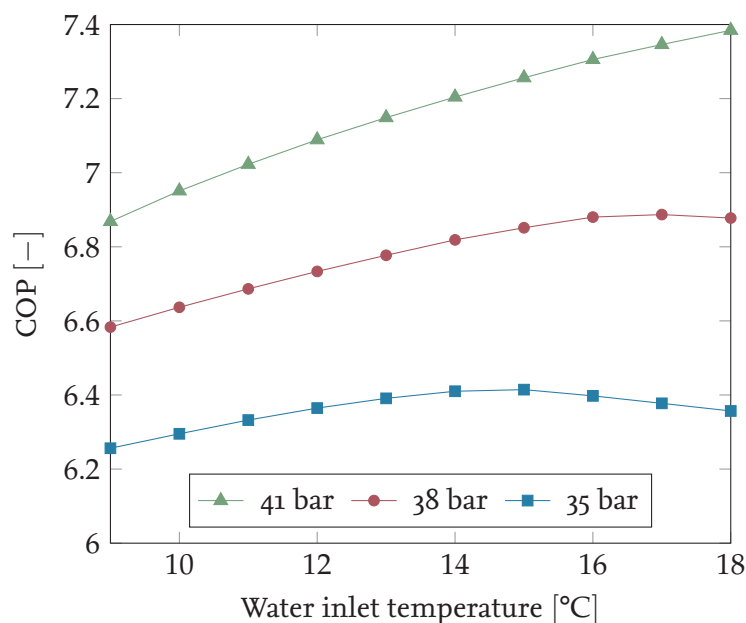


Figure 4.5: Investigation of the influence of different water inlet temperatures on the combined COP of the Heat pump chiller at three different ejector-fed evaporation pressures

## 4.3 Adjustments of the current design for further investigations

Through this work and that of Hafsås [22], initial investigations with the novel two-stage evaporator have been carried out both by simulation and experiments. It was possible to gain knowledge about the operation, behavior and characteristics of the heat pump chiller with the novel two-stage evaporator and thus also for the test rig. One finding, for example, was the high pressure drop across the mass flow sensors, which is why the gravity-fed evaporator could not deliver the expected results. This chapter therefore deals with how the simulation model and the test rig should be modified and operated to achieve better results.

### New boundary conditions for the simulation model and the test rig

In order to be able to make these adjustments, boundary conditions must first be defined in order to be able to deliver meaningful comparable results. So far, the experiments have been carried out with a constant cross-section of the expansion valve. To ensure that the ejector always sucks in a constant vapor fraction, the expansion valve should now be controlled. The setpoint for the control is the vapor fraction at the outlet of the ejector-fed evaporator. This setpoint is defined as 90 % vapor fraction. In addition, the conditions of the motive flow of the ejector should be better selected in order to achieve a better performance of the ejector and thus of the entire system. This could be done by considering the study of Elbarghthi et al. [11] who investigated the behavior of an ejector in the test rig used for this work. However, it is generally difficult to say which conditions in laboratory operation will result in stable behavior of the test rig with high ejector efficiency for all boundary conditions to be investigated. If the experiments on the test rig continue to be carried out with a high pressure of 80 bar, the motive temperature of the ejector should be lowered from 35 °C to e.g. 25 °C. Another possibility is to increase the pressure to, for instance, 90 bar. If these better operation conditions are taken into account, ejector efficiencies between 20 % and 30 % should not be a problem according to Elbarghthi et al. [11] at the investigated test rig. In order to have uniform conditions, the motive ejector conditions for the optimization of the test rig were set to 25 °C, a pressure of 90 bar and an ejector efficiency of 21 %. The goal of the redesign is to generate a cooling capacity of 10 kW with each of the two evaporators and thus pre-cool the water in two stages from 12 °C to 8 °C and then exit the evaporator at 4 °C. To achieve this, the water mass flow must be increased to 36 kg min<sup>-1</sup>. To ensure a constant water outlet temperature, the compressor control was modified so that the outlet temperature serves as the new setpoint for the compressor speed control. The gravity-fed evaporator should be adjusted to provide a vapor fraction of 80 % at the outlet under these conditions.

### Possible adjustments for an optimized test rig

In addition to the operating behavior and the boundary conditions, there are also design measures to optimize the test rig. These are mainly carried out on the gravity-fed evaporator loop. In chapter 3.2, the effects of different static heights and riser diameters on the performance of the gravity loop were shown. On the basis of this knowledge, various ways of achieving the desired results by

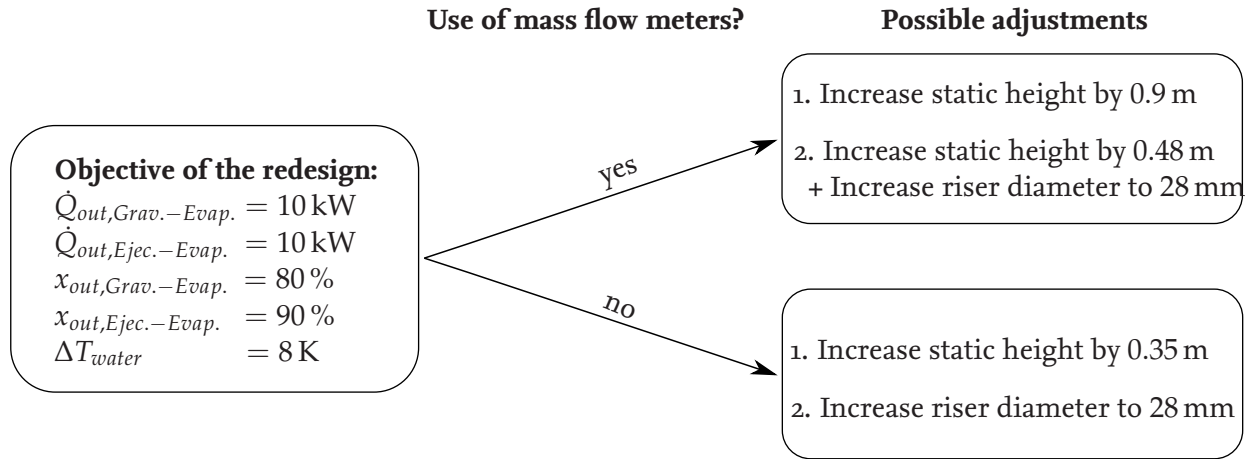


Figure 4.6: Schematic illustration of the possible adjustments for the redesign of the test rig with and without a mass flow sensor

means of a redesign will now be shown. An decisive aspect of these suggestions is that they can be implemented in the existing test rig. In the current test rig, the static height of the downcomer is 0.795 m. Of this, 0.265 m is the refrigerant charge height in the separator and 0.53 m of it is height of the vertical pipe of the downcomer. If the static height is now to be changed, this can be done by changing the length of the pipe. The internal diameter of the piping in the gravity-evaporator loop is currently 14 mm.

In order to be able to make statements about the possible adjustments, the new boundary conditions were implemented in the simulation model. By changing the static height and the inner diameter of the riser, different ways of achieving the objectives of the redesign were identified. Since the validation in chapter 3 and 4 showed a high pressure loss, which is assumed to be mainly caused by the mass flow sensor, it should also be discussed whether these are necessary at all or can be replaced by other measurement methods that do not cause any pressure loss. The different possibilities of adjustment are shown in Figure 4.6. It shows the different possibilities of adjustments for the redesign of the test rig with and without mass flow sensors. If the mass flow sensors are to be retained, the static height can be increased by 0.9 m to a total of 1.695 m. Another possibility is to increase the riser diameter to 28 mm. Then, only an increase of the static height by 0.48 m to a total of 1.275 m would be necessary. If the coreolis mass flow sesors can be dispensed with, the static height would only have to be increased by 0.35 m to a total of 1.145 m with no change in the riser diameter. An alternative option would be to only increase the riser diameter to 28 mm to achieve the objective values. Before deciding on one or the other variant, however, it should first be investigated whether the two mass flow sensors really achieve the pressure loss predicted during validation. This can be done by removing at least the mass flow sensor in the gravity-fed evaporator loop. Subsequently, some operating points already investigated in this work should be re-examined and the cooling capacity and vapor fraction compared.



## 4.4 Effect of the division of the number of plates in the two-stage evaporator

In this chapter, the aim is to determine whether the heat exchanger surface should be distributed evenly over both pressure stages, as in the prototype, or whether an uneven distribution of the number of plates would be advantageous. The two-stage evaporator prototype consists of 80 plates, half of which (40 plates) are used for the gravity-fed and the other half for the ejector-fed evaporator. For the investigation, the number of plates was distributed so that the sum of both evaporators was always 80 plates. The operating conditions were selected on the basis of Chapter 4.3 and Figure 4.6. The pressure loss of the mass flow sensor was omitted. In addition, the static height of the gravity-fed evaporator was increased by 0.35 m to a total height of 1.145 m as described in Chapter 4.3. For both evaporators, a plate split of 5 to 75 up to 75 to 5 was investigated. The results of the influence of the division of the number of plates on the performance of the two-stage evaporator are shown in Figures 4.7, 4.8, and 4.9.

Figure 4.7 shows the cooling capacity of both evaporators and the vapor fraction at the outlet of both evaporators versus the number of plates in the gravity-fed evaporator. If only 5 plates are used in the gravity-fed evaporator and 75 in the ejector-fed evaporator, the cooling capacity  $\dot{Q}_{EFE}$  is to 75 % on the ejector-fed evaporator. This is equivalent to a cooling capacity of 15 kW. As the number of plates in the gravity-fed evaporator increases, so does the proportion of the cooling capacity. At the same time, the cooling capacity in the ejector-fed evaporator  $\dot{Q}_{EFE}$  decreases by the same share that  $\dot{Q}_{GFE}$  increases. If the heat exchanger surface is evenly distributed with 40 plates each, there is an inflection point and intersection of the two cooling capacity curves at 10 kW each. With a shift of the plate distribution to the gravity-fed evaporator,  $\dot{Q}_{GFE}$  increases to 14 kW at 75 to 5 plates. This corresponds to a share of 75 % of the total cooling capacity.  $\dot{Q}_{EFE}$  continues to decrease by the share that  $\dot{Q}_{GFE}$  increases. If the number of plates in the gravity-fed evaporator increases, the vapor fraction  $x_{GFE}$  at the outlet of the evaporator also increases. Starting at a vapor fraction of 57 %, the curve runs similarly to the  $\dot{Q}_{GFE}$  curve. With an even distribution of the plates,  $x_{GFE}$  reaches the vapor fraction of 80 % targeted in the design and then continues to rise to 100 %. As intended, the vapor fraction at the outlet of the ejector-fed evaporator remains constant at 90 %.

Furthermore, the influence of the distribution of the number of plates in the two-stage evaporator on the coefficient of performance is considered. This is shown in Figure 4.8. It shows the refrigeration COP over the number of plates in the gravity-fed evaporator. As the number of plates in the gravity-fed evaporator increases, the COP also increases to a value of 3.62. This maximum COP takes place with an evenly distributed number of plates of 40 each. As can be seen in Figure 4.7, there is a uniform cooling capacity distribution of 10 kW each. At the same time, the temperature difference of the water to be cooled is also evenly distributed over the respective evaporator at this point with 4 K each. If the number of plates is changed by 20 in both directions from the high point at 40, there is hardly any difference in the COP. Only with a distribution of 70 to 10 plates in favor of the gravity-fed evaporator is a lower COP clearly visible. With a 75 to 5 split, the difference is even more pronounced with a COP of 3.43 to 3.49.

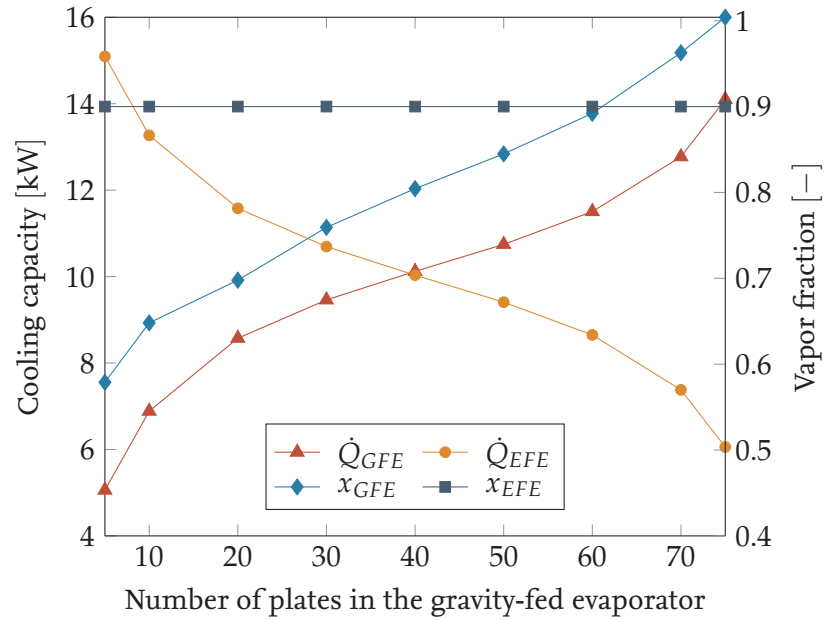


Figure 4.7: Influence of the division of the number of plates in the two-stage evaporator on the cooling capacity distribution and the vapor fraction in both evaporators. The number of plates of the gravity-fed evaporator is shown on the X-axis. Together with the ejector-fed evaporator, the total number of plates is always 80.

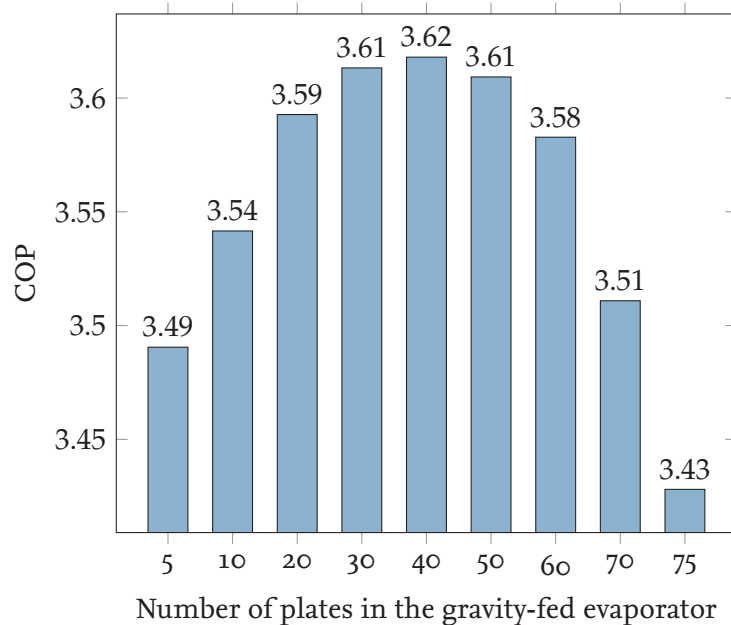


Figure 4.8: Effect of the division of the number of plates in the two-stage evaporator on the refrigeration COP. On the X-axis the number of plates of the gravity-fed evaporator is shown. Together with the ejector-fed evaporator, the total number of plates is always 80.

In order to better visualise the interaction between the cooling capacity distribution and the relative change of the COP to the maximum COP of the study, this is illustrated in Figure 4.9. The curve rises steeply up to a cooling capacity distribution  $\dot{Q}_{GFE}/\dot{Q}_{EFE}$  of 1. At this point, the relative change of the COP to the maximum COP ( $\text{COP}/\text{COP}_{max}$ ) is also 1. From Figure 4.8 it is known that the maximum COP for an even distribution of the heat exchanger surfaces has a value of 3.62. From the curve it can be concluded that an uneven distribution of the cooling load among the evaporators has an unfavorable effect on the system efficiency. This influence is higher with a larger share of the cooling capacity on the gravity-fed evaporator and leads in this investigation to a deviation of the COP from the maximum COP of more than 5%. This may be due to the fact that the vapour fraction at this point with 100% leads to a reduced heat transfer. On the other hand, the separator pressure  $p_{sep}$  increases in a similar way as the relative change of the COP, as can be seen in the figure. It shows its maximum at a separator pressure of 41.63 bar at a cooling load distribution  $\dot{Q}_{GFE}/\dot{Q}_{EFE}$  of 1. Since the separator pressure is also the suction pressure of the compressor, low pressures lead to more compressor work and thus to a lower COP.

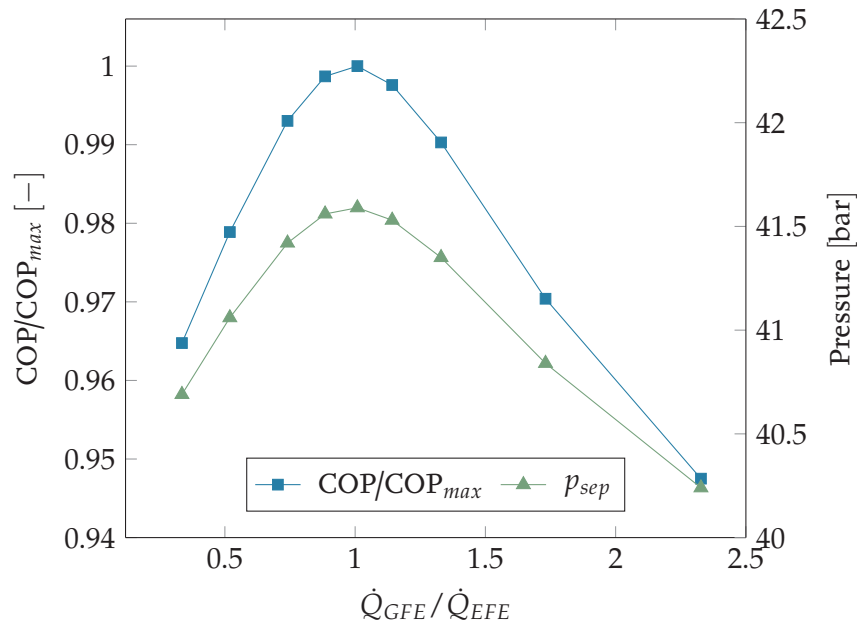


Figure 4.9: Effect of the division of the number of plates in the two-stage evaporator on the relative change of the refrigeration COP ( $\text{COP}/\text{COP}_{max}$ ) and on the separator pressure ( $p_{sep}$ ) over the refrigeration load distribution between gravity-fed  $\dot{Q}_{GFE}$  and ejector-fed evaporators  $\dot{Q}_{EFE}$ .

In summary, an even distribution of the heat exchanger surface and thus of the number of plates led to the best results. In this way, the cooling capacities and the temperature differences of the water to be cooled are equally distributed between the two stages. Another observation is that the pressure lift generated by the ejector is 4 bar for the same number of plates. Under the boundary conditions considered, a cooling of the water from 12 °C to 4 °C was aimed for. Thereby, the temperature glide was divided equally with 4 K on both evaporators. Since the  $\Delta p/\Delta T$  ratio in the two-phase region of  $\text{CO}_2$  is approximately 1 bar/K, it can be concluded from this observation that the optimum pressure lift to be generated by the ejector is half of the target temperature glide across the two-stage

evaporator. If the temperature glide is to be 10 K instead of 8 K, the optimum pressure lift of the ejector in this case is 5 bar. This should be investigated in more detail as part of future work.

## 4.5 Part load behavior of the system

Depending on the application, heat pump chillers operate outside their design point most of the year. Therefore, in addition to considering the design case, the system behavior under part load is also crucial. This is why the cooling load was gradually reduced by half from 20 kW to 10 kW in this chapter. For this purpose, the target water outlet temperature was gradually increased in 1 K steps from 4 °C (design condition) to 8 °C. In Figure 4.10, the part-load behavior of the two-stage evaporator system was investigated based on the cooling capacity distribution and the refrigeration COP over the water outlet temperature of the ejector-fed evaporator. The operating conditions were selected on the basis of Chapter 4.3 and Figure 4.6. The pressure loss of the mass flow sensor was omitted. In addition, the static height of the gravity-fed evaporator was increased by 0.35 m to a total height of 1.145 m as described in Chapter 4.3. In the design point at a water outlet temperature of 4 °C, the cooling capacity is evenly distributed between the two evaporators. As the outlet water temperature increases, the load distribution shifts further in the direction of the ejector-fed evaporator. At a water outlet temperature of 8 °C, almost 65% of the cooling capacity is provided by the ejector-fed evaporator. The refrigeration COP, on the other hand, increases with the water outlet temperature from 3.62 at design point to 4.03 at half load. This is due to the fact that the evaporating pressure in both evaporators increases, as can be seen in Figure 4.11.

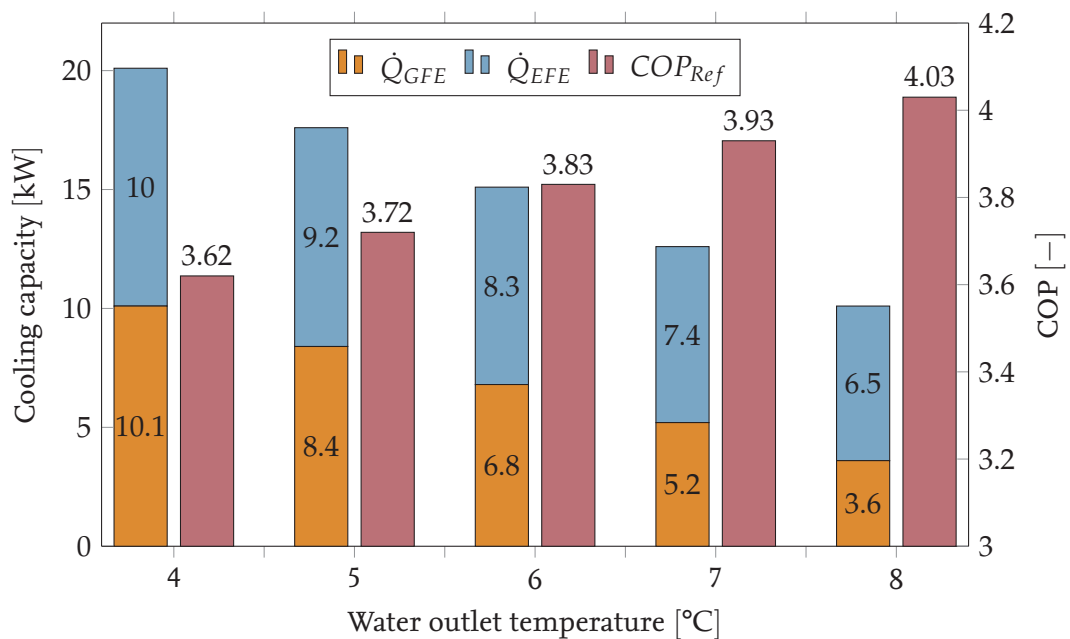


Figure 4.10: Investigation of the part load behavior of the two-stage evaporator system based on the cooling capacity distribution and the refrigeration COP over the water outlet temperature of the ejector-fed evaporator. (Water inlet temperature constant at 12 °C)

Figure 4.11 shows the two evaporation pressures in the gravity-fed evaporator  $p_{GFE}$  and ejector-fed evaporator  $p_{EFE}$ . In addition the vapor fraction at the outlet of the two evaporators  $x_{GFE}$  and  $x_{EFE}$  over the water outlet temperature of the ejector-fed evaporator is shown. As the outlet water temperature increases, the evaporating pressure in the gravity-fed evaporator also increases from 41.63 bar at 4 °C water outlet temperature to 45.12 bar at 8 °C. In the ejector-fed evaporator, the pressure increases simultaneously from initially 37.52 bar to 42.02 bar. Thus, the pressure lift of the ejector gradually decreases from 4 bar at full load to 3 bar at the lowest part load investigated. While the vapor fraction at the outlet of the ejector-fed evaporator remains constant at 90 %, the vapor fraction at the outlet of the gravity-fed evaporator decreases from originally 80 % to about 29 %.

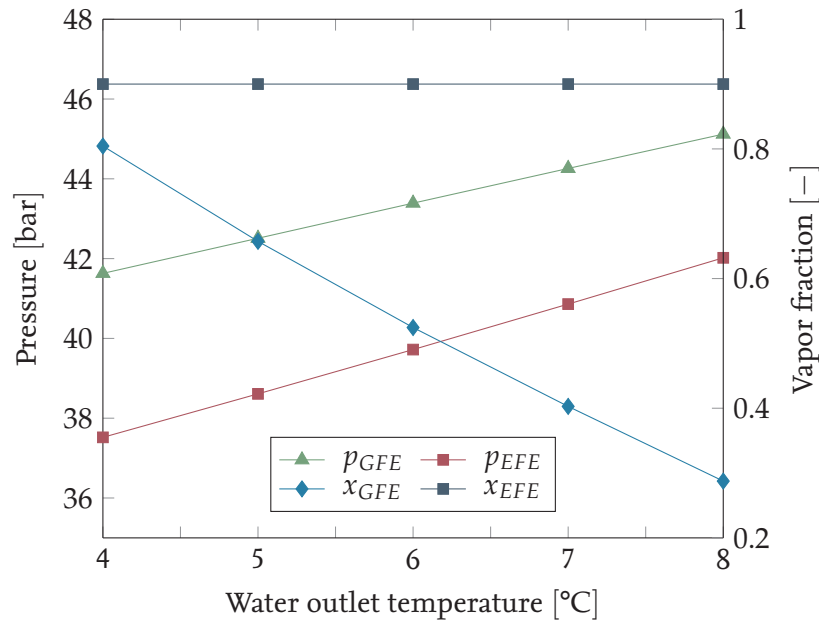


Figure 4.11: Investigation of the part load behavior of the two-stage evaporator system based on the evaporating pressure in the gravity-fed evaporator  $p_{GFE}$  and ejector-fed evaporator  $p_{EFE}$ , and the vapor fraction at the outlet of the two evaporators  $x_{GFE}$  and  $x_{EFE}$  over the water outlet temperature of the ejector-fed evaporator.

Finally, based on the distribution of the refrigerant mass flow to the gravity-fed evaporator  $\dot{m}_{GFE}$  and the ejector-fed evaporator  $\dot{m}_{EFE}$  as well as the water-side temperature difference across the two evaporators  $\Delta T_{w,GFE}$  and  $\Delta T_{w,EFE}$  over the water outlet temperature of the ejector-fed evaporator, the part-load behavior is shown in Figure 4.12. As the water outlet temperature increases, the refrigerant mass flow rate  $\dot{m}_{GFE}$  flowing through the gravity-fed evaporator increases slightly. In contrast, the refrigerant mass flow rate over the ejector-fed evaporator  $\dot{m}_{EFE}$  decreases from an initial  $3.17 \text{ kg min}^{-1}$  to  $2.17 \text{ kg min}^{-1}$ . This is because the expansion valve upstream of the ejector-fed evaporator controls the refrigerant mass flow so that the vapor fraction is constant at 90 %. At the design point, the water temperature differences are both 4 K. Subsequently, both temperature differences decrease with increasing water outlet temperature. The temperature difference  $\Delta T_{w,GFE}$  decreases faster than  $\Delta T_{w,EFE}$ . At the highest water outlet temperature, the temperature difference

$\Delta T_{w,GFE}$  is 1.42 K and  $\Delta T_{w,EFE}$  is 2.58 K.

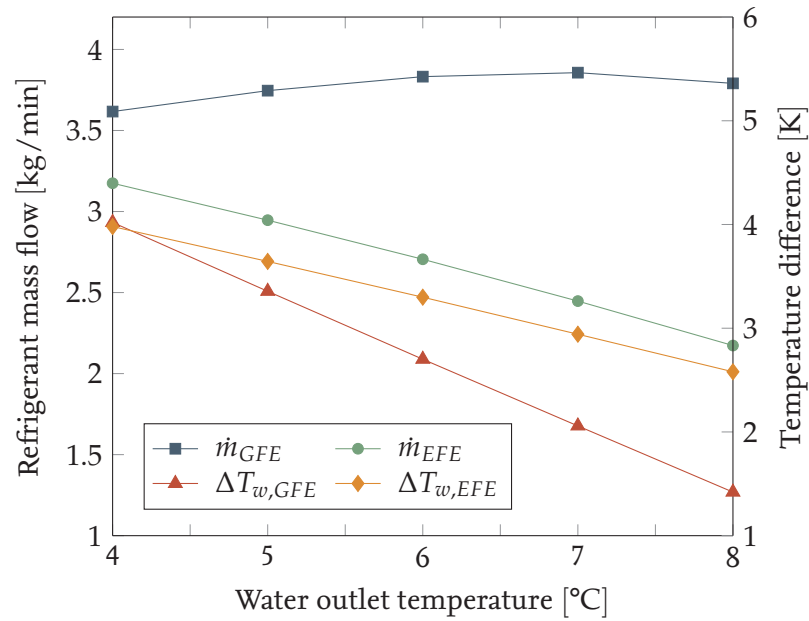


Figure 4.12: Investigation of the part load behavior of the two-stage evaporator system based on the distribution of the refrigerant mass flow on the gravity-fed evaporator  $\dot{m}_{GFE}$  and the ejector-fed evaporator  $\dot{m}_{EFE}$  as well as the water-side temperature difference over the two evaporators  $\Delta T_{w,GFE}$  and  $\Delta T_{w,EFE}$  over the water outlet temperature of the ejector-fed evaporator.

The investigation of the part-load behavior has shown that the load distribution shifts to the ejector-fed evaporator when the load decreases. At the same time, the COP increases due to the rising evaporating pressure. Since it was shown in chapter 4.4 that an even load distribution is the most efficient, further work should investigate the degree to which a constant load distribution is possible even at part load and how this can be implemented.

# 5 Summary and outlook

Heat pump chillers currently available on the market often suffer from either insufficient cooling capacity or from too high space requirements. To address both issues simultaneously, a compact, novel two-stage evaporator was developed at NTNU in collaboration with SINTEF and Alfa Laval. It consists of two commercially available brazed plate heat exchangers which are assembled back to back. The compactness and thus uniqueness of this heat exchanger is due to an internal connection of the secondary loop between the two evaporators. This means that only two connections are required for the secondary fluid, thus saving pipework and space. In addition, the two-stage evaporator is also novel due to its mode of operation. Both evaporators are operated at different evaporation pressures. By using the thermosyphon principle, the medium-pressure evaporator, in which the secondary fluid is pre-cooled, is operated as a flooded gravity-fed evaporator. The low-pressure evaporator is operated as an ejector-fed evaporator via the suction mass flow of the ejector and cools the secondary fluid further down to the outlet temperature. All of this results in a higher temperature differential across the secondary fluid, a higher volumetric capacity of the evaporator and the overall system, and better system performance due to a two-stage evaporation and the higher compressor suction pressure enabled by the ejector.

In this thesis, this novel two-stage evaporator was investigated. This was done with the help of simulation models that were created in the course of this work using the TIL library. Furthermore, the simulation model was validated with the help of measurement data from a test rig. For this purpose, the state of the art of CO<sub>2</sub> heat pump chillers was first summarized and a concept for a heat pump chiller was developed on its basis. Then the model was developed and the system was investigated and validated in two steps. First, the simulation model for the gravity-fed evaporator loop was developed and extended into a heat pump chiller model with a single-stage evaporator. The model was then validated and model-based investigations were carried out. With the help of the gravity-fed evaporator model, important knowledge was gained about the behavior of the gravity loop under different boundary conditions. This also included insights into the correct dimensioning and operating mode. By integrating the pressure loss from the Coriolis mass flow sensor of the test rig, the simulation results could be adapted to the measurement results and therefore be validated. In addition, it was found that the gravity-fed evaporator is operating in the best way, if the refrigerant exits the evaporator at a vapor fraction by 80%. Furthermore, when investigating the influence of the dimensioning of the gravity loop, it was discovered that a reduction of the vapor fraction either by doubling the riser diameter compared to the downcomer diameter or by increasing the static height by 0.3 m leads to a reduction of the vapor fraction of 15%. By varying the water inlet temperature and the water mass flow rate, the behavior of the gravity-fed evaporator loop was investigated under different boundary conditions. Both the variation of the water inlet temperature and the variation of the water mass flow lead to a change of the cooling capacity and thus to a similar behavior of the gravity loop. It was discovered that the dimensioning of the gravity loop has

an influence on the maximum cooling capacity. Under the operating conditions considered, the maximum cooling capacity was about 13 kW. Furthermore, with the help of the validation and the other investigations, the interaction between the thermosyphon effect, the vapor fraction and the pressure drop was clarified, which have a significant influence on the performance of the gravity-fed evaporator loop. Therefore, avoidable pressure losses should be eliminated. The findings and main results of the first part of the work have already been presented at the 15<sup>th</sup> IIR-Gustav Lorenzen Conference and published as a conference paper [24]. This paper is attached to this thesis in Appendix F.

The second step was to extend the model to include the ejector-fed evaporator, to validate the two-stage evaporator with the aid of measurement data and to carry out further model-based investigations. After extending the model to include the ejector-fed evaporator, it was possible to adapt the simulation model to match the measured values from the test rig. For the gravity-fed evaporator, the validation could be carried out similarly to the first part of this thesis. However, this was not the case for the validation of the ejector-fed evaporator. Therefore, in the simulation model, the correlation of the heat transfer model (Longo) in the ejector-fed evaporator had to be multiplied by a correction factor of 0.2 to achieve results similar to the measured values. Thus, the measured data should be treated with caution. By modifying the test rig, for example by installing a probe array for water temperature measurement and improving the control of the ejector performance, the measurement results should be verified and a new validation should be carried out. With the help of the knowledge gained from the simulations and the findings from the test rig described in Hafsås [22], the simulation model was further optimized. Thus, further model-based investigations could be carried out. These findings can also be transferred to the optimization of the test rig. With the aid of the optimized simulation model, the optimum distribution of the heat exchanger surfaces between the two evaporator stages was then investigated. It was found that an even distribution of the heat exchanger surface leads to an even distribution of the cooling capacity and thus to the best results. With the same distribution of the heat exchanger surfaces, the refrigeration COP is at a maximum value of 3.62 in this investigation. This is also due to the fact that with the same distribution, the separator pressure is at its peak, which means that the least amount of compressor work is required. Additionally, it was concluded from the observations that the optimum pressure lift of the ejector should be half of the value of the target temperature glide of the secondary fluid across both evaporators. Further research should be carried out in the following work to investigate this conclusion further. Since, depending on their application, heat pump chillers are operated outside the design point for most of the year, the part load behavior was also investigated. Compared to the design point, where the load was distributed equally between both evaporators, the load distribution in the part load case was more heavily on the ejector-fed evaporator. At the same time, the COP increases with decreasing load, so a good part load behavior is provided by the system. However, this is not due to a better distribution of the cooling capacity but due to the increasing evaporating pressure as the water outlet temperature from the evaporator increases. Since the results showed that a uniform load distribution leads to the best results, the following work should investigate if a constant load distribution is also possible at part load. The findings of the second part of the work should be presented at the 26<sup>th</sup> International Congress of Refrigeration 2023. For this purpose, an abstract has been submitted, which can be seen in Appendix G.



# Bibliography

- [1] ALFA LAVAL: *Alfa Laval AXP14: Brazed plate heat exchanger for extreme high-pressure requirements.* [https://www.alfalaval.com/globalassets/documents/products/heat-transfer/plate-heat-exchangers/brazed-plate-heat-exchangers/axp/axp14\\_productleaflet\\_CHE00017EN.pdf](https://www.alfalaval.com/globalassets/documents/products/heat-transfer/plate-heat-exchangers/brazed-plate-heat-exchangers/axp/axp14_productleaflet_CHE00017EN.pdf)
- [2] ALLOUCHE, Y. ; SMITT, S. ; HAFNER, A. : *Educational e-book about MultiPACK No 2: Thermal Energy storage integrated into CO<sub>2</sub> heat pump systems.* [https://www.ntnu.edu/documents/1272037961/0/723137\\_Deliverable\\_16\\_%28Educational+e-book+about+MULTIPACK+No+2%29.pdf/b544d606-c41e-390f-5be6-c82512af7318?t=1616766385953](https://www.ntnu.edu/documents/1272037961/0/723137_Deliverable_16_%28Educational+e-book+about+MULTIPACK+No+2%29.pdf/b544d606-c41e-390f-5be6-c82512af7318?t=1616766385953)
- [3] BAEHR, H. D. ; STEPHAN, K. : *Wärme- und Stoffübertragung.* Berlin, Heidelberg : Springer Berlin Heidelberg, 2019. <http://dx.doi.org/10.1007/978-3-662-58441-5>. <http://dx.doi.org/10.1007/978-3-662-58441-5>. – ISBN 978–3–662–58440–8
- [4] BRENNEN, C. E.: *Fundamentals of multiphase flow.* Cambridge : Cambridge Univ. Press, 2005. – ISBN 0521 848040
- [5] BYRNE, P. ; GHOUBALI, R. ; DIABY, A. T.: *Heat pumps for simultaneous heating and cooling.* <https://hal.archives-ouvertes.fr/hal-01990466/document>. Version: 2019
- [6] CAO, X. ; LIANG, X. ; SHAO, L. ; ZHANG, C. : Performance analysis of an ejector-assisted two-stage evaporation single-stage vapor-compression cycle. In: *Applied Thermal Engineering* 205 (2022), S. 118005. <http://dx.doi.org/10.1016/j.applthermaleng.2021.118005>. – DOI 10.1016/j.applthermaleng.2021.118005. – ISSN 13594311
- [7] CASINI, M. ; DIE KÄLTE & KLIMATECHNIK (Hrsg.): *CO<sub>2</sub>-Verdichter und -Ausrüstungen, Anwendung und Verfügbarkeit.* [https://www.diekaelte.de/sites/default/files/ulmer/file\\_173159.pdf](https://www.diekaelte.de/sites/default/files/ulmer/file_173159.pdf). Version: 2001
- [8] CHENG, L. ; RIBATSKI, G. ; THOME, J. R.: New prediction methods for CO<sub>2</sub> evaporation inside tubes: Part II—An updated general flow boiling heat transfer model based on flow patterns. In: *International Journal of Heat and Mass Transfer* 51 (2008), Nr. 1-2, S. 125–135. <http://dx.doi.org/10.1016/j.ijheatmasstransfer.2007.04.001>. – DOI 10.1016/j.ijheatmasstransfer.2007.04.001. – ISSN 00179310
- [9] ECKERT, M. (Hrsg.) ; KAUFFELD, M. (Hrsg.) ; SIEGISMUND, V. (Hrsg.): *Natürliche Kältemittel: Anwendungen und Praxiserfahrungen.* Berlin and Offenbach and Karlsruhe : VDE Verlag GmbH and cci Dialog GmbH, 2019 (cci Buch). – ISBN 9783800739363
- [10] ELARGA, H. ; SHERMAN, P. K. ; HAFNER, A. : *Educational e-book about MultiPACK No 3: CO<sub>2</sub> refrigeration and heat pump systems.* [https://www.ntnu.edu/documents/1272037961/0/723137\\_Deliverable\\_17\\_Educational+e-book+about+MULTIPACK+No+3+%283%29.pdf/bdf62beb-47ac-0999-6006-fe067c100fc2?t=1638259340299](https://www.ntnu.edu/documents/1272037961/0/723137_Deliverable_17_Educational+e-book+about+MULTIPACK+No+3+%283%29.pdf/bdf62beb-47ac-0999-6006-fe067c100fc2?t=1638259340299)

- [11] ELBARGHTHI, A. F. ; HAFNER, A. ; BANASIAK, K. ; DVORAK, V. : An experimental study of an ejector-boosted transcritical R744 refrigeration system including an exergy analysis. In: *Energy Conversion and Management* 238 (2021). <http://dx.doi.org/10.1016/j.enconman.2021.114102>. – DOI 10.1016/j.enconman.2021.114102. – ISSN 01968904
- [12] EUROPEAN COMMISSION: Stepping up Europe's 2030 climate ambition: Investing in a climate-neutral future for the benefit of our people. (2020). <https://eur-lex.europa.eu/legal-content/EN/TXT/PDF/?uri=CELEX:52020DC0562&from=EN>
- [13] EUROSTAT: Renewable energy for heating and cooling. In: *Eurostat* (11/2/2020). <https://ec.europa.eu/eurostat/web/products-eurostat-news/-/ddn-20200211-1>
- [14] FLEITERN, T. ; STEINBACH, J. ; RAGWITZ, MÜLLER, ANDREAS: *Mapping and analyses of the current and future (2020-2030) heating/cooling fuel deployment (fossil/renewables) Work package 1: Final energy consumption for the year 2012 Final report*
- [15] FÖRSTERLING, S. : *Vergleichende Untersuchung von CO<sub>2</sub>-Verdichtern in Hinblick auf den Einsatz in mobilen Anwendungen*. Cuvillier Verlag, 2004. – ISBN 9783736910805
- [16] GABRIELI, C. H.: KLD HFC free Chiller India: Environmental benefits of implementing a CO<sub>2</sub> heat pump for combined heating and cooling at Bengaluru centralised school kitchen. (2019). <https://sintef.brage.unit.no/sintef-xmlui/handle/11250/2647428?locale-attribute=en>
- [17] GULLO, P. ; FUSINI, L. ; HAFNER, A. : *Educational e-book about MultiPACK No 1*. [https://www.ntnu.edu/documents/1272037961/0/723137\\_Deliverable\\_16\\_%28Educational+e-book+about+MULTIPACK+No+1%29.pdf/37332fd4-da00-55d8-ab6f-ff7282949ec8?t=1616766346730](https://www.ntnu.edu/documents/1272037961/0/723137_Deliverable_16_%28Educational+e-book+about+MULTIPACK+No+1%29.pdf/37332fd4-da00-55d8-ab6f-ff7282949ec8?t=1616766346730)
- [18] GULLO, P. ; TSAMOS, K. ; HAFNER, A. ; GE, Y. ; TASSOU, S. A.: State-of-the-art technologies for transcritical R744 refrigeration systems – a theoretical assessment of energy advantages for European food retail industry. In: *Energy Procedia* 123 (2017), S. 46–53. <http://dx.doi.org/10.1016/j.egypro.2017.07.283>. – DOI 10.1016/j.egypro.2017.07.283. – ISSN 18766102
- [19] HAFNER, A. : The advantages of natural working fluids. (2019). <http://dx.doi.org/10.18462/IIR.ICR.2019.1030>. – DOI 10.18462/IIR.ICR.2019.1030
- [20] HAFNER, A. ; HAZARIKA, M. M. ; LECHI, F. ; ZORZIN, A. ; PARDIÑAS, Á. ; BANASIAK, K. : *Experimental investigation on integrated two-stage evaporators for CO<sub>2</sub> heat-pump chillers* (15th IIR-Gustav Lorentzen conference on Natural Refrigerants)
- [21] HAFNER, A. ; PARDIÑAS, Á. : CO<sub>2</sub> refrigeration technology: possible innovations. (2019). <http://dx.doi.org/10.18462/iir.nh3-co2.2019.0024>. – DOI 10.18462/iir.nh3-co2.2019.0024
- [22] HAFSÅS, J. : *Experimental study on the integration of a novel two-stage evaporator in a CO<sub>2</sub> heat pump chiller*
- [23] HAUKÅS, H. T.: *Design and optimization of flooded evaporators with natural circulation: The joint Israeli - Norwegian symposium on refrigeration Tel Aviv*. Trondheim, 1986

- [24] HAZARIKA, M. M. ; BENGSCHE, J. ; HAFSÅS, J. ; HAFNER, A. ; SVEMDSEM, E. S. ; YE, Z. : *Integration of gravity-fed evaporators in CO<sub>2</sub> based heat-pump chillers* (15th IIR-Gustav Lorentzen conference on Natural Refrigerants)
- [25] KARAMPOUR, M. ; SAWALHA, S. : State-of-the-art integrated CO<sub>2</sub> refrigeration system for supermarkets: A comparative analysis. In: *International Journal of Refrigeration* 86 (2018), S. 239–257. <http://dx.doi.org/10.1016/j.ijrefrig.2017.11.006>. – DOI 10.1016/j.ijrefrig.2017.11.006. – ISSN 01407007
- [26] LORENTZEN ; GUSTAV: Evaporator design and liquid feed regulation. In: *The Journal of Refrigeration* (1958)
- [27] LUCAS, C. ; KOEHLER, J. : Experimental investigation of the COP improvement of a refrigeration cycle by use of an ejector. In: *International Journal of Refrigeration* 35 (2012), Nr. 6, S. 1595–1603. <http://dx.doi.org/10.1016/j.ijrefrig.2012.05.010>. – DOI 10.1016/j.ijrefrig.2012.05.010. – ISSN 01407007
- [28] MAURER, T. : *Kältetechnik für Ingenieure*. Berlin and Offenbach : VDE Verlag GmbH, 2016. – ISBN 978–3–8007–3935–6
- [29] PALIWODA, A. : Calculation of basic parameters for gravity-fed evaporators for refrigeration and heat pump systems. In: *International Journal of Refrigeration* 15 (1992), Nr. 1, S. 41–47. [http://dx.doi.org/10.1016/0140-7007\(92\)90066-4](http://dx.doi.org/10.1016/0140-7007(92)90066-4). – DOI 10.1016/0140-7007(92)90066-4. – ISSN 01407007
- [30] PALIWODA, A. : Generalized method of pressure drop calculation across pipe components containing two-phase flow of refrigerants. In: *International Journal of Refrigeration* 15 (1992), Nr. 2, S. 119–125. [http://dx.doi.org/10.1016/0140-7007\(92\)90036-T](http://dx.doi.org/10.1016/0140-7007(92)90036-T). – DOI 10.1016/0140-7007(92)90036-T. – ISSN 01407007
- [31] RHEONIK GMBH: *Coreolis mass flow sensor RHM06*. <https://www.rheonik.com/products/small-size-sensors/rhm-06/>
- [32] SMITT, S. ; PARDIÑAS, Á. ; HAFNER, A. : Evaluation of Integrated Concepts with CO<sub>2</sub> for Heating, Cooling and Hot Water Production. In: *Energies* 14 (2021), Nr. 14, S. 4103. <http://dx.doi.org/10.3390/en14144103>. – DOI 10.3390/en14144103
- [33] STEPHAN, P. ; SCHABER, K. ; STEPHAN, K. ; MAYINGER, F. : *Thermodynamik: Grundlagen und technische Anwendungen Band 1: Einstoffsysteme*. 18. Aufl. 2009. Berlin, Heidelberg : Springer Berlin Heidelberg, 2008 (Springer-Lehrbuch). <http://dx.doi.org/10.1007/978-3-540-92895-9>. <http://dx.doi.org/10.1007/978-3-540-92895-9>. – ISBN 978–3–540–92894–2
- [34] SWEP INTERNATIONAL AB: *Flooded evaporators*. <https://www.swep.net/refrigerant-handbook/6.-evaporators/asas2/>
- [35] TLK-THERMO GMBH: *TIL Suite 3.11.0: Software package components*. <https://www.tlk-thermo.com/index.php/de/software/til-suite>

- [36] TOSATO, G. ; GIROTTO, S. ; MINETTO, S. ; ROSSETTI, A. ; MARINETTI, S. : An integrated CO<sub>2</sub> unit for heating, cooling and DHW installed in a hotel. Data from the field. In: *Journal of Physics: Conference Series* 1599 (2020), Nr. 1. <http://dx.doi.org/10.1088/1742-6596/1599/1/012058>. – DOI 10.1088/1742-6596/1599/1/012058. – ISSN 1742-6588
- [37] WEIGAND, B. ; KÖHLER, J. ; WOLFERSDORF, J. von: *Thermodynamik kompakt*. Berlin, Heidelberg : Springer Berlin Heidelberg, 2016. <http://dx.doi.org/10.1007/978-3-662-49703-6>. <http://dx.doi.org/10.1007/978-3-662-49703-6>. – ISBN 978-3-662-49702-9
- [38] YANG, L. ; LI, H. ; CAI, S.-W. ; SHAO, L.-L. ; ZHANG, C.-L. : Minimizing COP loss from optimal high pressure correlation for transcritical CO<sub>2</sub> cycle. In: *Applied Thermal Engineering* 89 (2015), S. 656-662. <http://dx.doi.org/10.1016/j.applthermaleng.2015.06.023>. – DOI 10.1016/j.applthermaleng.2015.06.023. – ISSN 13594311
- [39] ZENDEHBOUDI, A. ; YE, Z. ; HAFNER, A. ; ANDRESEN, T. ; SKAUGEN, G. : Heat transfer and pressure drop of supercritical CO<sub>2</sub> in brazed plate heat exchangers of the tri-partite gas cooler. In: *International Journal of Heat and Mass Transfer* 178 (2021), S. 121641. <http://dx.doi.org/10.1016/j.ijheatmasstransfer.2021.121641>. – DOI 10.1016/j.ijheatmasstransfer.2021.121641. – ISSN 00179310

# Appendix

# A Test rig setup



Figure A.1: Picture of the test rig

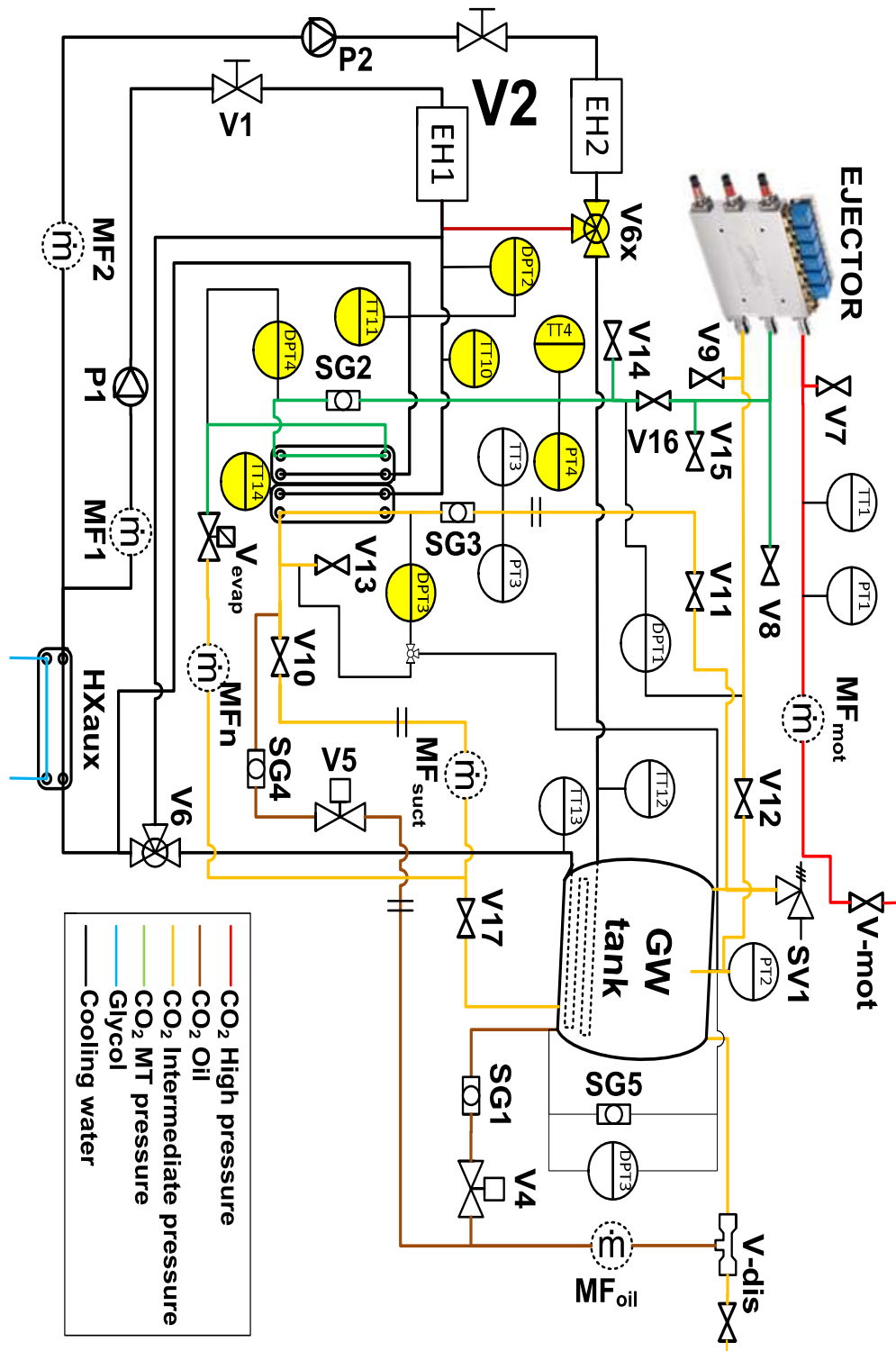


Figure A.2: P&ID of the laboratory test rig for the two-stage evaporator.

# B Interconnection of the cells in the heat exchanger

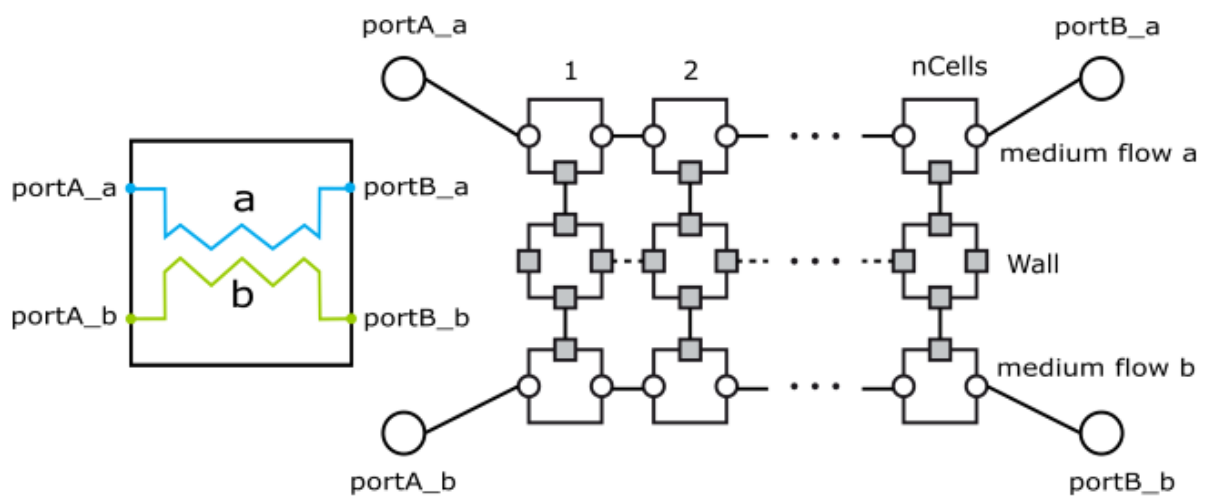


Figure B.1: Interconnection of the cells in the heat exchanger [35]



# C Controller settings

Table C.1: Controller setting for the gravity-fed evaporator system  
PI-Inline Boundary

Designation	Value	Unit
Proportional coefficient	1.00E-03	-
Reset time	3	s
Initial value	Pressure of the downcomer	bar

## PI-Compressor

Designation	Value	Unit
Proportional coefficient	4.00E-02	-
Reset time	5	s
Initial value	38	bar

## PI-Water mass flow GC

Designation	Value	Unit
Proportional coefficient	5.00E-02	-
Reset time	5	s
Initial value	GCWaterIn.TFixed + 3	K

## PI-Expansion valve

Designation	Value	Unit
Proportional coefficient	5.00E-08	-
Reset time	1	s
Initial value	120	bar

# D Pressure drop of the mass flow sensor

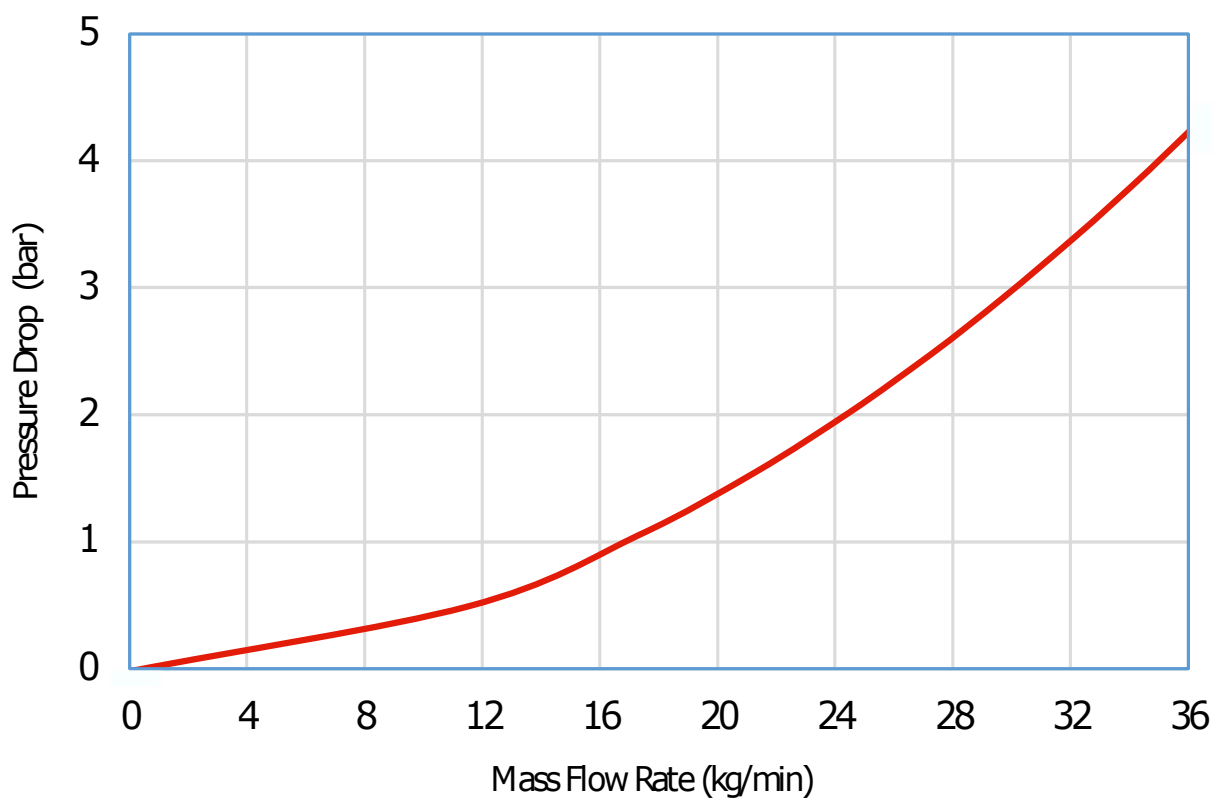


Figure D.1: Pressure drop curve the mass flow sensor: Rheonics coreolis mass flow sensor RHM 06 (Measured with water as fluid) [31]

# E Further data from the validation

Table E.1: Measured values compared with the simulated values for the gravity-fed evaporator and the ejector-fed evaporator with similar boundary conditions

	Designation	Measured value	Simulated value	Unit	Difference %
Gravity-fed evaporator	Separator pressure	42.2	42.21	[bar]	0.02
	Cooling capacity	6.2	6.511	[kW]	4.78
	Refrigeration mass flow	1.9	2.022	[kg/min]	6.03
	Vapor fraction evaporator outlet	92.4	93.48	[%]	1.16
	Water inlet temperature	12	12	[°C]	0
	Water outlet temperature	8.3	8.12	[°C]	-2.22
	Water mass flow	24	24	[kg/min]	0
Ejector-fed evaporator	Evaporation pressure	38	38	[bar]	0
	Cooling capacity	5.2	6.803	[kW]	23.57
	Refrigeration mass flow	3.3	3.173	[kg/min]	-4.01
	Vapor fraction evaporator outlet	42.5	63.1	[%]	32.65
	Water inlet temperature	8.3	8.12	[°C]	-2.22
	Water outlet temperature	5.2	4.072	[°C]	-27.7
	Water mass flow	24	24	[kg/min]	0
Ejector	Motive flow pressure	79.8	79.8	[bar]	0
	Motive flow temperature	35	35	[°C]	0
	Ejector efficiency	10	5.5	[%]	-81.82

**F Conference paper for the  
15th IIR-Gustav Lorentzen  
conference of Natural  
Refrigerants**

# Integration of gravity-fed evaporators in CO<sub>2</sub> based heat-pump chillers

Mihir Mouchum HAZARIKA<sup>(a)</sup>, Jan BENGSCHE<sup>(a)</sup>, Johan HAFSÅS<sup>(a)</sup>,  
Armin HAFNER<sup>(\*a)</sup>, Eirik Starheim SVENDSEN<sup>(b)</sup>, Zuliang YE<sup>(c)</sup>

<sup>(a)</sup>Norwegian University of Science and Technology, Trondheim, \*armin.hafner@ntnu.no

<sup>(b)</sup>Fisheries and New Biomarine Industry, SINTEF Ocean AS, Trondheim

<sup>(c)</sup>School of Energy and Power Engineering, Xi'an Jiaotong University, China

## ABSTRACT

This study is carried out to model a gravity-fed evaporator for CO<sub>2</sub> based heat-pump chillers. The gravity-fed evaporator loop consists of a separator, a downcomer, a heat exchanger, and a riser. The working principle is that the evaporation of fluid in the heat exchanger gives rise to a density gradient in the loop. This density gradient generates the buoyancy force which drives the fluid by overcoming all the pressure drops in the loop. Appropriate equations are derived to estimate these pressure resistances. Finally, the balance between the buoyancy forces and pressure resistances dictates the flowrate in the loop. This procedure is implemented in Modelica to develop the simulation model for the gravity-fed evaporator. The loop dimensions are critical to the performance of the system. Hence it is essential to estimate the loop dimensions accurately. In this study, the simulations are carried out to predict the optimum dimensions to achieve the optimum circulation rate in the loop. It is expected that this study will be helpful in designing optimized gravity-fed evaporators for CO<sub>2</sub> based heat-pump chillers.

Keywords: Gravity-fed evaporator, Carbon Dioxide, Heat-pump, Modelica

## 1. INTRODUCTION

Gravity-fed evaporators are regarded as very simple and effective modification incorporated in a heat-pump unit to enhance the performance. As these evaporators are operated on flooded mode, it is possible to achieve better contact between liquid refrigerant and cooling surface of the heat exchanger. This leads to better heat transfer rates and hence helps in designing compact heat exchanger. For many years, gravity-fed evaporators have been used effectively in ammonia-based system. Several benefits can be obtained by incorporating such evaporators in heat-pump units. These systems eliminate the requirement of thermostatic expansion valve and operate independently irrespective of high-side pressure (Paliwoda, 1992a). In addition, the distribution of liquid refrigerant is better in these evaporators. Lorentzen (1968) presented different methods on how to implement gravity-fed evaporators as well as other types of flooded evaporators in refrigeration system. It was reported that the average efficiency of flooded evaporators is more than twice the efficiency of dry-expansion evaporators. Haukås (1986) presented a methodology and estimated optimum dimensions for gravity-fed evaporator implemented in a halocarbons-based system. It was reported that the ratio of evaporator coil length to inner diameter is the most critical parameter required to be optimized. Paliwoda (1992a) prepared an article to discuss how to develop a mathematical model for gravity-fed evaporator implemented in ammonia-based system. In this article too, it was reported how to optimize the dimensions for gravity-fed evaporator. These all studies show the benefits of implementing gravity-fed evaporator.

The present study is carried out to investigate the integration of gravity-fed evaporators in a CO<sub>2</sub> based heat-pump chiller. The purpose of this proposed CO<sub>2</sub> heat-pump chiller is to produce hot and cold water

simultaneously. Such systems could be implemented in different applications like fishing vessels, large kitchens, hotels etc. To integrate the gravity-fed evaporator in the proposed CO<sub>2</sub> system, a loop is designed which consists of a two-phase separator, a downcomer, the evaporator, and a riser. The dimensions of this loop play a significant role in the performance of the system. This study is performed to estimate the suitable dimensions of the gravity-fed evaporator loop. To fulfill this objective, a simulation model is developed in Modelica for the proposed CO<sub>2</sub> system. Based on the simulation results, the suitable dimensions are estimated for the gravity-fed evaporator loop. These results are presented in this paper.

## 2. MODELLING PROCEDURE

Figure 1 shows the schematic of the CO<sub>2</sub> heat-pump chiller with gravity-fed evaporator. To integrate the gravity-fed evaporator, a loop is designed which consists of a two-phase separator, a downcomer, the evaporator, and a riser. The liquid refrigerant (state pt. 6) separated in the separator is fed to the evaporator through the downcomer. Low vapor fraction ( $\approx 0.8$ ) is maintained at the exit of the evaporator. The fluid leaving the evaporator (state pt. 7) then goes back to the separator through the riser. From the separator, the vapor fraction (state pt. 8) is sent to the compressor (Comp) through the internal heat exchanger (IHX). The compressed fluid (state pt. 2) is cooled down to low temperature in the gas cooler (GC-DWH) and then in the IHX. The fluid exiting the IHX (state pt. 4), returns to the separator through high pressure control valve (HPV). This completes the cycle. However, the refrigerant flowrate through the compressor and the refrigerant flowrate in the gravity-fed evaporator loop are different. In this paper, the refrigerant flowrate through the compressor is termed as primary flow ' $\dot{m}_p$ ', while the refrigerant flowrate in the gravity-fed evaporator loop is termed as self-circulation flowrate ' $\dot{m}_{s-c}$ '.

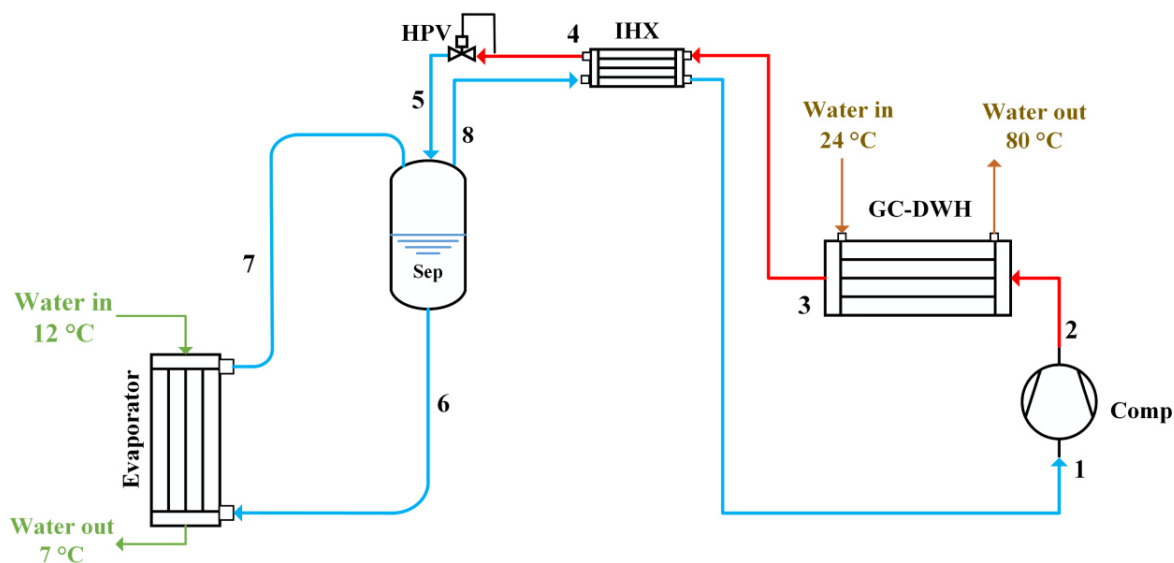


Figure 1: Schematic of the CO<sub>2</sub> heat-pump chiller with gravity-fed evaporator



where, ' $\xi$ ' is the coefficient of resistance for pipe components. Paliwoda (1992b) presents a table showing ' $\xi$ ' for different pipe components.

As low vapor fraction is maintained at the exit of evaporator, the flow through the riser is two-phase flow. The frictional pressure drop of two-phase flow is estimated from:

$$\Delta p_o = \beta_o \times \Delta p_g \quad (6)$$

where, ' $\beta_o$ ' is the two-phase multiplier and ' $\Delta p_g$ ' is the frictional pressure drop of single-phase vapor:

$$\Delta p_g = 0.241 \times \frac{\mu_g^{0.25}}{\rho_g} \times \dot{m}^{1.75} \times \frac{L_o}{d_o^{4.75}} \quad (7)$$

It is assumed that ' $\dot{x}_o$ ' is the quality of the two-phase fluid at the exit of the evaporator and it remains constant during the flow in the riser. Pressure drop ' $\Delta p_o$ ' is estimated considering this assumption.

The two-phase flow multiplier ' $\beta_o$ ' corresponding to quality ' $\dot{x}_o$ ' is estimated from (Paliwoda, 1992b):

$$\beta_o = [\vartheta + 2(1 - \vartheta) \times \dot{x}_o](1 - \dot{x}_o)^{0.333} + \dot{x}_o^{2.276} \quad (8)$$

where,

$$\vartheta = \frac{\Delta p_l}{\Delta p_g} = \frac{\rho_g}{\rho_l} \left( \frac{\mu_l}{\mu_g} \right)^{0.25} \quad (9)$$

In the riser, the pressure drop due to minor losses is estimated from:

$$\sum \Delta p_o = \frac{\dot{G}^2}{2\rho_g} \sum \xi_j \beta_{c,j} \quad (10)$$

The two-phase multiplier ' $\beta_c$ ' for each pipe component is estimated from:

$$\beta_c = [\vartheta + C(1 - \vartheta) \times \dot{x}_o](1 - \dot{x}_o)^{0.333} + \dot{x}_o^{2.276} \quad (11)$$

Paliwoda (1992b) presents a table showing the values for coefficient ' $C$ ' for different components.

To estimate the pressure drop in the evaporator, a quadratic equation dependent on the mass flow rate is used:

$$\Delta p_{ev} = b \times \dot{m}^2 \quad (12)$$

where b is:

$$b = \frac{\Delta p_n}{\dot{m}_n^2} \times \frac{l}{l_n} \quad (13)$$

These equations form the basis of the gravity-fed evaporator loop. To develop the model for this gravity-fed loop in object-oriented programming language Modelica [Modelica], component models are considered from TIL-library 3.9 [TLK-Thermo GmbH]. However, these models from TLK library do not have the appropriate equations (presented above) to estimate the minor losses, major losses and the gravity term in the pressure drop model. Hence, these models are upgraded including all the necessary equations to capture the physics of self-circulating flow in the loop. These upgraded models are then used to develop



the gravity-fed evaporator loop. Finally, the gravity-fed evaporator model is integrated with the proposed CO<sub>2</sub> heat-pump chiller to develop the complete model in Modelica. Dymola 2021 is used as the modelling environment [Dassault Systems].

### 3. DIMENSIONS OF COMPONENTS

Table 1: Dimensions of components

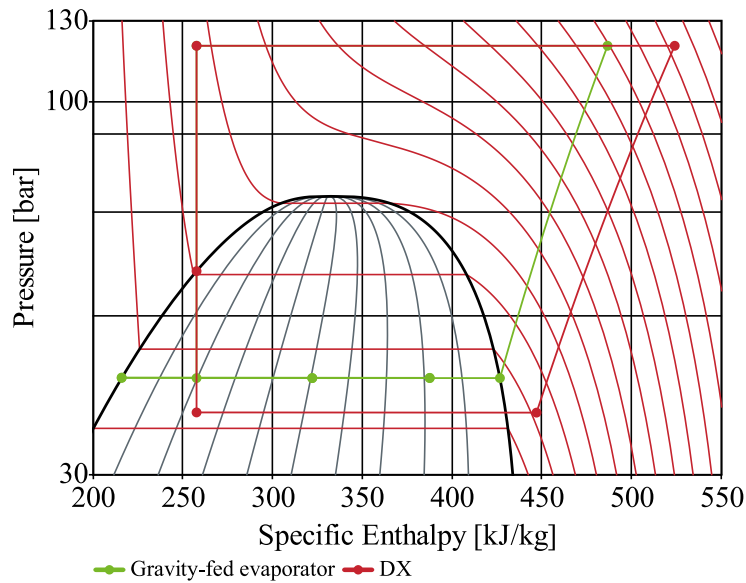
Downcomer	
Internal diameter (mm)	14
Length (mm)	1500
Riser	
Internal diameter (mm)	14 - 28
Length (mm)	2150
Evaporator (plate heat exchanger)	
Number of plates	40
Plate length (mm)	420
Plate width (mm)	155
Pattern angle (°)	22.5
Wall thickness (mm)	0.5
Pattern amplitude (mm)	2.9
Pattern wavelength (mm)	6

### 4. RESULTS AND DISCUSSION

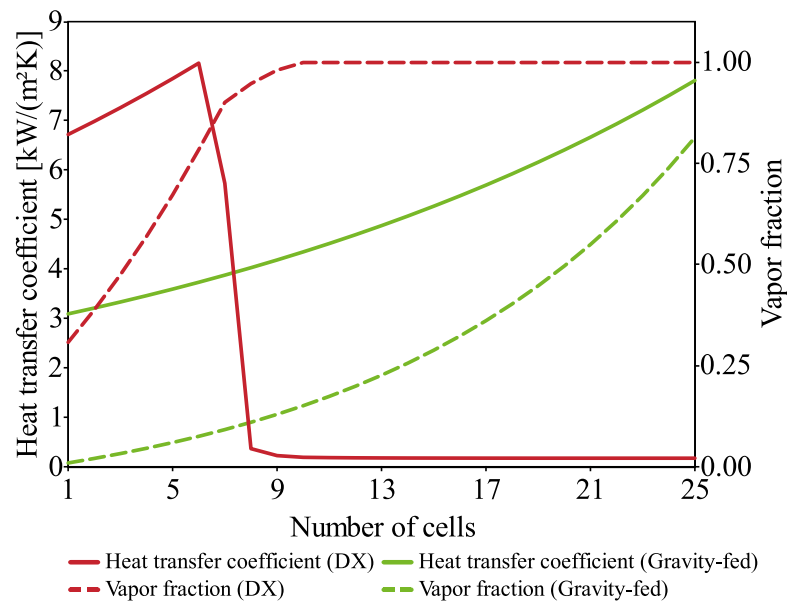
This section presents the results to show the implementation of gravity-fed evaporator loop in CO<sub>2</sub> based heat-pump. In a gravity-fed evaporator loop, low vapor fraction ( $\approx 0.8$ ) is maintained at the exit of evaporator to ensure better contact between liquid refrigerant and cooling surface of heat exchanger. This helps in achieving high heat transfer coefficient of the refrigerant and hence gives better heat transfer rates between refrigerant and secondary fluid. Therefore, gravity-fed evaporator performs better as compared to dry-expansion evaporator. Figure 3 shows the  $p$ - $h$  plot for gravity-fed evaporator and dry-expansion evaporator to achieve the same cooling capacity. It is observed that it is possible to raise the evaporation temperature by 4.3 K for gravity-fed evaporator as compared to dry-expansion evaporator. Figure 4 shows how the heat transfer coefficient and vapor fraction changes across the heat exchanger for gravity-fed and dry-expansion system. It is observed that the average heat transfer coefficient of gravity-fed evaporator is more than twice the heat transfer coefficient of dry-expansion evaporator.

Table 2: Simulation conditions

Discharge pressure (bar)	Suction pressure (bar)	Cooling capacity (kW)	Cold water temperature (°C)		Hot water temperature (°C)		GC approach temp. (K)
			in	out	in	out	
120	41	8.3	12	7	24	80	3



**Figure 3:  $p$ - $h$  plot for gravity-fed evaporator and DX evaporator**



**Figure 4: Heat transfer coefficient and Vapor fraction for gravity-fed evaporator and DX evaporator**

These results clearly show the benefit of gravity-fed evaporator over dry-expansion evaporator. To implement the gravity-fed evaporator, however, it is essential to investigate the effect of loop dimensions on the system performance. One critical parameter is static height which acts as a prime mover to generate the desired flow in the gravity-fed loop by overcoming all the resistances. The flowrate in the gravity-fed loop is defined as self-circulation flowrate in this study. The self-circulation flowrate strongly depends on the static height and total pressure resistances in the gravity-fed loop. To investigate the effect of height, it is varied from 0.35 m to 1.43 m. A very low static height generates low self-circulation flowrates which gets superheated at the exit of evaporator. This degrades the heat transfer rate in the evaporator and hence the overall performance. An increase in static height increases the self-circulation

flowrate and thereby superheating can be avoided and low vapour fractions can be achieved at the exit of evaporator. It is observed that static height of 0.68 m maintains vapor fraction of 0.8 which can be considered as optimum condition for the specified dimensions and capacity of the system. Figure 5 shows the effect of static height on cooling capacity, self-circulation flowrate, and primary flowrate. The pressure difference in the downcomer, evaporator, and riser are shown in figure 6.

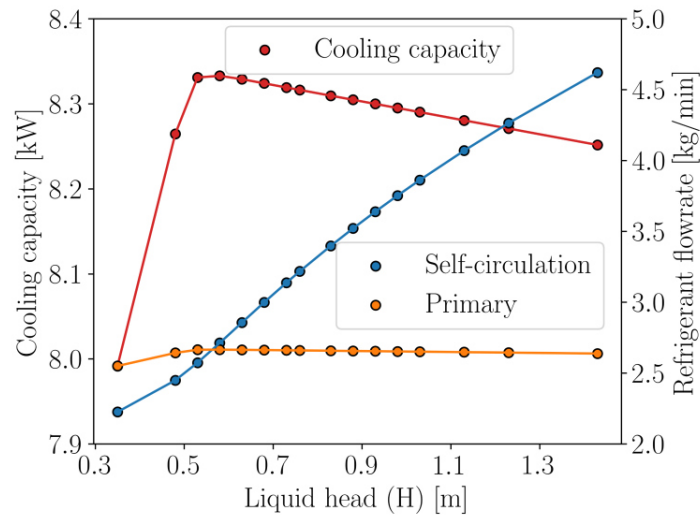


**Figure 5: Effect of static height on cooling capacity, self-circulation flowrate, and primary flowrate**

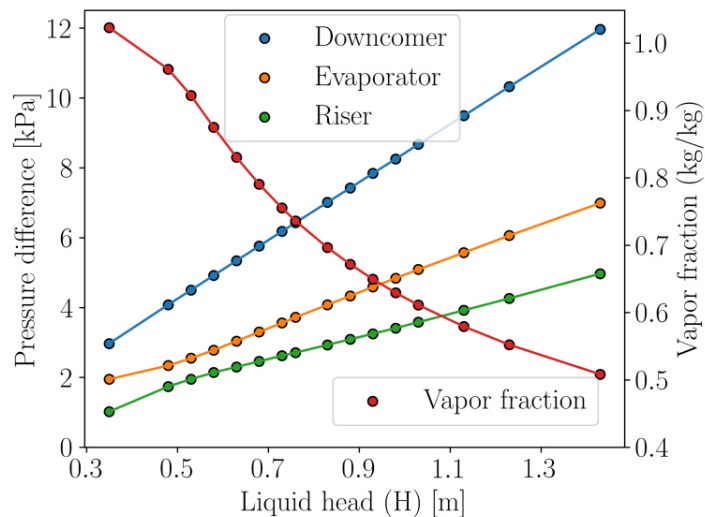


**Figure 6: Effect of static height on pressure difference in downcomer, evaporator, and riser**

Another important parameter is diameter of the riser tube in the gravity-fed loop. In this study, the riser diameter is first considered same as the downcomer diameter which is 14 mm. Then the riser diameter is varied from 14 mm to 28 mm. It is observed that as the riser diameter is increased, the pressure drop in the riser decreases and hence the self-circulation flowrate increases. Initially the flowrate increases sharply and then the rate of increment becomes steady for a riser diameter of 28 mm. Hence, it is not

effective to increase the riser diameter beyond 28 mm for the investigated case. Figure 7 shows the pressure difference in the downcomer, evaporator, and riser with changes in riser diameter, while figure 8 shows the cooling capacity. It is also observed that with higher self-circulation flowrate, the vapor fraction decreases at the exit of evaporator. Hence it can be concluded that selecting larger riser diameter as compared to downcomer diameter is beneficial. The riser diameter should be twice the size of downcomer diameter. Selecting a larger riser diameter gives the opportunity to reduce the static height of the gravity-fed loop.

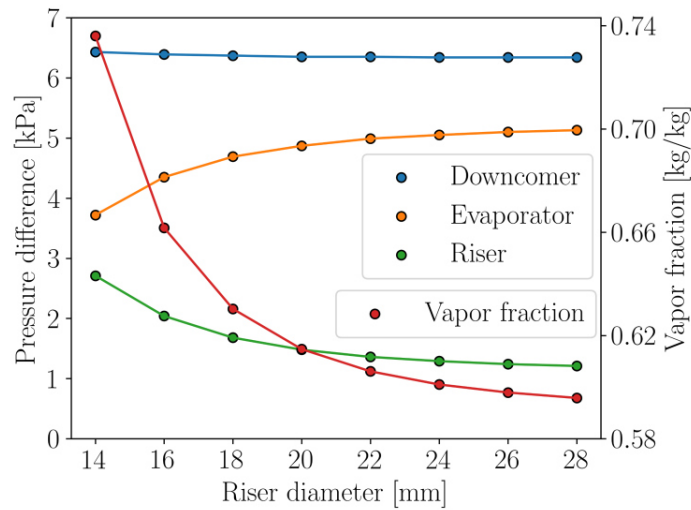


**Figure 7: Effect of riser diameter on pressure difference in downcomer, evaporator, and riser**

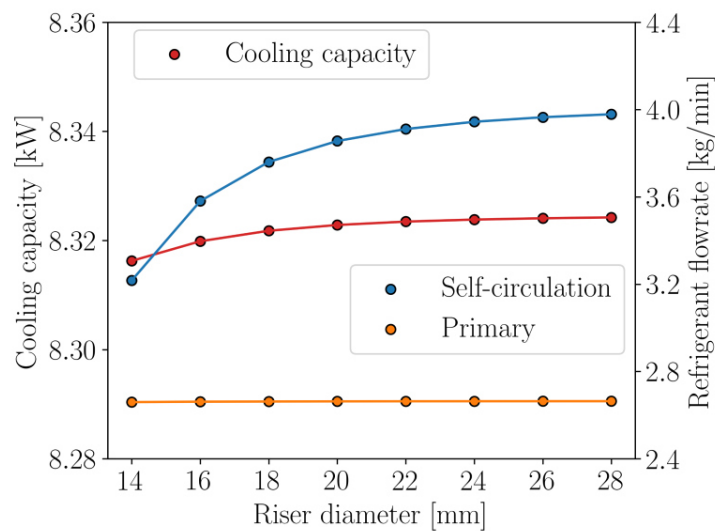


**Figure 8: Effect of riser diameter on cooling capacity and refrigerant flowrate**

## 5. CONCLUSIONS

This study presents the results for implementation of gravity-fed evaporator in a CO<sub>2</sub> heat pump chiller. Such evaporator configurations are operated on flooded mode to maintain low vapor fraction ( $\approx 0.8$ ) at the exit. This gives the possibility to achieve enhanced and high heat transfer coefficients. Simulation results show that the average heat transfer coefficient of a gravity-fed CO<sub>2</sub> evaporator is more than twice the heat transfer coefficient of dry-expansion evaporator. As a result, there is improvement in heat transfer rate. Better heat transfer rate gives the opportunity to raise the evaporation temperature. It is observed in the investigated case, that the evaporation temperature of gravity-fed evaporator is 4.3 K higher as compared to dry-expansion evaporator. These results clearly show how the system performance and energy efficiency can be enhanced by implementing gravity-fed evaporator. However, it is essential to design the gravity-fed evaporator loop properly to achieve the desired system performance. The static height ' $H$ ' and riser diameter are two critical parameters that significantly affect the system performance. Simulation results show that the static height of 0.68 m maintains vapor fraction of 0.8 which can be considered as optimum condition for the specified dimensions and capacity of the investigated system. Also, it is found that selecting a larger riser diameter helps in reducing the total resistances in the gravity-fed loop and hence gives the opportunity to reduce the static height. Results suggest that the riser diameter should be twice the size of downcomer diameter.

## ACKNOWLEDGEMENTS

The authors would like to acknowledge the support received from national research projects funded by the Research Council of Norway, i.e. the CoolFish project, and the Heat-Jet project.

## NOMENCLATURE

		<i>Greek letters</i>
$d$	Internal diameter of connecting tubes (m)	$\rho$ Density
$f$	Friction coefficient for flow inside pipe	$\mu$ Dynamic viscosity ( $\text{kg m}^{-1} \text{s}^{-1}$ )
$\dot{G}$	Mass flux ( $\text{kg m}^{-2} \text{s}^{-1}$ )	$\xi$ Coefficient of resistance for pipe components
$g$	Gravitational acceleration ( $\text{m s}^{-1}$ )	$\beta$ Two-phase multiplier
$H$	Liquid head above the entrance of evaporator (m)	<i>Subscripts</i>
$h$	Height of evaporator (m)	$ev$ evaporator
$L$	Length (m)	$g$ gas
$\dot{m}$	mass flowrate ( $\text{kg s}^{-1}$ )	$i$ Referred to inlet or downcomer
$\Delta p$	Pressure drop due to flow resistance ( $\text{N m}^{-2} = \text{pa}$ )	$l$ liquid
$\sum \Delta p$	Sum of pressure drops in pipe components ( $\text{N m}^{-2} = \text{pa}$ )	$o$ Referred to outlet or riser
$V$	Velocity of fluid ( $\text{m s}^{-1}$ )	
$\dot{x}$	Refrigerant vapor fraction ( $\text{kg kg}^{-1}$ )	

## REFERENCES

- Dassault Systems, DYMOLA Systems Engineering. Available online: <https://www.3ds.com/products-services/catia/products/dymola/>
- Haukås, H.T., 1986. Design and optimization of flooded evaporators with natural circulation, in: The Joint Israeli-Norwegian Symposium on Refrigeration.
- Lorentzen, G., 1968. Evaporator design and liquid feed regulation. *Int. J. Refrig.* (November December).
- Modelica. The Modelica Association. Available online: <https://modelica.org/>
- Paliwoda, A., 1992a. Calculation of basic parameters for gravity-fed evaporators for refrigeration and heat pump systems. *Int. J. Refrig.* 15, 41–47.
- Paliwoda, A., 1992b. Generalized method of pressure drop calculation across pipe components containing two-phase flow of refrigerants. *Int. J. Refrig.* 15, 119–125.
- TLK-Thermo GmbH. TIL Suite Thermal Systems. Available online: <https://www.tlk-thermo.com/index.php/en/software/til-suite>

### Open access to applied data

HAZARIKA, Mihir Mouchum; BENGSCHE, Jan; HAFSÅS, Johan; HAFNER, Armin; SVENDSEN, Eirik Starheim; YE, Zuliang, 2022, "Integration of gravity-fed evaporators in CO<sub>2</sub> based heat-pump chillers", <https://doi.org/10.18710/KTQZPL>

**G Abstract for the 26th  
International Congress of  
Refrigeration**

# Investigation and analysis of a CO<sub>2</sub> heat pump chiller with novel two-stage evaporator

Jan Bengsch<sup>1</sup>, Mihir Mouchum Hazarika<sup>1</sup>, Armin Hafner<sup>1\*</sup>,

<sup>1</sup>Department of Energy and Process Engineering, Norwegian University of Science and Technology, Trondheim, \*armin.hafner@ntnu.no

## Abstract

This study is carried out to investigate the performance of a transcritical CO<sub>2</sub> heat pump chiller that provides heating and cooling simultaneously. There are several applications where such CO<sub>2</sub> systems are implemented, i.e., hotels, large kitchens, fishing vessels, etc. Depending on the type of applications, these systems can be designed to achieve the desired hot and cold fluid temperature on the secondary side. The system investigated in the present study is utilized to produce hot water (up to 90°C) and chilled water (4°C). The evaporator utilized for chilled water production is a novel two-stage evaporator. The first stage of this evaporator operates on gravity-fed mode while the second stage operates on ejector-supported mode. The secondary loop is internally connected within the plate heat exchanger. This evaporator configuration gives the possibility to achieve a higher temperature gradient on the secondary fluid side. To analyze the performance of this proposed CO<sub>2</sub> system with the two-stage evaporator, a simulation model is developed in Modelica. Using this model, simulations are carried out to analyze the performance of the system under different operating conditions. Results show that the integration of the two-stage evaporator enhances the overall performance as the cooling capacity is shared between the two stages and the suction pressure of the compressor is elevated by utilizing the ejector.

Keywords: CO<sub>2</sub>, heat-pump chiller, two-stage evaporation, Modelling, Modelica



